

AzTEC half square degree survey of the SHADES fields - II. Identifications, redshifts, and evidence for large-scale structure

Michał J. Michałowski^{1*}, J. S. Dunlop¹, R. J. Ivison^{2,1}, M. Cirasuolo^{1,2}, K. I. Caputi^{3,1}, I. Arétxaga⁴, V. Arumugam¹, J. E. Austermann⁵, E. L. Chapin^{6,7}, S. C. Chapman⁸, K. E. K. Coppin⁹, E. Egami¹⁰, D. H. Hughes⁴, E. Ibar², A. M. J. Mortier^{11,1}, A. M. Schaefer^{12,1}, K. S. Scott¹³, I. Smail¹⁴, T. A. Targett¹, J. Wagg¹⁵, G. W. Wilson¹⁶, L. Xu¹⁰, M. Yun¹⁶

¹SUPA†, Institute for Astronomy, University of Edinburgh, Royal Observatory, Edinburgh, EH9 3HJ

²UK Astronomy Technology Centre, Royal Observatory, Edinburgh EH9 3HJ

³Kapteyn Astronomical Institute, University of Groningen, P.O. Box 800, 9700 AV Groningen, The Netherlands

⁴Instituto Nacional de Astrofísica, Óptica y Electrónica (INAOE), Aptdo. Postal 51 y 216, 72000 Puebla, Pue., Mexico

⁵Center for Astrophysics and Space Astronomy, University of Colorado, Boulder, CO 80309, USA

⁶Department of Physics & Astronomy, University of British Columbia, 6224 Agricultural Road, Vancouver, BC V6T 1Z1, Canada

⁷XMM SOC, ESAC, Apartado 78, 28691 Villanueva de la Cañada, Madrid, Spain

⁸Institute of Astronomy, University of Cambridge, Madingley Road, Cambridge CB3 0HA

⁹Department of Physics, McGill University, 3600 Rue University, Montreal, QC H3A 2T8, Canada

¹⁰Steward Observatory, University of Arizona, 933 N. Cherry Ave, Tucson, AZ 85721, USA

¹¹Astrophysics Group, Imperial College London, Blackett Laboratory, Prince Consort Road, London SW7 2AZ

¹²Max Planck Institute for Extraterrestrial Physics, 85748 Garching bei München, Germany

¹³North American ALMA Science Center, National Radio Astronomy Observatory, Charlottesville, VA 22903

¹⁴Institute for Computational Cosmology, Durham University, South Road, Durham DH1 3LE

¹⁵European Southern Observatory, Casilla 19001, Santiago, Chile

¹⁶University of Massachusetts, Department of Astronomy, Amherst, MA 01003, USA

Accepted 2012 July 30. Received 2012 July 27; in original form 2012 May 09

ABSTRACT

The AzTEC 1.1 mm survey of the two SCUBA HALf Degree Extragalactic Survey (SHADES) fields is the largest (0.7 deg^2) blank-field millimetre-wavelength survey undertaken to date at a resolution of $\simeq 18 \text{ arcsec}$ and a depth of $\simeq 1 \text{ mJy}$. We have used the deep optical-to-radio multi-wavelength data in the SHADES Lockman Hole East and SXDF/UDS fields to obtain galaxy identifications for $\simeq 64\%$ ($\simeq 80\%$ including tentative identifications) of the 148 AzTEC-SHADES 1.1 mm sources reported by Austermann et al. (2010), exploiting deep radio and $24 \mu\text{m}$ data complemented by methods based on $8 \mu\text{m}$ flux-density and red optical-infrared ($i - K$) colour. This unusually high identification rate can be attributed to the relatively bright millimetre-wavelength flux-density threshold, combined with the relatively deep supporting multi-frequency data now available in these two well-studied fields. We have further exploited the optical–mid-infrared–radio data to derive a $\simeq 60\%$ ($\simeq 75\%$ including tentative identifications) complete redshift distribution for the AzTEC-SHADES sources, yielding a median redshift of $z \simeq 2.2$, with a high-redshift tail extending to at least $z \simeq 4$. Despite the larger area probed by the AzTEC survey relative to the original SCUBA SHADES imaging, the redshift distribution of the AzTEC sources is consistent with that displayed by the SCUBA sources, and reinforces tentative evidence that the redshift distribution of mm/sub-mm sources in the Lockman Hole field is significantly different from that found in the SXDF/UDS field. Comparison with simulated surveys of similar scale extracted from semi-analytic models based on the Millennium simulation indicates that this is as expected if the mm/sub-mm sources are massive ($M > 10^{11} M_\odot$) star-forming galaxies tracing large-scale structures over scales of 10–20 Mpc. This confirms the importance of surveys covering several square degrees (as now underway with SCUBA2) to obtain representative samples of bright (sub)mm-selected galaxies. This work provides a foundation for the further exploitation of the *Spitzer* and *Herschel* data in the SHADES fields in the study of the stellar masses and specific star-formation rates of the most active star-forming galaxies in cosmic history.

Key words: galaxies: distances and redshifts – galaxies: evolution – galaxies: high-redshift – galaxies: stellar content – cosmology: miscellaneous – submillimetre: galaxies

1 INTRODUCTION

The objects uncovered by high galactic latitude surveys at (sub)millimetre wavelengths (generally termed ‘submillimetre galaxies’; SMGs), are now understood to be distant ($z \simeq 2\text{--}3$) and massive ($\simeq 10^{11} M_{\odot}$) star-forming galaxies (Aretxaga et al. 2003, 2007; Dannerbauer et al. 2004; Smail et al. 2004; Swinbank et al. 2004, 2006; Takagi et al. 2004; Borys et al. 2005; Chapman et al. 2005; Greve et al. 2005; Tacconi et al. 2006, 2008; Eales et al. 2009; Amblard et al. 2010; Dunlop et al. 2010; Engel et al. 2010; Michałowski et al. 2010a,b, 2012; Santini et al. 2010; Hainline et al. 2011; Hayward et al. 2011; Targett et al. 2011; Wardlow et al. 2011; Béthermin et al. 2012; Bussmann et al. 2012; Shimizu et al. 2012; Yun et al. 2012). However, the role of these spectacular objects in the cosmic history of galaxy/star formation has yet to be properly established.

The majority of the submillimetre surveys undertaken with the Submillimetre Common-User Bolometer Array (SCUBA; Holland et al. 1999) on the James Clerk Maxwell Telescope (JCMT) covered small ($< 0.03 \deg^2$) fields due to sensitivity and time constraints (Smail et al. 1997; Hughes et al. 1998; Barger et al. 1998, 1999, 2000, 2001, 2002; Chapman et al. 2001, 2003; Scott et al. 2002; Webb et al. 2003; Wang et al. 2004; Coppin et al. 2005; Pope et al. 2006). Only two submillimetre surveys completed to date cover a significant fraction of a degree: the SCUBA HAlf Degree Extragalactic Survey (SHADES; $0.2 \deg^2$; Mortier et al. 2005; Coppin et al. 2006) undertaken at the JCMT, and the $870 \mu\text{m}$ survey of the ECDFS field ($0.25 \deg^2$; Weiß et al. 2009) performed with the Large APEX BOlometer CAmera (LABOCA; Siringo et al. 2009) on the Atacama Pathfinder Experiment (APEX).

At slightly longer wavelengths (1.1–1.2 mm) surveys with the Max-Planck Millimeter Bolometer array (MAMBO) on the IRAM 30-m telescope, and with the AzTEC (Wilson et al. 2008) on the JCMT and Atacama Submillimetre Telescope Experiment (ASTE; Ezawa et al. 2004, 2008) have generally covered areas of $< 0.25 \deg^2$ (Greve et al. 2004, 2008; Bertoldi et al. 2007; Perera et al. 2008; Scott et al. 2008, 2010; Austermann et al. 2009; Hatsukade et al. 2011; Lindner et al. 2011). The notable exceptions are the MAMBO survey of the (possibly lensed) field of the cluster Abell 2125 totalling $0.44 \deg^2$ (Wagg et al. 2009), and the AzTEC/ASTE survey of the COSMOS field with a $\simeq 34 \text{ arcsec}$ beam covering $0.72 \deg^2$ (Aretxaga et al. 2011).

There are number of reasons why it is necessary to analyse SMG properties in fields with significant sizes (of the order of a \deg^2 or more). Smaller fields miss the rare members of the SMG population, i.e. both low- and high-redshift parts of the distribution as well as the bright-end of the luminosity function. Moreover, the clustering properties and large-scale structures traced by SMGs can only be studied in fields larger than these structures. Finally, significant field-to-field variation (cosmic variance) advocates the need of observing multiple well-separated fields.

Here we analyse the properties of the galaxies detected in the largest very deep (rms $0.9\text{--}1.7 \text{ mJy per beam}$) blank-field millimetre survey of the Lockman Hole East and the Subaru/*XMM-Newton* Deep Field (SXDF) (aka UKIDSS

Ultra Deep Survey (UDS) field) conducted with AzTEC mounted on the JCMT (beam size 18 arcsec FWHM) which covers a total area of $0.7 \deg^2$ (Austermann et al. 2010). At present, the only substantially larger millimetre-wavelength survey is the $87 \deg^2$ survey program undertaken with the South Pole Telescope (Vieira et al. 2010), but this has a much larger beam size ($\simeq 60 \text{ arcsec}$) and much lower sensitivity (3.4 mJy at 1.4 mm , which corresponds to 6.5 mJy at 1.1 mm assuming the average SMG spectral energy distribution (SED) from Michałowski et al. 2010a at $z = 2\text{--}3$).

The AzTEC survey considered here incorporates the two smaller fields (totalling $\simeq 0.2 \deg^2$) covered by the original SCUBA-SHADES $850 \mu\text{m}$ imaging. The $850 \mu\text{m}$ sources uncovered by SCUBA (Coppin et al. 2006) have already been the subject of extensive multi-frequency analysis, including the identification of their galaxy counterparts via radio (VLA 1.4 GHz) and mid-IR (*Spitzer* 24 μm) imaging (Ivison et al. 2007), estimation of their redshifts from the observed submillimetre-radio SEDs (Aretxaga et al. 2007), further redshift estimation and stellar mass determination based on the optical-infrared data (Takagi et al. 2007; Dye et al. 2008; Clements et al. 2008), follow-up imaging at $350 \mu\text{m}$ (Coppin et al. 2008), and studies of their environments and clustering (Serjeant et al. 2008; van Kampen et al. 2005). Individual SHADES sources have also been the subject of detailed high-resolution follow-up with the SMA (Younger et al. 2008; Hatsukade et al. 2010) and with *Spitzer* mid-infrared spectroscopy (Coppin et al. 2010). A final analysis of the redshift distribution and properties of the SCUBA-SHADES galaxies will be presented in Schael et al. (in preparation).

As is well-known, the large beams delivered by current single-dish (sub)millimetre facilities hampers the search for robust counterparts at other wavelengths. Usually the radio observations are used, both because the radio emission is believed to be related to the far-IR emission (e.g. Condon 1992), and because the surface number density of bright radio sources is relatively low (and hence associations are often unique and statistically significant). Experience has shown that radio identifications can typically be secured for $\simeq 30\text{--}70\%$ of SMGs; the precise percentage depends on the relative depths of the (sub)millimetre and radio data (Ivison et al. 2002, 2007; Dannerbauer et al. 2004, 2010; Pope et al. 2006; Chapin et al. 2009; Aretxaga et al. 2011; Chapin et al. 2011; Biggs et al. 2011; Wardlow et al. 2011), with completion rates of up to 80% being achieved for the relatively bright ($S_{1.1\text{mm}} > 4 \text{ mJy}$) and/or possibly lensed samples of Ivison et al. (2005) and Wagg et al. (2009). Recently Lindner et al. (2011) obtained a 93% identification (ID) rate for a sample of 41 SMGs using very deep radio data. Attempts have been made to boost the identification fraction further using, for example, *Spitzer* MIPS 24 μm data, but these have generally resulted in only a modest increase in the number of secure galaxy counterparts (Ivison et al. 2007). It has also been shown that for 30–60% of SMGs (depending on depth) one can obtain 3–8 μm counterparts using the *Spitzer*/IRAC data (Ashby et al. 2006; Pope et al. 2006; Biggs et al. 2011).

The objective of this paper is to provide secure identifications and photometric redshifts for as many as possible of the 148 AzTEC-SHADES 1.1 mm sources, exploiting not only the latest extremely-deep VLA/GMRT radio

and *Spitzer* MIPS 24 μm data, but also the deep *Spitzer* IRAC 8 μm maps, and the ever-improving optical–near-infrared imaging which has now been secured within both the UDS/SXDF and Lockman East fields. There are two reasons to expect that we should be able to secure a higher ID fraction for the AzTEC-SHADES sample than has been obtained for any previous large (>100 source) and complete sample of (sub)millimetre sources. The first is that our 1.1 mm source sample is relatively bright¹ and so we are not probing the faint part of the high-redshift (sub)millimetre luminosity function. The second is that, over the required $\simeq 0.7 \deg^2$ area, the radio, mid-infrared and near-infrared/optical data are among some of the deepest currently available. These considerations have encouraged us to try to refine the use of mid-infrared data and optical-infrared colour information to maximise the completeness of the galaxy identifications and hence the inferred redshift distribution of the AzTEC 1.1 mm sources.

Here we present the final results of this ID analysis, and derive photometric redshifts for the galaxies in the resulting near-complete SMG sample. We explore the implications of the inferred redshift distribution of this SMG sample, comparing it with redshift distributions previously reported from other, smaller, mm-wavelength surveys. We also explore the consistency of the redshift distributions of the AzTEC sources found in the two separate SHADES survey fields, as well as comparing the AzTEC source redshift distribution with that already derived for the SCUBA 850 μm sources. Further analysis of the full SEDs of the AzTEC sources, including derived physical properties such as star formation rates and stellar masses, is deferred to a future paper.

This paper is structured as follows. In Section 2 we summarize the available multi-wavelength data. Then, in Section 3, we describe the methods used to identify potential galaxy counterparts at other wavelengths, and to assess their statistical significance/robustness. The resulting galaxy IDs, photometric redshifts, and optical-infrared SEDs are presented in Sections 4, 5 and 6, respectively, with notes on individual sources provided in Appendix A. In Section 7 we explore the implications of the derived redshift distributions, and assess the evidence for large-scale structure with the aid of simulated AzTEC surveys extracted from cosmological simulations. Section 8 closes with our conclusions. We use a cosmological model with $H_0 = 70 \text{ km s}^{-1} \text{ Mpc}^{-1}$, $\Omega_\Lambda = 0.7$ and $\Omega_m = 0.3$, and give all magnitudes in the AB system.

¹ The rms of the AzTEC 1.1 mm data in the SHADES fields is 0.9–1.7 mJy (Austermann et al. 2010), i.e. a factor of $\simeq 2$ shallower than for the AzTEC survey of the GOODS-S field (rms 0.48–0.73 mJy (Scott et al. 2010)) and for the LESS survey of the ECDFS (rms 1.2 mJy at 870 μm (Weiß et al. 2009)), corresponding to 0.6–0.7 mJy at 1.1 mm assuming the average SMG spectral energy distribution from Michałowski et al. (2010a) at $z = 2\text{--}3$.

2 DATA

We utilised the JCMT/AzTEC 1.1 mm maps and catalogues from Austermann et al. (2010)². These data cover $0.7 \deg^2$ to an rms depth of 0.9–1.7 mJy per beam. We selected all 148 sources presented by Austermann et al. (2010) with signal-to-noise ratios (S/N) > 3.5 , and adopted the statistically deboosted 1.1 mm flux densities.

The VLA 1.4 GHz and GMRT 0.61 GHz radio data were taken from Ivison et al. (2005, 2007) and Ibar et al. (2009, 2010) respectively. The 1σ rms depths at the centre of the radio images are 6 and 9 $\mu\text{Jy beam}^{-1}$ for the 1.4 GHz maps in the Lockman Hole East and the UDS field respectively, and 15 $\mu\text{Jy beam}^{-1}$ for the 0.61 GHz map in the Lockman Hole. Both the VLA and GMRT radio imaging delivered a beam size of 5 arcsec (FWHM). The catalogues include sources for which $> 3\sigma$ detections were obtained.

The mid-infrared *Spitzer* data in the Lockman Hole East are from programs PID 81 (PI: G. Rieke) and PID 50249 (PI: E. Egami), described in Egami et al. (2004) and Dye et al. (2008), whereas in the UDS field the mid-infrared data are from the *Spitzer* Public Legacy Survey of the UKIDSS Ultra Deep Survey (SpUDS; PI: J. Dunlop)³ described in Caputi et al. (2011).

The optical data in both fields were obtained with Subaru/SuprimeCam (Miyazaki et al. 2002), as described in Dye et al. (2006) and Furusawa et al. (2008). The near-infrared data in both fields are provided by the UKIRT Infrared Deep Sky Survey (UKIDSS; Lawrence et al. 2007) with the SXDF/UDS field benefitting from the ultra-deep J, H, K coverage provided by the UDS survey (e.g. Cirasuolo et al. 2010), while the Lockman Hole East field is part of the somewhat shallower UKIDSS DXS survey (Warren et al. 2007).

The depths of the data in both fields are summarized in Table 1.

3 IDENTIFICATION METHOD

3.1 Radio and 24 μm IDs

We obtained the radio and 24 μm counterparts applying the method outlined in Downes et al. (1986), Dunlop et al. (1989) and Ivison et al. (2007). The 2.5σ search radius r around each AzTEC position was determined on the basis of the deboosted signal-to-noise ratio (S/N): $r = 2.5 \times 0.6 \times \text{FWHM}/(S/N)$, where FWHM = 18 arcsec is the size of the beam delivered by the JCMT at 1.1 mm. In order to account for systematic astrometry shifts (due to either pointing inaccuracies or source blending; e.g. Dunlop et al. 2010) we used a minimum search radius $r = 8$ arcsec whenever the above formula produced $r < 8$ arcsec (this proved necessary for only 20 AzTEC sources).

The statistical significance of each potential counterpart was assessed on the basis of the corrected Poisson probability

² The fluxes have been recently revised by Downes et al. (2012), but this change does not have any significant impact on our analysis.

³ <http://ssc.spitzer.caltech.edu/spitzermission/observingprograms/legacy/spuds/>

Table 1. The 3σ depths of the multi-frequency data used in the Lockman Hole East and SXDF/UDS fields.

Filter	LH	UDS	Unit
<i>B</i>	27.4	28.8	AB mag
<i>R</i>	26.4	28.1	AB mag
<i>i</i>	26.3	27.8	AB mag
<i>z</i>	25.6	26.9	AB mag
<i>J</i>	22.9	25.5	AB mag
<i>H</i>	...	24.8	AB mag
<i>K</i>	23.5	25.2	AB mag
3.6 μm	0.8	1.4	μJy
4.5 μm	1.6	1.5	μJy
5.6 μm	11	19	μJy
8.0 μm	13	12	μJy
24 μm	25	30	μJy
1.1 mm	0.9–1.3	1.0–1.7	mJy
1.4 GHz	18	27	μJy
0.6 GHz	45	...	μJy

p that the chosen radio or 24 μm candidate could have been selected by chance.

3.2 IRAC 8 μm IDs

In order to maximize the fraction of AzTEC galaxies with identified counterparts we also explored other ways to select IDs.

There is now a growing body of evidence indicating that SMGs are bright at the rest-frame near-IR wavelengths (Ashby et al. 2006; Pope et al. 2006; Hainline et al. 2009; Biggs et al. 2011; Wardlow et al. 2011) and hence are expected to be massive (Borys et al. 2005; Michałowski et al. 2010a,b, 2012; Hainline et al. 2011; Bussmann et al. 2012; Yun et al. 2012). Similar to Ashby et al. (2006), we thus explored the potential of using the available IRAC 8.0 μm imaging to search for IDs. We used the longest IRAC wavelength because the surface density of bright sources is lower than at shorter wavelengths.

We selected the 8 μm IDs in a similar way to the radio and 24 μm IDs; i.e. we searched for 8 μm objects within the same search radius, and estimated the probability of a chance association using analogous p -statistics. To do this we derived the cumulative number counts of 8.0 μm sources in our fields; we found that this had the form $N(> S_{8.0}) \propto S_{8.0}^{-1.1}$ with a normalization given by $N(> 20 \mu\text{Jy}) = 4 \text{ arcmin}^{-2}$. We did not select candidate identifications at flux densities fainter than 20 μJy .

3.3 Red $i - K$ IDs

It is now well known that SMGs generally exhibit red optical/near-IR colours (Smail et al. 1999, 2002, 2004; Ivison et al. 2002; Webb et al. 2003; Dannerbauer et al. 2004; Ashby et al. 2006; Yun et al. 2012). This is likely a consequence of two effects: SMGs are very dusty and they host a significant evolved stellar population (Michałowski et al. 2010a, 2012). Similarly, $\simeq 60\%$ of ULIRGs at $z \simeq 2\text{--}3$ are very red with $i - K > 2.5$ (Caputi et al. 2006).

Therefore, we explored the potential of red $i - K$ colour to yield SMG galaxy counterparts, building on the work of Schael et al. (in preparation)⁴. Schael et al. showed, for SCUBA sources in the SHADES fields, that the reddest ($i - K > 2$) source within 10 arcsec of the SCUBA position usually corresponds to the radio ID. We therefore selected all sources with $i - K > 2$ within the search radius defined above, and again estimated their reliability as AzTEC IDs by estimating the *a priori* probability p . The number density of K -band detected sources in the magnitude range of interest is well described by Euclidean counts, with $N(> S_K) \propto S_K^{-1.5}$. We estimated the number density at $K = 23$ mag separately for sources with $i - K$ colours 2–2.5, 2.5–3 and > 3 to be $N(K < 23 \text{ mag}) = 8 \text{ arcmin}^{-2}$, 4 arcmin^{-2} and 2 arcmin^{-2} , respectively. These number densities were used to calculate the p -values for sources with $i - K$ colours of 2–2.5, 2.5–3 and > 3 , respectively. We did not select sources fainter than $K = 23$ mag.

4 IDENTIFICATIONS

In Figs. B1 and B2 we present thumbnail images for all of the AzTEC-SHADES sources, with the IDs indicated by coloured symbols. For completeness and future reference, Tables B3 and B4 give the positions, relevant flux densities, angular offsets (from the original AzTEC 1.1 mm positions), and probabilities of chance associations (p) for all candidate radio and 24 μm IDs, regardless of their p -values. When IDs obtained at different wavelengths were separated by less than 2.5 arcsec they are listed as a single ID. Tables B1 and B2 present the relevant data only for the reliable IDs with $p < 0.05$ (marked in bold) and tentative IDs with $0.05 < p < 0.1$ (marked in italics). The coordinates listed are those of the 1.4 GHz ID if present, or alternatively those of the appropriate 24 μm (or 0.61 GHz), 8 μm , or $i - K$ selected ID.

We matched these coordinates with the optical/near-infrared catalogues, using a matching search radius of $r = 1.5$ arcsec. The resulting multi-wavelength photometry was used both to derive photometric redshifts for the IDs (Section 5), and also to select additional IDs as described above. Specifically, using the method presented in Section 3.2 we selected 9 (5) additional IDs in the Lockman Hole field (UDS field) from the IRAC 8.0 μm imaging. For 2 (1) of the AzTEC-SHADES sources these are the only IDs, so this method adds a very small, but still useful set of extra identifications. We checked the 22 AzTEC sources for which we found both robust radio ($p < 0.05$) and 8.0 μm IDs, and found that they coincided in 20 cases (91%), providing additional confidence that the 8.0 μm method can be reliably utilised when the radio data are not deep enough.

In addition, using the method presented in Section 3.3 we identified 16 (28) significant $i - K$ colour-selected IDs in the Lockman Hole field (UDS field). For 1 (5) of the AzTEC-SHADES sources these are the only IDs, so again the result of this effort is another small, but helpful set of additional identifications, along with supporting evidence for several others. Again we checked the AzTEC sources for which we

⁴ See also Schael (2009).

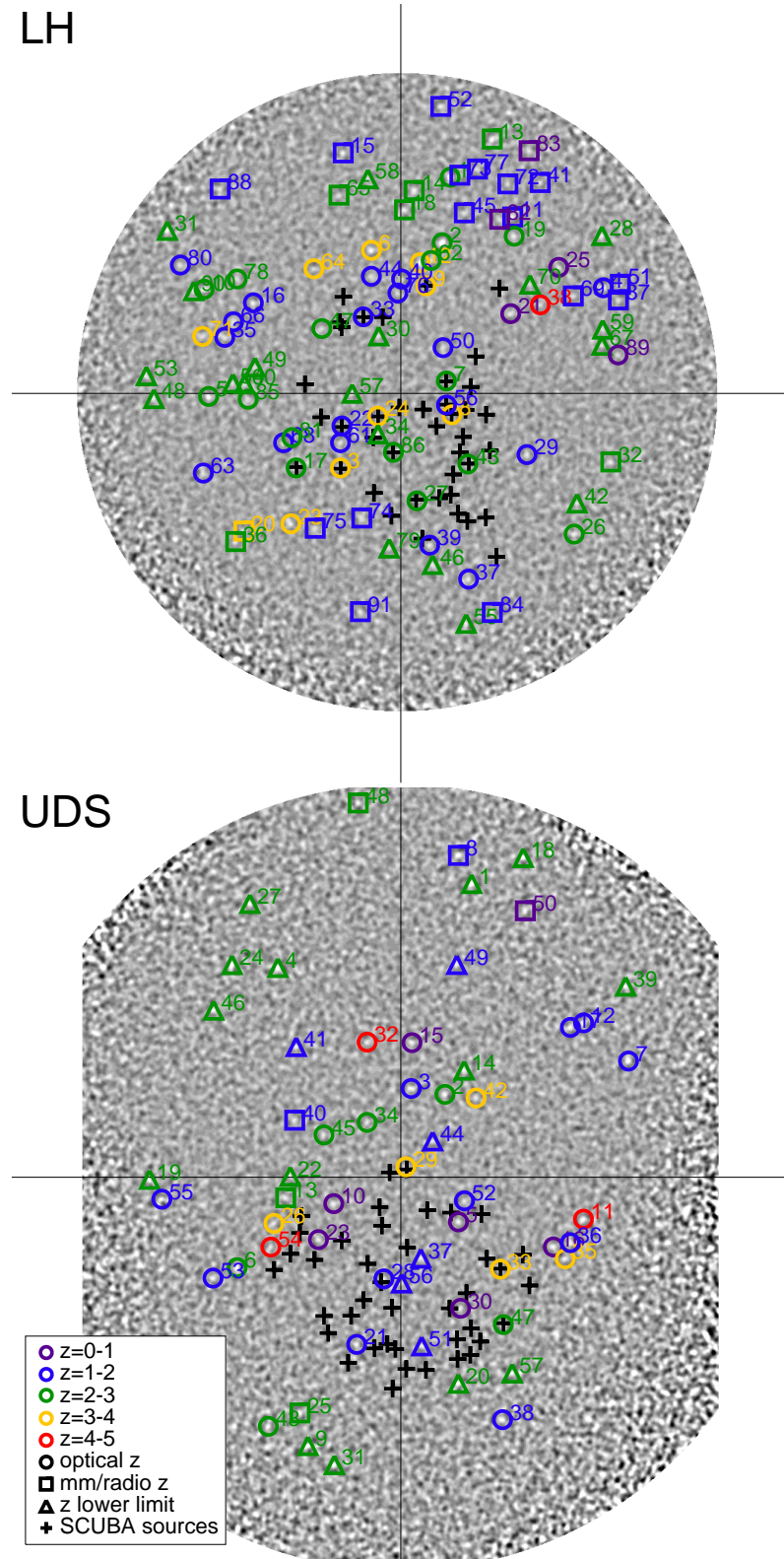
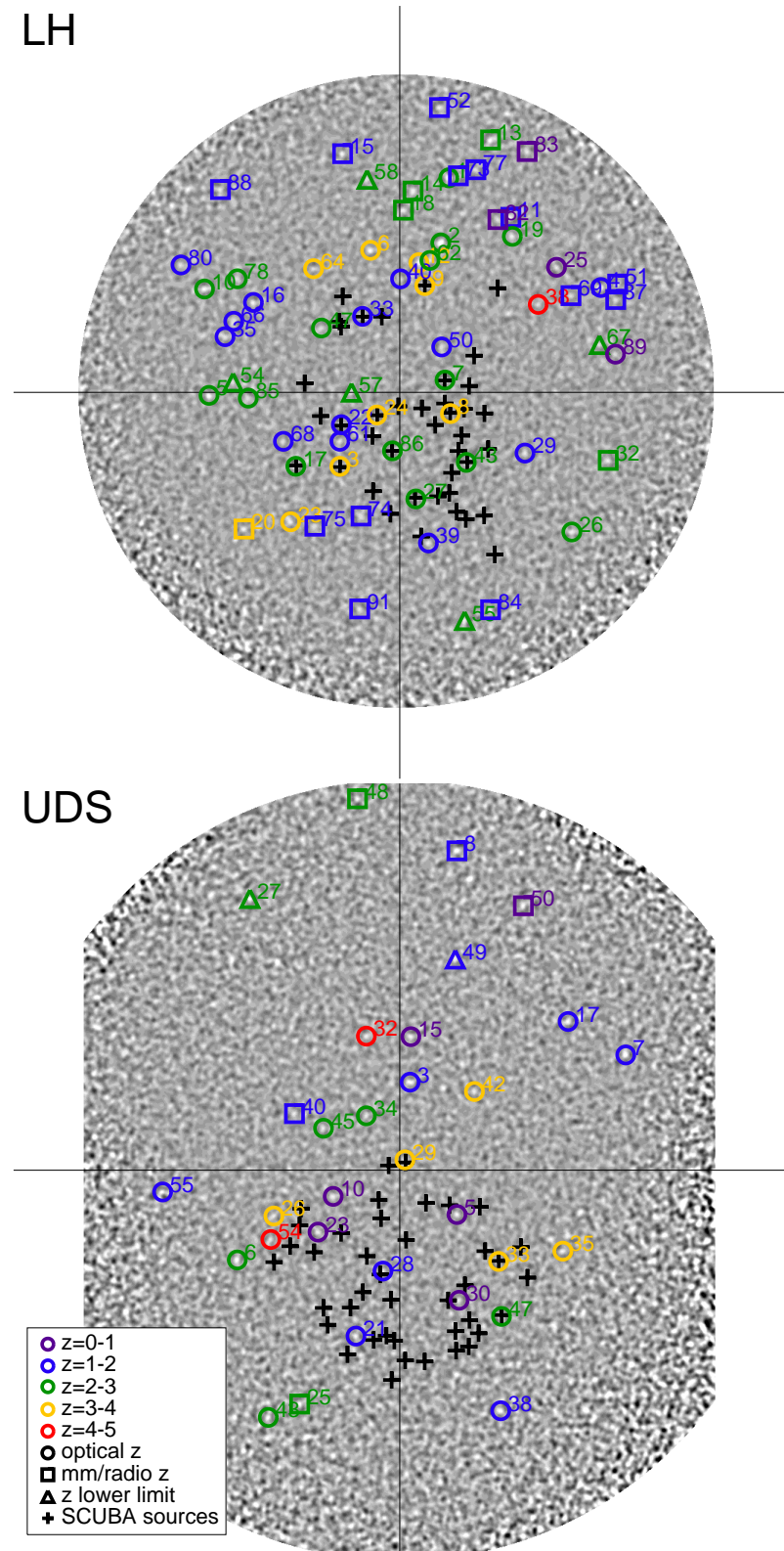


Figure 1. The AzTEC 1.1 mm maps of the Lockman Hole (*top*) and the SXDF/UDS field (*bottom*) from Austermann et al. (2010). Both images are 0.88 deg on a side (the noisier edges have been removed). The sources analysed in this paper are marked and colour-coded according to their redshifts. Circles correspond to spectroscopic or photometric optical or mid-infrared PAH redshifts, whereas squares correspond to redshifts derived from the 1.1 mm/1.4 GHz flux-density ratio based on the average SED model of SMGs (Michałowski et al. 2010a). In the case of a radio non-detection this method provides only a lower limit to the redshift and such cases are marked as triangles. Black lines divide both fields into four equal parts each with an area similar to that of the GOODS-N AzTEC survey studied by Chapin et al. (2009). 50% (4/8) of these sub-fields do not contain any low-redshift SMGs (i.e. robust identifications with $z < 1$). Crosses denote 850 μ m-selected galaxies for which photometric redshifts have been derived by Schael et al. (in preparation).

**Figure 2.** The same as Fig. 1, but this time only showing robust (category 1) IDs.

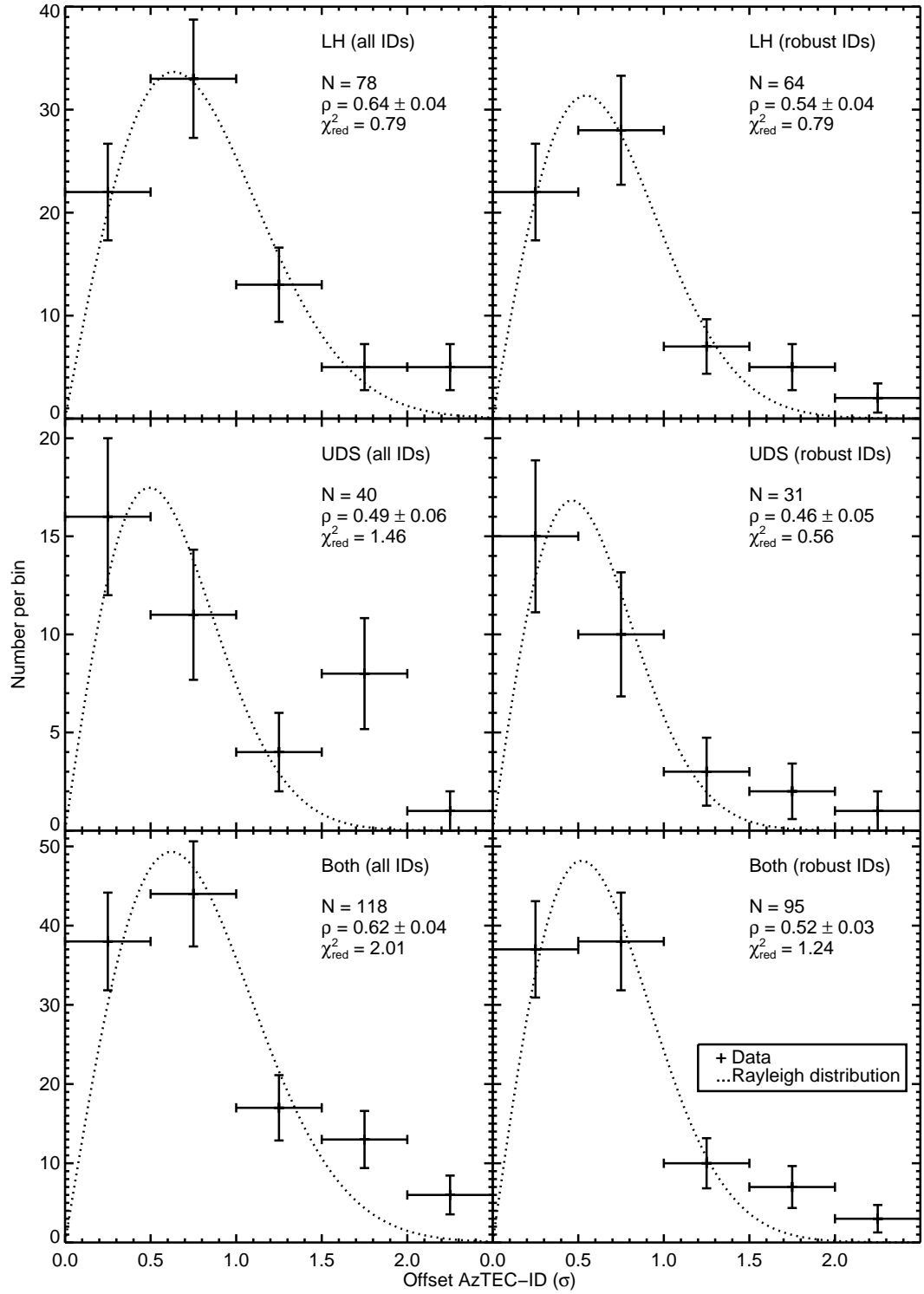


Figure 3. Distribution of the offsets of IDs from the AzTEC positions (crosses with Poissonian error bars; only the best ID is taken into account for each source) and the Rayleigh distribution (dotted lines), $R(r) \propto r \exp(-r^2/2\rho^2)$, expected to explain the data if offsets originate from the statistical positional uncertainty of the AzTEC sources. Each panel represents all or robust (category-1 $p < 0.05$) IDs, in the Lockman Hole, or the UDS field, or both. As in Biggs et al. (2011), for each ID the value of the offset is normalized to the 1σ AzTEC positional uncertainty, $\sigma = 0.6 \times \text{FWHM}/(\text{S/N})$ (Sec. 3.1). Hence, the value of ρ corresponds to the 1σ positional uncertainty of IDs expressed in the units of such calculated σ and hence should be equal to 1. The numbers given in each panel are lower, so likely our estimates of the AzTEC positional uncertainties are overestimated. This is not because for 20 sources we reset the search radius to 8 arcsec (2.5σ ; Sec. 3.1), as after we remove this limit the values of ρ increase only by < 0.05 . There is an indication that the distributions of all IDs exhibit a slight excess at higher offsets compared to the model and to the robust-only IDs, indicating that some of the category-2 and 3 IDs are not correct, but this difference is not statistically significant. For each panel the number of IDs and the reduced χ^2 of the fit of the Rayleigh distribution to the data are shown indicating that the offset distributions are consistent with the Rayleigh distribution, so the number of wrongly assigned IDs is small (as they should manifest themselves as a significant signal at larger offsets).

Table 2. The success rate of the identification process. The columns show: (1) field name; (2) the total number of AzTEC sources, (3) the number of sources with IDs having at least one association with $p < 0.05$ at radio, $24\mu\text{m}$, $8.0\mu\text{m}$ or $i - K$; (4) the number of sources with IDs having at least two associations with $0.05 < p < 0.1$; (5), the number of sources with IDs having only one potential counterpart with $0.05 < p < 0.1$; (6) the number of sources with no IDs; (7) the total number of sources covered by the optical map (i.e. those for which a photometric redshift could in principle be reliably estimated); (8) number (and percentage relative to number of sources covered b the optical map) of sources with an optical–near-infrared photometric redshift; (9) number of sources with category 1 and an optical–near-infrared photometric redshift.

Field (1)	N (2)	Cat 1 (3)	Cat 2 (4)	Cat 3 (5)	No ID (6)	N_{opt} (7)	z_{opt} (8)	Cat 1 with z_{opt} (9)
Lockman Hole	91	64 (70%)	7 (8%)	7 (8%)	13 (14%)	62	47 (76%)	39 (63%)
UDS	57	31 (54%)	1 (2%)	8 (14%)	17 (30%)	44	31 (70%)	24 (55%)
Both	148	95 (64%)	8 (5%)	15 (10%)	30 (20%)	106	78 (74%)	63 (59%)

Table 3. The success rate of the identification process for the five individual methods. The columns show: (1) field name; (2) the total number of AzTEC sources, (3) the number of sources with any 1.4 GHz ID; (4) the number of sources with a category-1 1.4 GHz ID; (5), (6) any / category-1 0.6 GHz IDs; (7), (8) any / category-1 $24\mu\text{m}$ IDs; (9) the number of sources covered by the IRAC map; (10), (11) any / category-1 $8.0\mu\text{m}$ IDs; (12) the number of sources covered by the i - and K -band maps; (13), (14) any / category-1 $i - K$ IDs.

Field (1)	N (2)	1.4 GHz IDs		0.6 GHz IDs		24 μm IDs		8.0 μm IDs			$i - K$ IDs		
		any (3)	Cat 1 (4)	any (5)	Cat 1 (6)	any (7)	Cat 1 (8)	N (9)	any (10)	Cat 1 (11)	N (12)	any (13)	Cat 1 (14)
LH	91	66 (73%)	50 (55%)	57 (63%)	46 (51%)	63 (69%)	43 (47%)	64	35 (55%)	24 (38%)	54	26 (48%)	18 (33%)
UDS	57	25 (44%)	21 (37%)	N/A	N/A	22 (39%)	16 (28%)	51	14 (27%)	5 (10%)	44	23 (52%)	13 (30%)
Both	148	91 (61%)	71 (49%)	N/A	N/A	85 (57%)	59 (40%)	115	49 (43%)	29 (25%)	98	49 (50%)	31 (32%)

found both robust radio and $i - K$ IDs, and found that they agreed in 19/23 cases (83%), providing reassurance that the $i - K$ method can be reliably used when the radio data are not deep enough.

The final success-rate of source identification is summarised in Table 2. The IDs have been divided into three categories. Category 1 is used for an ID which has a very low probability of chance association, $p < 0.05$ (p marked as bold in Tables B1 and B2 and a big symbol on Figs. B1 and B2). Category 2 denotes an ID selected at least twice by one of the radio, $24\mu\text{m}$ $8.0\mu\text{m}$ or $i - K$ methods with $0.05 < p < 0.1$, while category 3 indicates an ID that has been selected by only one of these methods with $0.05 < p < 0.1$.

The higher category-1 rate for the Lockman Hole can be primarily attributed to the slightly deeper radio data available in this field. Indeed, if the radio depth was degraded to the same as that available in the UDS field ($\simeq 45\mu\text{Jy}$, 5σ), then the category-1 ID percentage in the Lockman Hole would drop to 58%, very similar to that found within the UDS field. The impact of the depth of the radio data on the ID rate is further demonstrated by the fact that the final total AzTEC-SHADES SMG ID rate of $\simeq 80\%$ is surpassed only by the survey of Lindner et al. (2011), who benefitted from the ultra-deep radio data available only in the Lockman Owen field, which reaches down to an rms $\sigma_{1.4\text{GHz}} \simeq 2.7\mu\text{Jy}$ in the central regions.

The ID success-rate separately for each method is shown in Table 3. The radio and $24\mu\text{m}$ methods in the Lockman Hole deliver higher success-rate than in the UDS field due to deeper data in the former field (see Table 1). On the other hand, deeper optical data in the UDS field do not help to increase the success-rate for the $i - K$ method. This is because no $i - K$ ID in the UDS field is fainter than the 3σ limit of $K = 23.5$ mag in the Lockman Hole. However,

deeper data in the UDS field help to increase the fraction of IDs with redshifts (see Table 2).

To determine the redshift distribution of the AzTEC-SHADES sources we decided to select only one ID for each source. For the vast majority of cases this is straightforward. However, for some sources there is more than one apparently significant galaxy counterpart. To deal with these cases we have adopted a policy of selecting the ID with the greatest number of high-significance ($p < 0.05$) entries in Tables B1 and B2 or, if IDs have only been uncovered at a single wavelength, the ID with the lowest value of p . If this procedure did not select a single ID, then we looked for the ID with the greatest number of moderate-significance ($0.05 < p < 0.1$) entries. In principle, such multiple IDs may indicate that the AzTEC source is a blend of a few galaxies (e.g. Wang et al. 2011); higher-resolution submillimetre imaging is necessary to test this.

The frequency of multiple IDs is $\simeq 21 \pm 5\%$ (19/91) for the Lockman Hole and $\simeq 11 \pm 4\%$ (6/57) for the UDS field, where the errors reflect the Poissonian uncertainties. This is consistent with the rates found for SCUBA sources in the same fields ($\simeq 9 \pm 5\%$; Clements et al. 2008; $\simeq 19 \pm 5\%$; Ivison et al. 2007) and for AzTEC sources in GOODS-N ($\simeq 18 \pm 8\%$ Chapin et al. 2009) and GOODS-S ($\simeq 10 \pm 5\%$ Yun et al. 2012).

We identified two sources (AzUDS5 and 43) with statistically robust IDs corresponding to optically-bright galaxies with very low photometric redshifts ($z \simeq 0.45$ and $z \simeq 0.15$ respectively). Such low redshifts are completely inconsistent with their $1.1\text{mm}/24\mu\text{m}$ flux-density ratios for any known long-wavelength SED (see Fig. 7). In the case of AzUDS5 the angular offset between the radio position and the optical galaxy is 0.65 arcsec, suggesting that this is an example of galaxy lensing, and that the SMG lies at much higher red-

shift (e.g. Dunlop et al. 2004). We note this, but leave the redshift as it is since we do not currently possess any CO spectroscopy of this source which might help to determine the true redshift of this SMG (see e.g. Negrello et al. 2010). However, in the case of AzUDS43 we have identified a second, statistically-robust ID at $z \simeq 2.43$, 3.5 arcsec away from the bright low-redshift optical ID, and so we have adopted this ID and its photometric redshift in the determination of the redshift distribution.

To test the reliability of the IDs, in Fig. 3 we show the distribution of the offsets of IDs from the AzTEC positions. Similarly to Biggs et al. (2011), we fitted the Rayleigh distribution, $R(r) \propto r \exp(-r^2/2\rho^2)$, expected to explain the data if offsets originate from the statistical positional uncertainty of the AzTEC sources. For each ID the value of the offset is normalized to the 1σ AzTEC positional uncertainty equal to $\sigma = 0.6 \times \text{FWHM}/(\text{S/N})$ (Sec. 3.1). Hence the value of ρ corresponds to the 1σ positional uncertainty of IDs expressed in the units of such calculated σ and hence should be equal to 1. The derived values are lower, so likely our estimates of the AzTEC positional uncertainties are overestimated. This is not because for 20 sources we reset the search radius to 8 arcsec (2.5σ ; Sec. 3.1), as after we remove this limit the values of ρ increase only by < 0.05 . There is an indication that the distributions of all IDs exhibit a slight excess at higher offsets compared to the model and to the robust-only IDs, indicating that some of the category-2 and 3 IDs are not correct, but this difference is not statistically significant. From the reduced χ^2 values we conclude that the offset distributions are consistent with the Rayleigh distribution, so the number of wrongly assigned IDs is small (as they should manifest themselves as a significant signal at larger offsets).

5 REDSHIFTS

We have used the photometric redshift catalogues from Cirasuolo et al. (2007, 2010) and McLure et al. (2009) in the UDS field and have now produced an equivalent catalogue in the Lockman Hole East, albeit with larger uncertainties due to the shallower near-infrared data. All optical, near-IR and IRAC data were used in the fits. These catalogues have been produced using the HYPERZ package (Bolzonella et al. 2000) with the stellar population models of Bruzual & Charlot (2003) and a Chabrier (2003) initial mass function (IMF) with a mass range $0.1\text{--}100 M_\odot$. A double-burst star-formation history was assumed, but this choice has little impact on derived redshifts (as opposed to derived stellar masses; Michałowski et al. 2012). The metallicity was fixed at the solar value and reddening was calculated following the Calzetti et al. (2000) law within the range $0 \leq A_V \leq 6$. The HI absorption along the line of sight was included according to the prescription of Madau (1995).

The resulting photometric redshifts are given in Tables B1 and B2. For sources with multiple IDs, the ID used in the determination of the redshift distribution is marked in bold (see Section 4). For sources with no optical-infrared photometric redshift we provide a redshift estimate based on the 1.1 mm / 1.4 GHz ratio (shown in italics), adopting the average SED of SMGs from Michałowski et al. (2010a).

AzUDS48 is not covered by the radio map, so an esti-

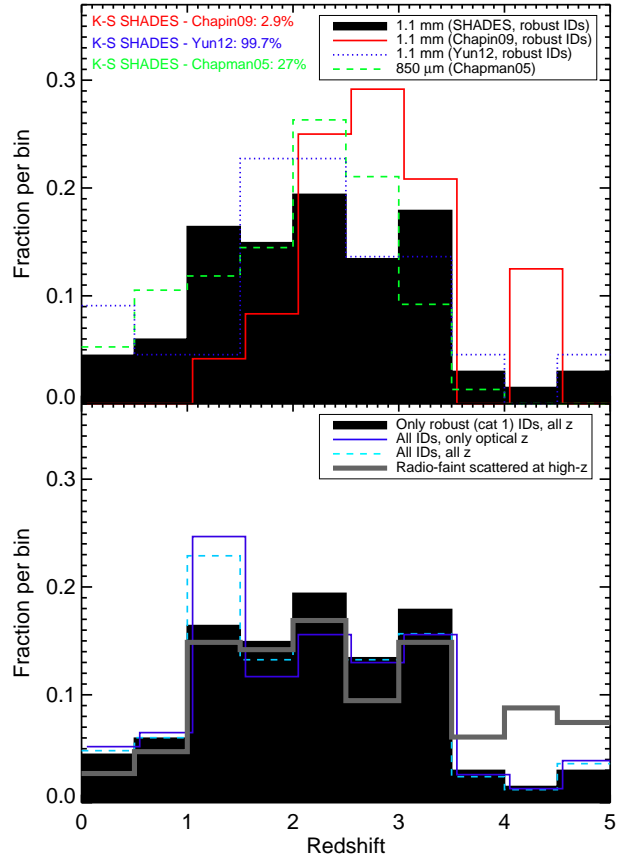


Figure 4. *Upper Panel:* the redshift distribution of 1.1 mm-selected galaxies in the SHADES fields with robust ($p < 0.05$) IDs using optical–near-infrared and 1.1 mm/1.4 GHz flux-density ratio redshifts (solid black histogram). In this plot any sources which only possess lower limits to their estimated redshifts have been excluded. Also shown are the redshift distributions of the 1.1 mm-selected galaxies in GOODS-N (solid red line; Chapin et al. 2009) and in GOODS-S (dotted blue line; Yun et al. 2012), as well as the spectroscopically-determined redshift distribution of 850 μm -selected galaxies reported by Chapman et al. (2005, green dashed line). The distributions peak at $z \simeq 0\text{--}3$ but contain objects over the redshift range $z \simeq 0\text{--}4$. The Kolmogorov-Smirnov test probabilities that samples are consistent with being drawn from the same parent population are indicated. The apparent difference at low redshifts between the SHADES and GOODS-N samples can be explained by the relatively small area of the latter survey (see Fig. 1 and Section 5). *Lower Panel:* An exploration of the robustness of the SHADES-AzTEC redshift distribution. The redshift distribution of the same set of robust IDs is again shown by the solid black histogram. The solid blue line represents only those IDs with optical–near-infrared photometric redshifts, while the dashed cyan line includes all IDs, irrespective of robustness (i.e. including categories 1, 2, and 3) and type of redshift. The grey thick line shows the redshift distribution for all AzTEC-SHADES SMGs, this time including those not detected at radio or optical wavelengths, which were scattered between $z = 5$ and the lower limit derived from the 1.1 mm/1.4 GHz flux-density limit using the SMG SED template from Michałowski et al. (2010a).

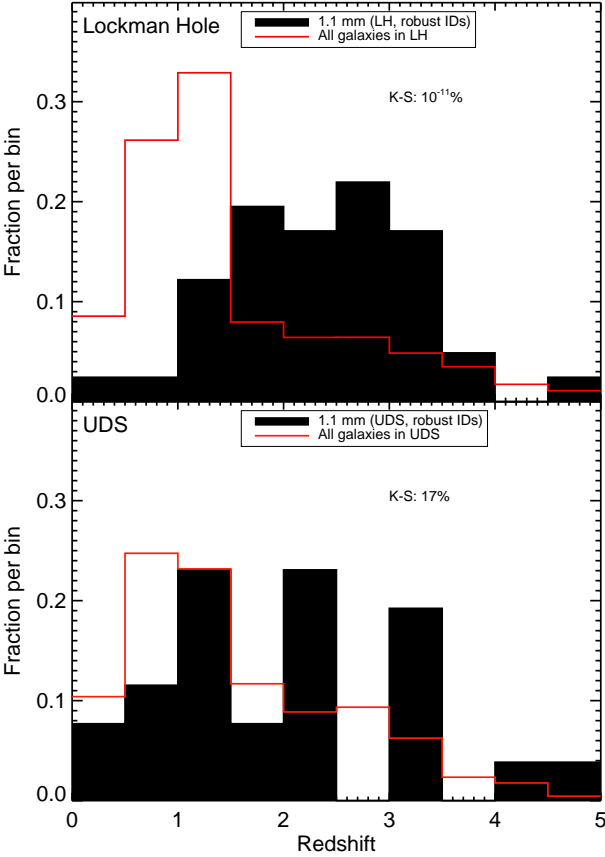


Figure 5. The redshift distribution of SHADES-AzTEC 1.1 mm-selected galaxies with robust ($p < 0.05$) IDs and either optical–near-infrared or 1.1 mm/1.4 GHz redshifts (solid black histograms), this time shown separately for the Lockman Hole field (upper panel) and the UDS field (lower panel). Sources with only lower limits to their estimated redshifts were excluded. Also shown for comparison are the redshift distributions of all the optical/near-infrared/*Spitzer* selected galaxies in the two survey fields (solid red lines). The Kolmogorov-Smirnov test probability that the samples on each panel are drawn from the same parent population are indicated. The AzTEC population in the Lockman Hole is not consistent with the general field galaxy population. The all galaxy samples (red lines) are different in both fields due to different optical depths, i.e. the i -band data is $\simeq 1.5$ mag deeper in the UDS field (Table 1), so the high redshift tail is much more pronounced in this field.

mate of its redshift has been deduced from its 1.1 mm/24 μm flux-density ratio (see third panel of Fig. 7).

The accuracy of the photometric catalogue of Cirasuolo et al. (2010) is excellent, with a mean $\Delta z/(1 + z_{\text{spec}}) = 0.008 \pm 0.034$. For 9 AzTEC sources with spectroscopic redshift (see appendix A) we derived a mean $\Delta z/(1 + z_{\text{spec}}) = -0.06 \pm 0.20$, also consistent with zero.

The median redshift (and 68% bootstrap error) of AzTEC-SHADES sources in the Lockman Hole field is $z_{\text{med}} \simeq 2.25^{+0.25}_{-0.21}$, in the UDS field it is $z_{\text{med}} \simeq 1.64^{+0.63}_{-0.28}$, and for the full combined sample it is $z_{\text{med}} \simeq 2.19^{+0.10}_{-0.30}$.

To date, only eleven SMGs have been shown to lie at $z > 4$ (Coppin et al. 2009; Capak et al. 2008, 2011; Schinnerer et al. 2008; Daddi et al. 2009b,a; Knudsen et al. 2008, 2010; Riechers et al. 2010; Cox et al.

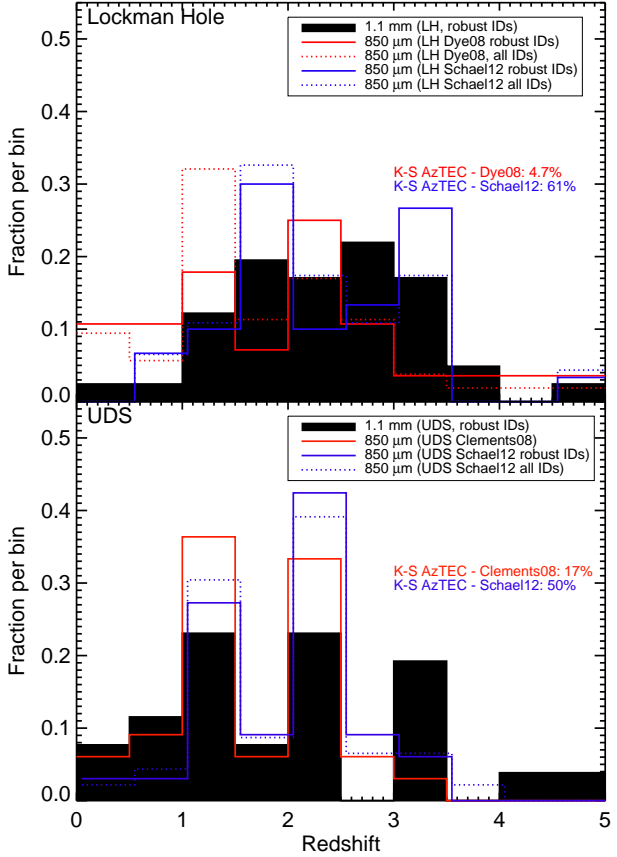


Figure 6. The redshift distribution of 1.1 mm-selected galaxies in the Lockman Hole (upper panel) and the UDS (lower panel) fields with robust ($p < 0.05$) IDs and optical–near-infrared or 1.1 mm/1.4 GHz flux-density ratio redshifts (solid black histograms). Sources with only lower limits to their estimated redshifts were excluded. Also shown in this figure are the redshift distributions derived for the SHADES-SCUBA 850 μm -selected galaxies in (sub regions of) the same fields (robust IDs: solid red lines; all IDs: dotted red line; Dye et al. 2008; Clements et al. 2008, Schael et al. in prep.). The Kolmogorov-Smirnov test probability that the samples in each panel are drawn from the same populations are indicated. The distributions of the 1.1 mm- and 850 μm -selected populations are consistent, although there is an indication that the 1.1 mm selection results in slightly higher redshifts. Combining the AzTEC and SCUBA samples in each field reveals a statistically significant difference between the inferred redshift distributions of SMGs in the Lockman Hole and UDS fields (see Section 7).

2011; Smolčić et al. 2011; Combes et al. 2012; Walter et al. 2012). We have identified five AzTEC-SHADES sources ($\simeq 5\%$) with photometric redshifts $z \gtrsim 4$ (AzLOCK6, AzLOCK38, AzUDS11, AzUDS32, AzUDS54). However, for all of these galaxies the uncertainties in the photometric redshifts are significant, and lower-redshift ($z \simeq 2$) solutions cannot be excluded. In addition, several AzTEC sources that are unambiguously detected in the radio (and in some cases also at 8.0 μm) remain undetected in the optical imaging (AzLOCK36, AzLOCK38, AzLOCK71, AzLOCK81, AzLOCK91, AzUDS25, AzUDS40 and AzUDS57). These sources are thus also candidates for very high-redshift (or highly dust-obscured) galaxies.

The success rate of redshift determination is summa-

rized in Table 2 (column 8). Excluding AzTEC sources which are not covered by the necessary optical-infrared data, we obtained optical photometric redshift estimates for $\simeq 75\%$ of sources (i.e. out of the 106 AzTEC sources which lie within the area covered by the deep optical/near-infrared imaging, we obtained optical photometric redshift estimates for 78; out of them 63 have category-1 IDs) or $\simeq 60\%$ if only category-1 IDs are taken into account. This is the most complete redshift information achieved to date for an unbiased sample of SMGs. For the remaining 28 ($\simeq 25\%$) SMGs no ID was selected, or the radio ID does not possess an optical counterpart, so the optical redshift could not be obtained.

The redshift distribution of the AzTEC-SHADES sources is shown in Fig. 4, where it is compared with that displayed by similar (but smaller) samples of SMGs selected in GOODS-N (Chapin et al. 2009) and in GOODS-S (Yun et al. 2012), as well as with the spectroscopically-determined redshift distribution of a somewhat heterogeneous selection of $850\text{ }\mu\text{m}$ -selected galaxies reported by Chapman et al. (2005). The redshift distribution of the AzTEC-SHADES sources is peaked at $z \simeq 2\text{--}2.5$, but has a high-redshift tail (extending to at least $z \simeq 4$) as well as a significant intermediate-redshift population.

As perhaps expected, the redshift distribution of AzTEC-SHADES sources is similar to that previously derived for $850\text{ }\mu\text{m}$ -selected galaxies, and to that displayed by the AzTEC-ASTE sample in GOODS-S; the Kolmogorov-Smirnov (K-S) test indicates that the redshift distribution of the AzTEC-SHADES sources and that reported by Chapman et al. (2005) and Yun et al. (2012) are consistent with the hypothesis that all three samples are drawn from the same parent population (Fig. 4).

However, our redshift distribution is slightly different than that reported by Chapin et al. (2009) in GOODS-N. The K-S test yields a probability of only $p \simeq 2.9\%$ that the AzTEC-SHADES and GOODS-N AzTEC samples are drawn from the same population (i.e. the difference is at the 2.2σ level). The probability increases to $\simeq 15\%$ (no significant difference) when $z < 1$ SMGs in the AzTEC-SHADES sample are removed.

To further explore the likelihood of this difference, we divided each of our fields into four equal parts, each similar in size to the GOODS-N field and analysed their redshift distributions separately (see Fig. 1). We found that in 50% (4/8) of such small fields we did not detect any $z < 1$ source. To confirm this we performed a Monte-Carlo simulation by selecting in both of our fields 100 000 randomly-located sub-fields with areas equal to that of Chapin et al. (2009). We found that $\simeq 60\%$ of these sub-fields did not contain any $z < 1$ object. This suggests that the sample of Chapin et al. (2009) may miss the lower-redshift population due to its small area and advocates for using larger fields to obtain a representative sample of millimeter-selected galaxies. Further support for field-to-field variation is provided by the differences in millimeter number counts in different fields, in particular by the fact that GOODS-N field has systematically higher number counts compared to other fields (Scott et al. 2010, 2012).

The lower panel of Fig. 4 shows that the form of the derived redshift distribution is essentially unaffected by whether one restricts the redshift information to only optical-infrared photometric redshifts, or alternatively in-

clude all available redshift information (i.e. including estimates based on mm-radio colour). However, when we include the category 2 and 3 IDs, then a spike at $z \simeq 1\text{--}1.5$ appears. At least some of these less-robust IDs are likely mis-identifications, because, as shown on Fig. 5, the redshift distribution of all optical/near-infrared galaxies in both the survey fields peaks at $z \simeq 1$.

Fig. 6 shows the redshift distribution of the robust ($p < 0.05$) IDs of the AzTEC sources separately in the Lockman Hole and the UDS fields compared with that of the $850\text{ }\mu\text{m}$ -selected SMGs in (smaller sub-regions of) the same fields (Dye et al. 2008; Clements et al. 2008, Schael et al. in prep.). Applying the K-S test we found that, within each field, the redshift distributions of the 1.1 mm - and $850\text{ }\mu\text{m}$ -selected populations are completely consistent (the significance values, p , are indicated in Fig. 6), although (unsurprisingly) there is a tendency for the 1.1 mm selected SMGs to lie at slightly higher redshifts. This consistency is not driven by the fact that both populations are composed of the same galaxies; the AzTEC images cover significantly larger areas than the SCUBA maps, to somewhat shallower effective depths (and different completeness), and consequently there are only 13 and 6 sources in common between the 1.1 mm and $850\text{ }\mu\text{m}$ -selected samples in the Lockman Hole and UDS fields, respectively (see Fig. 1, Fig. 2 and appendix A). The implications of this result are explored further below in Section 7.

In principle AGN contamination may influence our photometric redshift estimates, which are based on purely star-forming templates. Hainline et al. (2009, 2011) claimed a significant AGN contribution to the IRAC fluxes of SMGs, however Michałowski et al. (2012) found that the AGN contamination is unlikely to influence the SED modelling. Additionally, the photometric errors of IRAC fluxes are typically $\sim 10\%$, significantly larger than that of our deep optical and near-IR data, so even if the AGN contamination was significant at IRAC wavelengths, these data should not influence the derived photometric redshifts significantly. Similarly, Wardlow et al. (2011) found that the exclusion of the $8.0\text{ }\mu\text{m}$ data does not significantly change the derived photometric redshifts of SMGs.

6 FLUX RATIOS

In order to verify that these redshift estimates are consistent with the available photometry, in Fig. 7 we show 1.1 mm flux density, as well as the three flux-density ratios $1.1\text{ mm}/1.4\text{ GHz}$, $1.1\text{ mm}/24\text{ }\mu\text{m}$, and $24\text{ }\mu\text{m}/1.4\text{ GHz}$ plotted against redshift for all the identified AzTEC-SHADES sources (utilising the best ID for each source, determined as described above). The lower 3 panels also show the expected redshift dependence of the appropriate flux-density ratio as predicted by the SED of an average SMG and individual SMGs (Michałowski et al. 2010a), the SEDs of local galaxies (a ULIRG, a starburst and spirals; Silva et al. 1998) and the SEDs of local ULIRGs/AGNs (Vega et al. 2008). Filled/thick symbols indicate category 1 (robust, $p < 0.05$) IDs, and the smaller symbols indicate that the $1.1\text{ mm}/1.4\text{ GHz}$ flux-ratio redshift estimator was used due to a lack of optical-infrared photometry.

The top panel shows that the brightest AzTEC

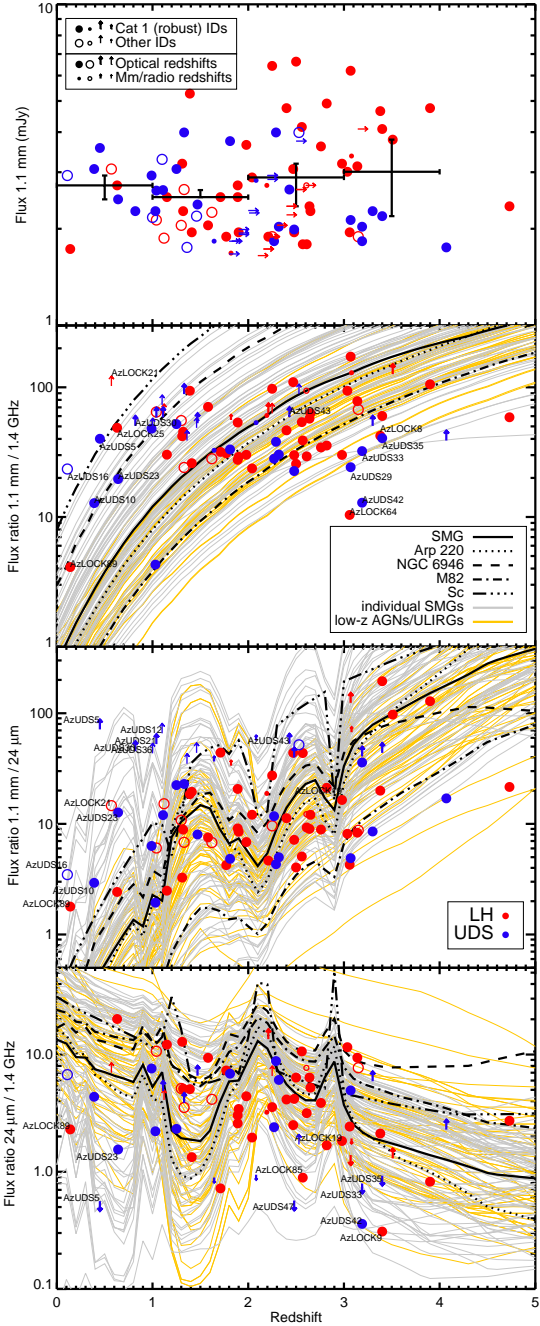


Figure 7. 1.1 mm flux densities (medians in four redshift bins with 68% bootstrap errors are shown as *thick crosses*) and the 1.1 mm/1.4 GHz, 1.1 mm/24 μm and 24 μm /1.4 GHz flux-density ratios plotted against redshift for all the AzTEC-SHADES sources (the best ID is shown for each source) presented in Tables B1 and B2 (*colour symbols*; red: Lockman Hole; blue: UDS field). *Circles* denote detections at both bands, whereas *upward and downward arrows* denote non-detections at one of the wavelengths. *Filled circles and thick arrows* indicate category 1 (robust; $p < 0.05$) IDs, whereas *open circles and thin arrows* indicate other IDs. *Big symbols* indicate sources with optical–near-infrared photometric redshifts, whereas *small symbols* indicate that 1.1 mm/1.4 GHz redshift estimator was used due to a lack of optical/infrared photometry. For comparison, the predicted redshift evolution of the flux-density ratios calculated using the SEDs of an average SMG and individual SMGs (Michałowski et al. 2010a), of local galaxies (Silva et al. 1998) and local ULIRGs/AGNs (Vega et al. 2008) are shown (*lines*).

sources preferentially lie at higher redshifts (consistent with Ivison et al. 2002; Wall et al. 2008; Marsden et al. 2011); all but one of the sources brighter than 4 mJy are at $z > 2$ (i.e. the upper-left corner of this panel is almost empty). However, this does not mean that the median flux densities of AzTEC sources is higher at higher redshifts (see thick crosses on this panel).

For sources with no radio detections the derived 1.1 mm/1.4 GHz redshifts are lower limits. As can be seen from the arrows in the top panel of Fig. 7, the derived limits do not allow us to place very strong redshift constraints on these sources (typically $z > 2$). Hence, in general, the lack of a radio detection does not imply that such sources lie at substantially higher redshifts than the radio-detected subset; given the 1.1 mm flux densities of the sources, and the depth of the available radio data, a radio-blank SMG could be at $z < 3$ or even at $z < 1.5$ if its dust is very cold (similar to spiral galaxies).

The second panel of Fig. 7 reveals the redshift dependence of the implied dust temperature of the galaxies within the AzTEC-SHADES sample (assuming the photometric redshifts are broadly correct). Namely, the 1.1 mm / 1.4 GHz flux ratios of the AzTEC sources do not change with redshift, implying that those at $z < 1.5$ are cooler (consistent with the SEDs of Sc spiral and NGC 6946), whereas those at higher redshifts are hotter (consistent with the SEDs of an average SMG, Arp 220 and M82).

Finally, the bottom two panels of Fig. 7 show that the vast majority of the AzTEC-SHADES sources lie within the regions spanned by the range of SED models considered (only for the sources denoted as small symbols were the redshifts in fact derived from the fluxes plotted in this figure). This indicates that our optical photometric redshift estimates are reasonable, in the sense that they are generally consistent with the anticipated range of 1.1 mm/24 μm and 24 μm /1.4 GHz flux-density ratios. We note that radio-loud AGN from Shang et al. (2011) have 1.1 mm/1.4 GHz and 24 μm /1.4 GHz flux-density ratios of 0.01–0.03 in the redshift range 0–5. Hence the sources which lie below the SED locus in panels 2 (AzLOCK64 and AzUDS42, both category-1 IDs) may be readily explained by some contribution from AGN synchrotron radiation at radio wavelengths.

7 LARGE-SCALE STRUCTURES

With only photometric redshifts it is difficult to study the large-scale structures traced by SMGs. However, as is evident from Fig. 6, the redshift distributions of the AzTEC sources in both the Lockman Hole and UDS fields are strikingly similar to that displayed by the SCUBA sources in the same fields, even though SCUBA covered much smaller sub-regions within these fields (see Fig. 1 and Fig. 2) and there are only 13 and 6 sources in common in the Lockman Hole and UDS samples respectively. Indeed, the K-S test shows that the AzTEC and SCUBA sources in each field are fully consistent with being drawn from the same population ($p = 61\%$ in the Lockman Hole, and $p = 50\%$ in UDS field). Interestingly this consistency between the redshift distributions of the AzTEC and SCUBA sources *within* each field is better than the consistency of the redshift distributions *between* the two SHADES fields (for AzTEC Lockman

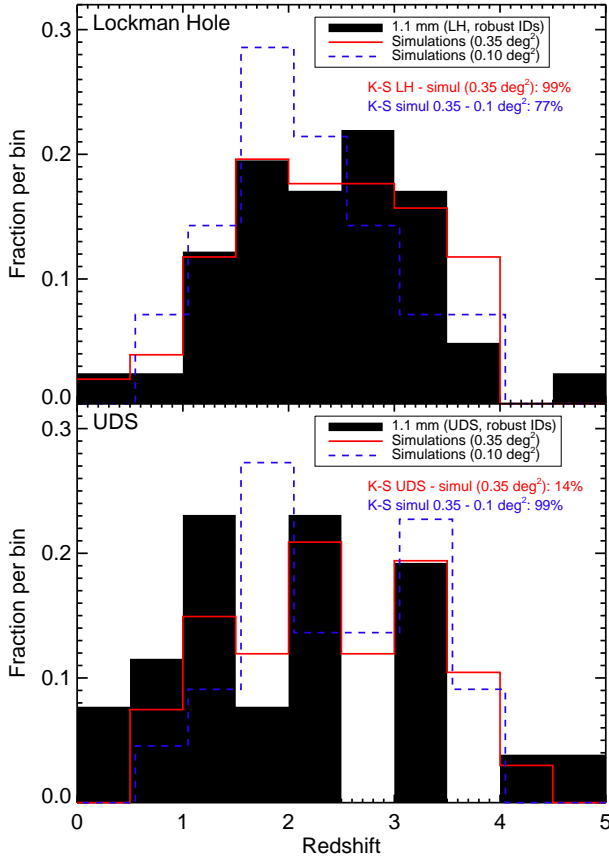


Figure 8. The redshift distribution of 1.1 mm-selected galaxies in the Lockman Hole (upper panel) and the UDS (lower panel) fields with robust ($p < 0.05$) IDs and optical–near-infrared or 1.1 mm/1.4 GHz flux-density ratio redshifts (solid black histograms). Sources with only lower limits to their estimated redshifts were excluded. Also shown in this figure are the redshift distributions of simulated galaxies (Croton et al. 2006) in random 0.35 (AzTEC-like, red solid lines) and 0.1 deg $^{-2}$ (SCUBA-like, blue dotted lines) fields. For each panel these simulated fields were chosen out of 1000 random fields to best represent the distributions of real SMGs. The Kolmogorov–Smirnov test probability that the real and simulated galaxies (as well as simulated galaxies in fields with different sizes) in each panel are drawn from the same populations are indicated.

Hole vs AzTEC UDS $p = 16\%$, while for SCUBA Lockman Hole vs SCUBA UDS $p = 14\%$). This difference starts to become statistically significant if we combine the AzTEC and SCUBA samples in each field (i.e. if for each field we construct a combined catalogue containing both AzTEC and SCUBA sources in that field), and then repeat the redshift distribution comparison. This yields a probability that the redshift distributions of the combined (AzTEC+SCUBA) Lockman Hole and UDS samples are drawn from the same population of only 2% (a statistical difference between the AzTEC source population in the Lockman Hole and UDS fields was also noted by Austermann et al. 2010, who showed that the 1.1 mm number counts at high fluxes in the Lockman Hole are higher than in the UDS field; see their Fig. 8 as well as the top panel of Fig. 7 in this paper).

This result suggests that the large-scale structures traced by the AzTEC survey are significantly different be-

tween the Lockman Hole and UDS fields, and the AzTEC and SCUBA SMG samples are tracing *the same* large-scale structures within each field. This latter result implies that these structures extend from the $\simeq 0.3$ deg areas sampled by SCUBA to at least the $\simeq 0.7$ deg scales traced by each AzTEC-SHADES survey field. These angular scales correspond to 10–20 Mpc at $z = 1.25$ and 2.25, (the redshifts of the prominent peaks seen in the redshift distribution of the UDS SMGs). Alternatively, large-scale structure at lower redshifts may also contribute to the appearance of this effect, as Aretxaga et al. (2011) showed that the clustering of the foreground galaxies at $z \simeq 0.7$ is correlated with the position of bright SMGs in the COSMOS field.

In order to investigate whether large-scale structure is in fact expected to produce the variations we see between the Lockman Hole and UDS fields, we have analysed a 900 deg 2 light cone of simulated galaxies at $z = 0$ –5 with $SFR > 100 M_{\odot} \text{ yr}^{-1}$ (Croton et al. 2006)⁵, produced in a semi-analytic model based on the Millennium simulation (Springel et al. 2005). Interestingly, to match the AzTEC number counts and produce a redshift distribution which peaks at $z \sim 2$ –3 rather than rising monotonically out to $z > 5$, we had to apply a stellar mass cut to the simulation to confine our analysis to galaxies with $M_* > 10^{11} M_{\odot}$. Confining our attention to this high-mass regime, we then randomly chose 1000 0.35 deg 2 fields from within this light-cone and, for each pair of fields, calculated the K-S probability that the galaxy redshift distributions are drawn from the same population. We found that $\simeq 10\%$ of field pairs were inconsistent at a K-S probability level of $< 5\%$ and that $\simeq 25\%$ of pairs were inconsistent at a probability level $< 15\%$. Hence, the level of inconsistency we found between the Lockman Hole and the UDS AzTEC source populations is broadly as predicted by the simulation, providing some support for the interpretation that it is indeed due to large-scale structure.

For illustrative purposes, Fig. 8 shows the redshift distributions of the random fields which yielded the highest K-S probability of being consistent with the Lockman Hole and UDS fields (99 and 14% respectively). Thus, the light cones produced using this particular simulation can certainly yield SMG number densities and redshift distributions consistent with those seen in both AzTEC-SHADES fields. However, it is clear that the SMG redshift distribution in the Lockman Hole is much more typical of what is found within the simulations than is the redshift distribution in the UDS field. Specifically, $\simeq 70\%$ of the simulated 0.35 deg 2 AzTEC surveys yield a K-S probability $> 5\%$ that their SMG redshift distribution is consistent with that of the AzTEC sources in the Lockman Hole, but this is true for only $\simeq 1\%$ of the simulated fields when compared to the UDS SMG redshift distribution. Thus, *for this particular simulation* it would appear the the observed redshift distribution in the UDS is relatively unusual, albeit not unfeasible so.

Our analysis of this simulation also indicates that it is unsurprising that the redshift distributions of the SHADES-SCUBA and SHADES-AzTEC sources within a given field should be in good agreement (Fig. 6), as the overlapping 1.1 mm and 850 μm surveys, while differing in size, wave-

⁵ <http://tao.it.swin.edu.au/mock-galaxy-factory/>

length and depth, are tracing the same large scale structures (see Fig. 8). Namely, virtually all random 0.35 deg^2 fields have the K-S probability above 5% that their redshift distribution is consistent with that of overlapping 0.1 deg^2 fields.

Finally we note that the fact the two well-separated SHADES fields, despite each covering $\simeq 0.35 \text{ deg}^2$, still yield significantly different redshift SMG distributions serves to reinforce the importance of completing SMG surveys over several square degrees in order to overcome cosmic variance and obtain a complete and representative view of the number density, redshift distribution and evolution of SMGs in the context of the general high-redshift galaxy population.

8 CONCLUSIONS

We have used the deep optical-to-radio multi-wavelength data in the SHADES Lockman East and SXDF/UDS and fields to obtain galaxy identifications for $\simeq 64\%$ ($\simeq 80\%$ including tentative identifications) of the 148 AzTEC-SHADES 1.1 mm sources reported by Austermann et al. (2010), exploiting deep radio and $24 \mu\text{m}$ data complemented by methods based on $8 \mu\text{m}$ flux-density and red optical-infrared ($i - K$) colour. This unusually high identification rate can be attributed to the relatively bright millimetre-wavelength flux-density threshold, combined with the relatively deep supporting multi-frequency data now available in these two well-studied fields. We have further exploited the optical–mid-infrared–radio data to derive a $\simeq 60\%$ ($\simeq 75\%$ including tentative identifications) complete redshift distribution for the AzTEC-SHADES sources, yielding a median redshift of $z \simeq 2.2$, with a high-redshift tail extending to at least $z \simeq 4$.

Despite the larger area probed by the AzTEC survey relative to the original SCUBA SHADES imaging, the redshift distribution of the AzTEC sources is consistent with that displayed by the SCUBA sources, and reinforces tentative evidence that the redshift distribution of mm/sub-mm sources in the Lockman Hole field is significantly different from that found in the SXDF/UDS field. Comparison with simulated surveys of similar scale extracted from semi-analytic models based on the Millennium simulation indicates that this is as expected if the mm/sub-mm sources are massive ($M > 10^{11} M_\odot$) star-forming galaxies tracing large-scale structures over scales of 10–20 Mpc. This confirms the importance of surveys covering several square degrees (as now underway with SCUBA2) to obtain representative samples of bright (sub)mm-selected galaxies.

ACKNOWLEDGMENTS

We thank Joanna Baradziej, Helmut Dannerbauer and our anonymous referee for comments and suggestions and Darren Croton and Pratika Dayal for help with numerical simulations.

MJM acknowledges the support of the Science and Technology Facilities Council. JSD acknowledges the support of the Royal Society via a Wolfson Research Merit award, and also the support of the European Research Council via the award of an Advanced Grant. KIC acknowledges

the Leverhulme Trust for support through the award of an Early Career Fellowship. IRS acknowledges support from STFC and the Leverhulme Trust. KSS is supported by the National Radio Astronomy Observatory, which is a facility of the National Science Foundation operated under cooperative agreement by Associated Universities, Inc. Support for this work was provided in part by NSF grant AST 05-40852 and a grant from the Korea Science & Engineering Foundation (KOSEF) under a cooperative Astrophysical Research Center of the Structure and Evolution of the Cosmos (ARC-SEC).

This research has made use of the Tool for Operations on Catalogues And Tables (TOPCAT; Taylor 2005): www.starlink.ac.uk/topcat/; SAOImage DS9, developed by Smithsonian Astrophysical Observatory (Joye & Mandel 2003); SExtractor: Software for source extraction (Bertin & Arnouts 1996), and NASA’s Astrophysics Data System Bibliographic Services.

REFERENCES

- Amblard A., et al., 2010, *A&A*, 518, L9
- Aretxaga I., Hughes D.H., Chapin E.L., Gaztañaga E., Dunlop J.S., Ivison R.J., 2003, *MNRAS*, 342, 759
- Aretxaga I., et al., 2007, *MNRAS*, 379, 1571
- Aretxaga I., et al., 2011, *MNRAS*, 415, 3831
- Ashby M.L.N., et al., 2006, *ApJ*, 644, 778
- Austermann J.E., et al., 2009, *MNRAS*, 393, 1573
- Austermann J.E., et al., 2010, *MNRAS*, 401, 160
- Barger A.J., Cowie L.L., Sanders D.B., Fulton E., Taniguchi Y., Sato Y., Kawara K., Okuda H., 1998, *Nat*, 394, 248
- Barger A.J., Cowie L.L., Sanders D.B., 1999, *ApJ*, 518, L5
- Barger A.J., Cowie L.L., Richards E.A., 2000, *AJ*, 119, 2092
- Barger A.J., Cowie L.L., Steffen A.T., Hornschemeier A.E., Brandt W.N., Garmire G.P., 2001, *ApJ*, 560, L23
- Barger A.J., Cowie L.L., Brandt W.N., Capak P., Garmire G.P., Hornschemeier A.E., Steffen A.T., Wehner E.H., 2002, *AJ*, 124, 1839
- Bertin E., Arnouts S., 1996, *A&A Suppl.*, 117, 393
- Bertoldi F., et al., 2007, *ApJS*, 172, 132
- Béthermin M., et al., 2012, *A&A*, 542, A58
- Biggs A.D., et al., 2011, *MNRAS*, 413, 2314
- Bolzonella M., Miralles J., Pelló R., 2000, *A&A*, 363, 476
- Borys C., Smail I., Chapman S.C., Blain A.W., Alexander D.M., Ivison R.J., 2005, *ApJ*, 635, 853
- Bruzual G., Charlot S., 2003, *MNRAS*, 344, 1000
- Bussmann R.S., et al., 2012, *ApJ*, 744, 150
- Calzetti D., Armus L., Bohlin R.C., Kinney A.L., Koornneef J., Storchi-Bergmann T., 2000, *ApJ*, 533, 682
- Capak P., et al., 2008, *ApJ*, 681, L53
- Capak P.L., et al., 2011, *Nat*, 470, 233
- Caputi K.I., Dole H., Lagache G., McLure R.J., Dunlop J.S., Puget J., Le Floc'h E., Pérez-González P.G., 2006, *A&A*, 454, 143
- Caputi K.I., Cirasuolo M., Dunlop J.S., McLure R.J., Farrah D., Almaini O., 2011, *MNRAS*, 413, 162
- Chabrier G., 2003, *ApJ*, 586, L133
- Chapin E.L., et al., 2009, *MNRAS*, 398, 1793
- Chapin E.L., et al., 2011, *MNRAS*, 411, 505

- Chapman S.C., Richards E.A., Lewis G.F., Wilson G., Barger A.J., 2001, ApJ, 548, L147
- Chapman S.C., et al., 2003, ApJ, 585, 57
- Chapman S.C., Blain A.W., Smail I., Ivison R.J., 2005, ApJ, 622, 772
- Cirasuolo M., et al., 2007, MNRAS, 380, 585
- Cirasuolo M., McLure R.J., Dunlop J.S., Almaini O., Foucaud S., Simpson C., 2010, MNRAS, 401, 1166
- Clements D.L., et al., 2008, MNRAS, 387, 247
- Combes F., et al., 2012, A&A, 538, L4
- Condon J.J., 1992, ARA&A, 30, 575
- Coppin K., Halpern M., Scott D., Borys C., Chapman S., 2005, MNRAS, 357, 1022
- Coppin K., et al., 2006, MNRAS, 372, 1621
- Coppin K., et al., 2008, MNRAS, 384, 1597
- Coppin K., et al., 2010, ApJ, 713, 503
- Coppin K.E.K., et al., 2009, MNRAS, 395, 1905
- Cox P., et al., 2011, ApJ, 740, 63
- Croton D.J., et al., 2006, MNRAS, 365, 11
- Daddi E., Dannerbauer H., Krips M., Walter F., Dickinson M., Elbaz D., Morrison G.E., 2009a, ApJ, 695, L176
- Daddi E., et al., 2009b, ApJ, 694, 1517
- Dannerbauer H., Lehnert M.D., Lutz D., Tacconi L., Bertoldi F., Carilli C., Genzel R., Menten K.M., 2004, ApJ, 606, 664
- Dannerbauer H., et al., 2010, ApJ, 720, L144
- Downes A.J.B., Peacock J.A., Savage A., Carrie D.R., 1986, MNRAS, 218, 31
- Downes T.P., Welch D., Scott K.S., Austermann J., Wilson G.W., Yun M.S., 2012, MNRAS, 423, 529
- Dunlop J.S., Peacock J.A., Savage A., Lilly S.J., Heasley J.N., Simon A.J.B., 1989, MNRAS, 238, 1171
- Dunlop J.S., et al., 2004, MNRAS, 350, 769
- Dunlop J.S., et al., 2010, MNRAS, 408, 2022
- Dye S., et al., 2006, MNRAS, 372, 1227
- Dye S., et al., 2008, MNRAS, 386, 1107
- Eales S., et al., 2009, ApJ, 707, 1779
- Egami E., et al., 2004, ApJS, 154, 130
- Engel H., et al., 2010, ApJ, 724, 233
- Ezawa H., Kawabe R., Kohno K., Yamamoto S., 2004, In: J. M. Oschmann Jr. (ed.) Society of Photo-Optical Instrumentation Engineers (SPIE) Conference Series, vol. 5489 of Society of Photo-Optical Instrumentation Engineers (SPIE) Conference Series, 763–772
- Ezawa H., et al., 2008, In: Society of Photo-Optical Instrumentation Engineers (SPIE) Conference Series, vol. 7012 of Society of Photo-Optical Instrumentation Engineers (SPIE) Conference Series
- Furusawa H., et al., 2008, ApJS, 176, 1
- Greve T.R., Ivison R.J., Bertoldi F., Stevens J.A., Dunlop J.S., Lutz D., Carilli C.L., 2004, MNRAS, 354, 779
- Greve T.R., et al., 2005, MNRAS, 359, 1165
- Greve T.R., Pope A., Scott D., Ivison R.J., Borys C., Conselice C.J., Bertoldi F., 2008, MNRAS, 389, 1489
- Hainline L.J., Blain A.W., Smail I., Frayer D.T., Chapman S.C., Ivison R.J., Alexander D.M., 2009, ApJ, 699, 1610
- Hainline L.J., Blain A.W., Smail I., Alexander D.M., Armus L., Chapman S.C., Ivison R.J., 2011, ApJ, 740, 96
- Hatsukade B., et al., 2010, ApJ, 711, 974
- Hatsukade B., et al., 2011, MNRAS, 411, 102
- Hayward C.C., Kereš D., Jonsson P., Narayanan D., Cox T.J., Hernquist L., 2011, ApJ, 743, 159
- Holland W.S., et al., 1999, MNRAS, 303, 659
- Hughes D.H., et al., 1998, Nat, 394, 241
- Ibar E., Ivison R.J., Biggs A.D., Lal D.V., Best P.N., Green D.A., 2009, MNRAS, 397, 281
- Ibar E., Ivison R.J., Best P.N., Coppin K., Pope A., Smail I., Dunlop J.S., 2010, MNRAS, 401, L53
- Ivison R.J., et al., 2002, MNRAS, 337, 1
- Ivison R.J., et al., 2005, MNRAS, 364, 1025
- Ivison R.J., et al., 2007, MNRAS, 380, 199
- Joye W.A., Mandel E., 2003, In: H. E. Payne, R. I. Jedrzejewski, & R. N. Hook (ed.) Astronomical Data Analysis Software and Systems XII, vol. 295 of Astronomical Society of the Pacific Conference Series, 489
- Knudsen K.K., Kneib J.P., Egami E., 2008, In: Chary R.R., Teplitz H.I., Sheth K. (eds.) Infrared Diagnostics of Galaxy Evolution, vol. 381 of Astronomical Society of the Pacific Conference Series, 372
- Knudsen K.K., Kneib J., Richard J., Petitpas G., Egami E., 2010, ApJ, 709, 210
- Lawrence A., et al., 2007, MNRAS, 379, 1599
- Lindner R.R., et al., 2011, ApJ, 737, 83
- Madau P., 1995, ApJ, 441, 18
- Marsden G., et al., 2011, MNRAS, 417, 1192
- McLure R.J., Cirasuolo M., Dunlop J.S., Foucaud S., Almaini O., 2009, MNRAS, 395, 2196
- Michałowski M., Hjorth J., Watson D., 2010a, A&A, 514, A67
- Michałowski M.J., Watson D., Hjorth J., 2010b, ApJ, 712, 942
- Michałowski M.J., Dunlop J.S., Cirasuolo M., Hjorth J., Hayward C.C., Watson D., 2012, A&A, 541, A85
- Miyazaki S., et al., 2002, PASJ, 54, 833
- Mortier A.M.J., et al., 2005, MNRAS, 363, 563
- Negrello M., et al., 2010, Science, 330, 800
- Perera T.A., et al., 2008, MNRAS, 391, 1227
- Pope A., et al., 2006, MNRAS, 370, 1185
- Riechers D.A., et al., 2010, ApJ, 720, L131
- Santini P., et al., 2010, A&A, 518, L154
- Schae A.M., 2009, The Star-Formation History of Massive Galaxies, Ph.D. thesis, University of Edinburgh
- Schinnerer E., et al., 2008, ApJ, 689, L5
- Scott K.S., et al., 2008, MNRAS, 385, 2225
- Scott K.S., et al., 2010, MNRAS, 405, 2260
- Scott K.S., et al., 2012, MNRAS, 423, 575
- Scott S.E., et al., 2002, MNRAS, 331, 817
- Serjeant S., et al., 2008, MNRAS, 386, 1907
- Shang Z., et al., 2011, ApJS, 196, 2
- Shimizu I., Yoshida N., Okamoto T., 2012, MNRAS, submitted, arXiv:1207.3856
- Silva L., Granato G.L., Bressan A., Danese L., 1998, ApJ, 509, 103
- Siringo G., et al., 2009, A&A, 497, 945
- Smail I., Ivison R.J., Blain A.W., 1997, ApJ, 490, L5
- Smail I., Ivison R.J., Kneib J.P., Cowie L.L., Blain A.W., Barger A.J., Owen F.N., Morrison G., 1999, MNRAS, 308, 1061
- Smail I., Ivison R.J., Blain A.W., Kneib J.P., 2002, MNRAS, 331, 495
- Smail I., Chapman S.C., Blain A.W., Ivison R.J., 2004, ApJ, 616, 71
- Smolčić V., et al., 2011, ApJ, 731, L27
- Springel V., et al., 2005, Nat, 435, 629

- Swinbank A.M., Smail I., Chapman S.C., Blain A.W., Ivison R.J., Keel W.C., 2004, ApJ, 617, 64
- Swinbank A.M., Chapman S.C., Smail I., Lindner C., Borys C., Blain A.W., Ivison R.J., Lewis G.F., 2006, MNRAS, 371, 465
- Tacconi L.J., et al., 2006, ApJ, 640, 228
- Tacconi L.J., et al., 2008, ApJ, 680, 246
- Takagi T., Hanami H., Arimoto N., 2004, MNRAS, 355, 424
- Takagi T., et al., 2007, MNRAS, 381, 1154
- Targett T.A., Dunlop J.S., McLure R.J., Best P.N., Cirasuolo M., Almaini O., 2011, MNRAS, 412, 295
- Taylor M.B., 2005, In: P. Shopbell, M. Britton, & R. Ebert (ed.) *Astronomical Data Analysis Software and Systems XIV*, vol. 347 of *Astronomical Society of the Pacific Conference Series*, 29
- van Kampen E., et al., 2005, MNRAS, 359, 469
- Vega O., Clemens M.S., Bressan A., Granato G.L., Silva L., Panuzzo P., 2008, A&A, 484, 631
- Vieira J.D., et al., 2010, ApJ, 719, 763
- Wagg J., Owen F., Bertoldi F., Sawitzki M., Carilli C.L., Menten K.M., Voss H., 2009, ApJ, 699, 1843
- Wall J.V., Pope A., Scott D., 2008, MNRAS, 383, 435
- Walter F., et al., 2012, ArXiv e-prints
- Wang W.H., Cowie L.L., Barger A.J., 2004, ApJ, 613, 655
- Wang W.H., Cowie L.L., Barger A.J., Williams J.P., 2011, ApJ, 726, L18
- Wardlow J.L., et al., 2011, MNRAS, 415, 1479
- Warren S.J., et al., 2007, MNRAS, 375, 213
- Webb T.M.A., Lilly S.J., Clements D.L., Eales S., Yun M., Brodwin M., Dunne L., Gear W.K., 2003, ApJ, 597, 680
- Weiß A., et al., 2009, ApJ, 707, 1201
- Wilson G.W., et al., 2008, MNRAS, 386, 807
- Younger J.D., et al., 2008, MNRAS, 387, 707
- Yun M.S., et al., 2012, MNRAS, 420, 957

APPENDIX A: NOTES ON INDIVIDUAL SOURCES

AzLOCK1: A robust single ID (category 1). The spectroscopic mid-infrared PAH redshift from Coppin et al. (2010) was adopted.

AzLOCK2: A robust single ID (category 1).

AzLOCK3: This source has two category 1 radio IDs, but the high-resolution submillimetre imaging obtained by Younger et al. (2008) revealed that the first one (the northern, 24 μm -faint ID) is the correct ID. This is the SCUBA source LOCK850.02 (Ivison et al. 2007). The same IDs were selected.

AzLOCK4: Three candidate category 1 radio identifications. The one with the lowest p value, and confirmation at low radio frequency and 24 μm was adopted.

AzLOCK5: A robust single ID (category 1). A possible blend of weak 24 μm sources. The spectroscopic mid-infrared PAH redshift from Coppin et al. (2010) was adopted.

AzLOCK6: A robust single radio and 8 μm ID (category 1).

AzLOCK7: A possible blend of two radio/24 μm sources and an additional red $i - K$ source (category 1) at the same redshift as the first ID. This is the SCUBA source

LOCK850.04 (Ivison et al. 2007). The faintest radio ID considered by Ivison et al. (2007) is not in the catalogue used here, as it is blended with the brighter object. The spectroscopic redshift from Ivison et al. (2007) was adopted for the second ID, but the first ID is the one adopted here.

AzLOCK8: A robust single ID (category 1). This is the SCUBA source LOCK850.01 (Ivison et al. 2007). The same ID was selected. The spectroscopic mid-infrared PAH redshift from Coppin et al. (2010) was adopted.

AzLOCK9: A robust ID (category 1) with two possible weaker IDs (category 3). This is the SCUBA source LOCK850.34 (Ivison et al. 2007). We did not select their fainter radio counterpart due to its low significance and we also considered one additional 24 μm candidate.

AzLOCK10: A robust ID (category 1) with a possible weaker ID (category 3). The spectroscopic mid-infrared PAH redshift from Coppin et al. (2010) was adopted for the robust ID.

AzLOCK11: A robust ID (category 1) with a possible radio companion (category 1).

AzLOCK12: A robust ID (category 1) with a possible radio companion (category 3).

AzLOCK13: A robust single ID (category 1).

AzLOCK14: A robust single ID (category 1).

AzLOCK15: A robust single ID (category 1).

AzLOCK16: A robust single ID (category 1) with a possible 8.0 μm companion (category 3). A possible blend of weak 24 μm sources.

AzLOCK17: A robust single ID (category 1). A possible blend of weak 24 μm sources. This is the SCUBA source LOCK850.15 (Ivison et al. 2007). We selected only their second radio IDs as the remaining two are too far away from the AzTEC position.

AzLOCK18: A robust single ID (category 1).

AzLOCK19: A robust ID (category 1) with a possible red $i - K$ companion (category 3). A possible blend of weak 24 μm sources.

AzLOCK20: Two robust ID (category 1) with a possible weaker radio companion (category 3). A possible blend of weak 24 μm sources.

AzLOCK21: A single ID (category 2). A possible blend of weak 24 μm sources. This is the SCUBA source LOCK850.13 (Ivison et al. 2007). We only selected the brighter (southern) out of their two 24 μm IDs, because of low significance of the other one.

AzLOCK22: A blend of four radio sources (category 1 and 3). This is the SCUBA source LOCK850.43 (Ivison et al. 2007). We selected two out of three of their radio IDs and selected two additional IDs. The inconsistency can be explained by the fact that the radio image is severely blended at this position.

AzLOCK23: A robust single ID (category 1) with a possible weaker red $i - K$ companion (category 3).

AzLOCK24: A blend of three radio sources (category 1 and 2). This is the SCUBA source LOCK850.03 (Ivison et al. 2007). We selected both of their radio IDs and an additional faint radio ID. The spectroscopic redshift from Ivison et al. (2007) was adopted.

AzLOCK25: A robust ID (category 1) with a possible radio companion (category 3).

AzLOCK26: A robust single ID (category 1).

AzLOCK27: Three robust IDs (category 1). A possible

blend of weak 24 μm sources. This is the SCUBA source LOCK850.71 (Ivison et al. 2007). The same IDs were selected.

AzLOCK28: No IDs obtained (but only the radio selection could yield IDs due to lack of coverage at other wavelengths).

AzLOCK29: A robust single ID (category 1).

AzLOCK30: No IDs obtained.

AzLOCK31: No IDs obtained. A possible blend of weak 24 μm sources.

AzLOCK32: A robust single ID (category 1). A possible blend of weak 24 μm sources.

AzLOCK33: Two robust IDs (category 1). This is the SCUBA source LOCK850.52 (Ivison et al. 2007). The same ID was selected.

AzLOCK34: No IDs obtained.

AzLOCK35: Three IDs (category 1 and 3).

AzLOCK36: A single ID (category 2).

AzLOCK37: Three IDs (category 2 and 3).

AzLOCK38: A robust single ID (category 1).

AzLOCK39: Three IDs (category 1 and 3). A possible blend of weak 24 μm sources.

AzLOCK40: Three IDs (category 1 and 3).

AzLOCK41: A single ID (category 2). A possible blend of weak 24 μm sources.

AzLOCK42: No IDs obtained. A possible blend of weak 24 μm sources.

AzLOCK43: Three IDs (category 1 and 3). A possible blend of weak 24 μm sources. This is the SCUBA source LOCK850.79 (Ivison et al. 2007). We selected the same IDs.

AzLOCK44: A tentative single ID (category 3). A possible blend of weak 24 μm sources.

AzLOCK45: A single ID (category 2). A possible blend of weak 24 μm sources.

AzLOCK46: No IDs obtained. A possible blend of weak 24 μm sources.

AzLOCK47: A robust single ID (category 1).

AzLOCK48: No IDs obtained (but the 8.0 μm and $i - K$ methods could not be used due to lack of coverage at these wavelengths).

AzLOCK49: No IDs obtained.

AzLOCK50: A robust single ID (category 1). A possible blend of weak 24 μm sources.

AzLOCK51: Three IDs (category 1 and 3).

AzLOCK52: A robust single ID (category 1).

AzLOCK53: No IDs obtained.

AzLOCK54: Four IDs (category 1, 2 and 3).

AzLOCK55: Three IDs (category 1 and 3).

AzLOCK56: Three IDs (category 2). This is the SCUBA source LOCK850.06 (Ivison et al. 2007). The same IDs were selected.

AzLOCK57: A single ID (category 1). A possible blend of weak 24 μm sources.

AzLOCK58: Two IDs (category 1).

AzLOCK59: No IDs obtained (but the 8.0 μm and $i - K$ methods could not be used due to lack of coverage at these wavelengths).

AzLOCK60: No IDs obtained. A possible blend of weak 24 μm sources.

AzLOCK61: Two IDs (category 1 and 3). A possible blend of weak 24 μm sources.

AzLOCK62: A robust single ID (category 1). The spectro-

scopic mid-infrared PAH redshift from Coppin et al. (2010) was adopted.

AzLOCK63: Two IDs (category 2 and 3).

AzLOCK64: A robust single ID (category 1). A possible blend of weak 24 μm sources.

AzLOCK65: A tentative single ID (category 3). A possible blend of weak 24 μm sources.

AzLOCK66: A robust single ID (category 1). A possible blend of weak 24 μm sources.

AzLOCK67: Two IDs (category 1 and 3).

AzLOCK68: A robust single ID (category 1). A possible blend of weak 24 μm sources.

AzLOCK69: A robust single ID (category 1).

AzLOCK70: No IDs obtained. A possible blend of weak 24 μm sources.

AzLOCK71: A tentative single ID (category 3).

AzLOCK72: A tentative single ID (category 3). A possible blend of weak 24 μm sources.

AzLOCK73: A robust single ID (category 1).

AzLOCK74: Two IDs (category 1 and 3). A possible blend of weak 24 μm sources.

AzLOCK75: Two IDs (category 1 and 3). A possible blend of weak 24 μm sources.

AzLOCK76: A tentative single ID (category 3). A possible blend of weak 24 μm sources.

AzLOCK77: Two IDs (category 1 and 3). A possible blend of weak 24 μm sources.

AzLOCK78: A robust single ID (category 1). A possible blend of weak 24 μm sources.

AzLOCK79: A tentative single ID (category 3). A possible blend of weak 24 μm sources.

AzLOCK80: Two IDs (category 1) at similar redshifts.

AzLOCK81: Two IDs (category 3). A possible blend of weak 24 μm sources.

AzLOCK82: Five IDs (category 1 and 3).

AzLOCK83: A robust single ID (category 1). A possible blend of weak 24 μm sources.

AzLOCK84: A robust single ID (category 1). A possible blend of weak 24 μm sources.

AzLOCK85: Four IDs (category 1 and 2).

AzLOCK86: Three IDs (category 1 and 3). A possible blend of weak 24 μm sources. This is the SCUBA source LOCK850.14 (Ivison et al. 2007). We only selected the closer out of their two radio IDs, because of low significance of the other one. The spectroscopic redshift from Ivison et al. (2007) was adopted.

AzLOCK87: A robust single ID (category 1).

AzLOCK88: A robust single ID (category 1). A possible blend of weak 24 μm sources.

AzLOCK89: Two robust IDs (category 1) at low redshift (0.14). A possible blend of weak 24 μm sources. Its 1.1 mm / 1.4 GHz flux ratio is also consistent with $z \lesssim 0.5$.

AzLOCK90: No IDs obtained.

AzLOCK91: A robust single ID (category 1).

AzUDS1: No IDs obtained (but the 8.0 μm and $i - K$ methods could not be used due to lack of coverage at these wavelengths).

AzUDS2: A tentative single ID (category 3).

AzUDS3: Two robust IDs (category 1).

AzUDS4: No IDs obtained (but the $i - K$ method could

not be used due to lack of coverage at these wavelengths). A possible blend of weak $24\,\mu\text{m}$ sources.

AzUDS5: A robust single ID (category 1). This is the SCUBA source SXDF850.03 (Ivison et al. 2007). The same ID was selected. The optical counterpart and the radio ID may correspond to a possible lensing galaxy and a lensed source (see Section 4).

AzUDS6: Two IDs (category 1 and 3).

AzUDS7: Two IDs (category 1 and 3).

AzUDS8: A robust single ID (category 1).

AzUDS9: No IDs obtained. A possible blend of weak $24\,\mu\text{m}$ sources.

AzUDS10: A robust single ID (category 1). A very close star makes the photometry difficult to obtain. This is the SCUBA source SXDF850.29 (Ivison et al. 2007). The same ID was selected.

AzUDS11: A tentative single ID (category 3). A possible blend of weak $24\,\mu\text{m}$ sources.

AzUDS12: A tentative single ID (category 3).

AzUDS13: A tentative single ID (category 3).

AzUDS14: No IDs obtained.

AzUDS15: Two IDs (category 1 and 3).

AzUDS16: A single ID (category 2).

AzUDS17: Two IDs (category 1 and 3).

AzUDS18: No IDs obtained (but the $8\,\mu\text{m}$ and $i - K$ methods could not be used due to lack of coverage at these wavelengths).

AzUDS19: No IDs obtained (but the $i - K$ methods could not be used due to lack of coverage at these wavelengths).

AzUDS20: No IDs obtained.

AzUDS21: Two IDs (category 1 and 3).

AzUDS22: No IDs obtained (but the $i - K$ methods could not be used due to lack of coverage at these wavelengths).

AzUDS23: A robust single ID (category 1).

AzUDS24: No IDs obtained (but the $i - K$ methods could not be used due to lack of coverage at these wavelengths).

AzUDS25: A robust single ID (category 1).

AzUDS26: Two IDs (category 1 and 3).

AzUDS27: Three IDs (category 1 and 3). A possible blend of weak $24\,\mu\text{m}$ sources.

AzUDS28: Two IDs (category 1 and 3) at similar redshifts. A possible blend of weak $24\,\mu\text{m}$ sources.

AzUDS29: Two IDs (category 1 and 3). A possible blend of weak $24\,\mu\text{m}$ sources.

AzUDS30: Two IDs (category 1 and 3). A possible blend of weak $24\,\mu\text{m}$ sources.

AzUDS31: No IDs obtained.

AzUDS32: A robust single ID (category 1).

AzUDS33: Two IDs (category 1 and 3). This is the SCUBA source SXDF850.01 (Ivison et al. 2007). We selected an additional category 3 ID.

AzUDS34: A robust single ID (category 1).

AzUDS35: A robust single ID (category 1).

AzUDS36: A single ID (category 3).

AzUDS37: No IDs obtained.

AzUDS38: Five IDs (category 1 and 3). A possible blend of weak $24\,\mu\text{m}$ sources.

AzUDS39: No IDs obtained. A possible blend of weak $24\,\mu\text{m}$ sources.

AzUDS40: Two IDs (category 1 and 3).

AzUDS41: No IDs obtained.

AzUDS42: Five IDs (category 1 and 3). A possible blend of weak $24\,\mu\text{m}$ sources.

AzUDS43: Two robust IDs (category 1). A possible blend of weak $24\,\mu\text{m}$ sources. The first and second IDs may correspond to a possible lensing galaxy and a lensed source (see Section 4). The redshift of the second ID was used in the analysis of the redshift distribution.

AzUDS44: No IDs obtained.

AzUDS45: A robust single ID (category 1). A possible blend of weak $24\,\mu\text{m}$ sources.

AzUDS46: No IDs obtained.

AzUDS47: Five IDs (category 1). The high-resolution submillimetre imaging revealed that the second one (the most northern with $z \simeq 2.48$) is the correct ID (Hatsukade et al. 2010). This is the SCUBA source SXDF850.06 (Ivison et al. 2007). The same radio IDs were selected.

AzUDS48: A robust single ID (category 1). A possible blend of weak $24\,\mu\text{m}$ sources.

AzUDS49: A robust single ID (category 1).

AzUDS50: Two IDs (category 1 and 3). A possible blend of weak $24\,\mu\text{m}$ sources.

AzUDS51: No IDs obtained. This is the SCUBA source SXDF850.5 (Ivison et al. 2007). Their 3σ radio ID is not selected as it is too far away from the AzTEC position, which is offset from the SCUBA position by $\simeq 5$ arcsec.

AzUDS52: Four tentative IDs (category 3).

AzUDS53: A tentative ID (category 3).

AzUDS54: A robust single ID (category 1).

AzUDS55: A robust single ID (category 1). A possible blend of weak $24\,\mu\text{m}$ sources.

AzUDS56: No IDs obtained. A possible blend of weak $24\,\mu\text{m}$ sources. This is the SCUBA source SXDF850.18 (Ivison et al. 2007). Their radio ID was not selected due to its low significance.

AzUDS57: A tentative single ID (category 3).

APPENDIX B: FIGURES AND TABLES

Table B1: Reliable and tentative radio, $24\mu\text{m}$, $8.0\mu\text{m}$ and $i - K$ identifications in the Lockman Hole field. $S_{1.1\mu\text{m}}$ is deboosted millimetre flux from Austermann et al. (2010). The coordinates and the distances to the AzTEC sources are that of the 1.4 GHz ID if present and $24\mu\text{m}$ (or 0.61 GHz) otherwise. The probabilities of a counterpart to be a chance superposition, p , are bold if $p < 0.05$ and italic if $0.05 < p < 0.1$. In the last column the photometric redshifts based on optical-near-IR photometry is given. Optical spectroscopic redshift from Ivison et al. (2007) are shown with no errors and with three significant digits. Mid-IR spectroscopic redshift from Coppin et al. (2010) are shown with symmetric errors. Italicized redshift were calculated from the $1.1\text{ mm} / 1.4\text{ GHz}$ flux ratio using the average SMG SED from Michałowski et al. (2010a). Bold redshifts indicate an ID used for redshift histogram analysis. N/A is given if an object is not covered by the IRAC map (column $S_{8.0}$ and $p_{8.0}$); or by the i - or K -band map (column $i - K$ and p_{i-K}). Moreover, N/A is given for p -values if $S_{8.0} < 20\mu\text{Jy}$, or $i - K < 2$ or the object is not detected at the K -band as such objects were not taken into account for the calculations of p -values. Dots represent a non-detection at $8.0\mu\text{m}$ (column $S_{8.0}$); a nondetection at both i - and K -band (column $i - K$).

No.	$S_{1.1\mu\text{m}}$ (mJy)	RA _{ID} (deg)	DEC _{ID} (deg)	Dist ($''$)	$S_{1.4}$ (μJy)	$p_{1.4}$	$S_{0.6}$ (μJy)	$p_{0.6}$	S_{24} (μJy)	p_{24}	$S_{8.0}$ (μJy)	$p_{8.0}$	K (mag)	$i - K$ (mag)	p_{i-K}	z	
1	$6.63^{+0.85}_{-0.97}$	163.008040	57.681007	2.3	258 ± 11	0.002	596 ± 24	0.001	1642 ± 11	0.002	215 ± 19	0.009	N/A	N/A	N/A	2.50 ± 0.02	
2	$6.43^{+0.90}_{-0.89}$	163.022900	57.607548	6.5	66 ± 8	0.038	235 ± 6	0.070	31 ± 3	0.136	21.7	3.3	0.035	$2.25^{+0.13}_{-0.13}$	
3	$6.21^{+1.05}_{-0.92}$	163.237710	57.350926	2.8	67 ± 7	0.011	149 ± 16	0.004	636 ± 13	0.008	28 ± 2	0.069	23.2	<2.0	...	$2.58^{+0.12}_{-0.23}$	
...	...	163.237530	57.352273	2.6	36 ± 7	0.019	30 ± 3	0.045	24.1	<2.9	...	$3.07^{+0.11}_{-0.64}$	
4	$5.27^{+0.91}_{-0.97}$	162.686880	57.556959	7.4	150 ± 12	0.021	121 ± 17	0.045	N/A	N/A	N/A	N/A	N/A	$2.43^{+0.08}_{-0.08}$	
...	...	162.686160	57.554737	2.1	56 ± 11	0.009	99 ± 17	0.025	284 ± 13	0.013	N/A	N/A	N/A	N/A	N/A	$1.39^{+0.58}_{-0.44}$	
...	...	162.682660	57.555667	5.5	43 ± 11	0.044	N/A	N/A	N/A	N/A	N/A	3.0 ± 0.5	
5	$4.91^{+1.02}_{-0.90}$	163.515860	57.431498	0.5	138 ± 9	0.000	277 ± 19	0.000	232 ± 6	0.000	31 ± 3	0.002	23.9	<2.9	...	2.82 ± 0.02	
6	$4.75^{+0.84}_{-1.00}$	163.173650	57.597852	1.9	45 ± 8	0.009	37 ± 6	0.052	31 ± 3	0.014	$3.90^{+1.45}_{-2.60}$	
7	$4.75^{+0.89}_{-1.06}$	163.017480	57.448871	5.2	102 ± 6	0.018	189 ± 14	0.019	422 ± 16	0.023	25 ± 2	0.151	22.6	3.7	0.074	$2.40^{+0.30}_{-0.35}$	
...	...	163.015030	57.451904	6.7	49 ± 6	0.050	58 ± 15	0.056	1179 ± 13	0.016	360 ± 32	0.028	21.3	3.0	0.057	1.480	
...	...	163.016557	57.449654	1.9	28 ± 2	0.061	22.3	2.1	0.047	$2.53^{+0.10}_{-0.15}$	
8	$4.65^{+0.97}_{-0.98}$	163.005230	57.412690	2.8	110 ± 6	0.006	114 ± 16	0.010	233 ± 5	0.027	17 ± 2	N/A	23.7	<2.6	...	3.38 ± 0.02	
9	$4.09^{+0.90}_{-0.92}$	163.059220	57.557859	0.8	68 ± 8	0.001	144 ± 19	0.002	21 ± 5	0.045	25 ± 2	0.025	23.2	<1.7	N/A	3.40 ± 0.12	
...	...	163.058446	57.558749	4.3	202 ± 18	0.059	> 3.1	
...	...	163.061316	57.557803	4.0	22.5	2.5	0.082	$2.30^{+0.08}_{-0.13}$	
10	$4.15^{+0.93}_{-1.02}$	163.528620	57.552436	3.5	77 ± 9	0.014	230 ± 27	0.015	819 ± 12	0.008	126 ± 11	0.021	21.0	2.1	0.028	2.56 ± 0.03	
...	...	163.526243	57.552566	1.3	22.7	3.0	0.010	$2.38^{+0.20}_{-0.16}$	
11	$3.79^{+0.97}_{-0.89}$	162.877010	57.635730	2.0	245 ± 11	0.002	428 ± 22	0.002	1120 ± 10	0.002	N/A	N/A	N/A	N/A	N/A	1.1 ± 0.5^a	
...	...	162.877810	57.634337	4.7	35 ± 11	0.044	N/A	N/A	N/A	N/A	N/A	2.8 ± 0.5^a	
12	$3.79^{+0.88}_{-0.95}$	163.072956	57.583444	4.3	80 ± 19	0.034	39 ± 3	0.137	$3.51^{+2.49}_{-2.21}$	
...	...	163.069630	57.582199	7.0	27 ± 9	0.074	3.2 ± 0.5	
13	$4.15^{+1.02}_{-0.91}$	162.921340	57.721734	7.5	77 ± 18	0.039	171 ± 22	0.037	285 ± 4	0.089	N/A	N/A	N/A	N/A	N/A	2.1 ± 0.5^a	
14	$3.61^{+0.94}_{-0.92}$	163.084400	57.665143	0.6	35 ± 9	0.002	173 ± 8	0.036	13 ± 1	N/A	N/A	N/A	N/A	N/A	2.7 ± 0.5^a
15	$3.73^{+0.94}_{-1.00}$	163.235830	57.706780	3.8	88 ± 12	0.013	132 ± 20	0.026	441 ± 8	0.017	39 ± 3	0.065	N/A	N/A	N/A	N/A	1.9 ± 0.5^a
16	$3.65^{+0.96}_{-0.95}$	163.422140	57.537473	1.9	121 ± 8	0.003	216 ± 24	0.003	533 ± 10	0.004	39 ± 3	0.025	21.2	3.0	0.006	$1.98^{+0.12}_{-0.11}$	
...	...	163.425335	57.538825	6.0	183 ± 7	0.104	62 ± 5	0.089	20.4	2.0	N/A	$0.80^{+0.02}_{-0.08}$	
17	$3.61^{+1.02}_{-0.98}$	163.329930	57.352418	4.1	105 ± 6	0.012	263 ± 14	0.009	406 ± 6	0.022	38 ± 3	0.060	22.9	3.2	0.046	2.76 ± 0.01	
18	$3.19^{+0.97}_{-0.90}$	163.103080	57.643072	3.8	97 ± 30	0.025	N/A	N/A	N/A	2.2 ± 0.5^a	
19	$3.19^{+0.97}_{-0.92}$	162.873630	57.613839	1.1	106 ± 11	0.001	162 ± 20	0.003	194 ± 6	0.007	21.3	0.5	N/A	2.98 ± 0.02	
...	...	162.869137	57.613927	7.7	21.1	2.9	0.057	$1.47^{+0.10}_{-0.05}$	
20	$3.37^{+1.11}_{-1.08}$	163.440710	57.280218	2.6	26 ± 8	0.029	N/A	N/A	3.1 ± 0.5	
...	...	163.438430	57.277931	6.9	31 ± 8	0.077	174 ± 12	0.164	N/A	N/A	23.7	<2.6	...	$0.86^{+0.29}_{-0.29}$	
...	...	163.441228	57.278313	5.9	N/A	N/A	21.9	3.3	0.041	$1.30^{+0.07}_{-0.10}$	
21	$3.07^{+0.91}_{-0.97}$	162.880905	57.524897	4.9	210 ± 6	0.061	84 ± 7	0.051	19.4	1.7	N/A	0.57 ± 0.08	
22	$3.19^{+1.10}_{-0.99}$	163.235770	57.399629	2.0	76 ± 5	0.006	267 ± 16	0.005	976 ± 72	0.000	71 ± 6	0.024	20.8	2.2	0.013	1.31 ± 0.09	

Table B1: continued.

Table B1: continued.

No.	$S_{1.1\mu\text{m}}$ (mJy)	RA _{ID} (deg)	DEC _{ID} (deg)	Dist (")	$S_{1.4}$ (μJy)	$p_{1.4}$	$S_{0.6}$ (μJy)	$p_{0.6}$	S_{24} (μJy)	p_{24}	$S_{8.0}$ (μJy)	$p_{8.0}$	K (mag)	$i - K$ (mag)	p_{i-K}	z
50	$2.21^{+1.03}_{-1.19}$	163.020980	57.488252	4.8	136 ± 7	0.015	268 ± 17	0.011	278 ± 7	0.056	66 ± 6	0.085	20.1	2.9	0.010	$1.13^{+0.04}_{-0.08}$
51	$2.21^{+1.15}_{-1.24}$	162.650370	57.557859	4.1	79 ± 13	0.022	96 ± 15	0.026	N/A	N/A	N/A	N/A	N/A	1.5 ± 0.5^a
...	...	162.648016	57.556668	8.7	3027 ± 39	0.010	N/A	N/A	N/A	N/A	N/A	$> 2.4^a$
...	...	162.653330	57.559403	7.4	43 ± 14	0.096	98 ± 9	0.337	N/A	N/A	N/A	N/A	N/A	2.0 ± 0.5^a
52	$2.35^{+1.33}_{-1.56}$	163.031250	57.760604	5.7	86 ± 19	0.035	N/A	N/A	N/A	N/A	N/A	1.5 ± 0.5^a
53	$2.35^{+1.20}_{-1.49}$	N/A	N/A	N/A	$> 2.4^a$
54	$2.13^{+1.10}_{-1.21}$	163.466554	57.447410	3.7	291 ± 17	0.038	N/A	N/A	N/A	$> 2.3^a$
...	...	163.466970	57.446462	4.4	26 ± 8	0.077	19 ± 7	0.687	24 ± 2	0.210	N/A	N/A	N/A	2.5 ± 0.5^a
...	...	163.466080	57.450271	12.3	92 ± 8	0.095	199 ± 17	0.084	349 ± 17	0.184	N/A	N/A	N/A	1.4 ± 0.5^a
...	...	163.458444	57.447070	12.5	158 ± 2	0.390	851 ± 75	0.042	N/A	N/A	N/A	$> 2.3^a$
55	$2.35^{+1.30}_{-1.96}$	162.976211	57.175804	3.9	240 ± 12	0.040	N/A	N/A	N/A	N/A	N/A	$> 2.4^a$
...	...	162.974050	57.177404	4.5	42 ± 10	0.057	N/A	N/A	N/A	N/A	N/A	2.1 ± 0.5^a
...	...	162.975700	57.177560	5.2	69 ± 17	0.085	N/A	N/A	N/A	N/A	N/A	2.2 ± 0.5^a
56	$2.13^{+1.12}_{-1.26}$	163.014780	57.421302	6.5	33 ± 7	0.106	80 ± 16	0.053	352 ± 8	0.068	35 ± 3	0.223	20.3	1.7	N/A	1.04^{+0.06}_{-0.04}
...	...	163.017130	57.423446	2.7	89 ± 14	0.091	25 ± 2	0.059	23.3	< 1.9	N/A	$4.60^{+0.03}_{-0.12}$
...	...	163.021900	57.422944	11.4	38 ± 6	0.180	116 ± 16	0.127	646 ± 11	0.088	556 ± 49	0.062	18.8	1.2	N/A	$0.60^{+0.12}_{-0.05}$
57	$2.05^{+1.18}_{-1.20}$	163.209248	57.435705	9.5	455 ± 9	0.108	3533 ± 311	0.007	N/A	N/A	N/A	$> 2.3^a$
58	$2.05^{+1.07}_{-1.19}$	163.181646	57.677593	3.9	770 ± 21	0.012	5531 ± 487	0.001	N/A	N/A	N/A	$> 2.3^a$
...	...	163.182610	57.678603	0.5	74 ± 22	0.001	N/A	N/A	N/A	2.0 ± 0.5^a
59	$2.05^{+1.08}_{-1.20}$	N/A	N/A	N/A	> 2.3
60	$2.05^{+1.11}_{-1.22}$	> 2.3
61	$2.05^{+1.21}_{-1.27}$	163.239680	57.379146	4.5	29 ± 4	0.075	74 ± 19	0.074	272 ± 8	0.054	18 ± 2	N/A	22.0	4.1	0.038	$1.58^{+0.24}_{-0.21}$
...	...	163.234813	57.381071	7.5	20 ± 2	N/A	21.8	3.5	0.077	$1.40^{+0.07}_{-0.08}$
62	$1.95^{+1.05}_{-1.16}$	163.049240	57.586139	1.8	65 ± 7	0.007	167 ± 20	0.008	272 ± 7	0.011	32 ± 3	0.025	23.0	> 3.4	0.031	2.48 ± 0.03
63	$2.05^{+1.19}_{-1.40}$	163.525460	57.343559	5.3	37 ± 9	0.077	190 ± 31	0.090	N/A	N/A	22.1	1.6	N/A	$1.30^{+0.10}_{-0.13}$
...	...	163.518080	57.343389	15.8	73 ± 9	0.171	89 ± 18	0.258	1722 ± 10	0.056	N/A	N/A	19.6	0.4	N/A	$0.16^{+0.04}_{-0.16}$
64	$1.95^{+1.07}_{-1.18}$	163.294160	57.576504	2.8	188 ± 7	0.004	347 ± 22	0.004	457 ± 9	0.015	53 ± 5	0.044	21.8	1.4	N/A	$3.06^{+0.02}_{-0.13}$
65	$1.97^{+1.08}_{-1.22}$	163.241560	57.659149	4.2	32 ± 11	0.062	142 ± 6	0.184	29 ± 3	0.183	N/A	N/A	N/A	2.2 ± 0.5^a
66	$1.95^{+1.08}_{-1.24}$	163.463590	57.514934	4.7	67 ± 8	0.034	107 ± 20	0.040	230 ± 15	0.074	23 ± 2	0.191	22.5	2.4	0.208	$1.90^{+0.15}_{-0.18}$
67	$1.89^{+1.14}_{-1.19}$	162.683620	57.488883	10.3	108 ± 17	0.131	888 ± 13	0.067	259 ± 23	0.109	N/A	N/A	N/A	$0.60^{+0.05}_{-0.15}$
...	...	162.687912	57.490231	2.0	28 ± 2	0.048	N/A	N/A	N/A	> 2.2	
68	$1.95^{+1.12}_{-1.31}$	163.356740	57.380114	2.3	75 ± 6	0.009	138 ± 15	0.003	100 ± 6	0.072	43 ± 4	0.043	21.3	3.0	0.008	$1.41^{+0.06}_{-0.09}$
69	$1.89^{+1.20}_{-1.31}$	162.748590	57.545517	1.9	42 ± 11	0.014	60 ± 20	0.014	315 ± 7	0.011	N/A	N/A	N/A	N/A	N/A	1.9 ± 0.5^a
70	$1.89^{+1.04}_{-1.20}$	> 2.2
71	$1.89^{+1.14}_{-1.25}$	163.532170	57.500368	6.6	28 ± 8	0.135	81 ± 24	0.088	216 ± 8	0.131	40 ± 4	0.189	24.4	< 3.2	...	$3.15^{+0.10}_{-1.40}$
72	$1.89^{+1.10}_{-1.24}$	162.883580	57.672004	6.2	44 ± 12	0.080	33 ± 6	0.740	N/A	N/A	N/A	N/A	N/A	1.9 ± 0.5^a
73	$1.89^{+1.07}_{-1.24}$	162.987140	57.683242	2.4	74 ± 11	0.011	117 ± 22	0.023	688 ± 25	0.008	N/A	N/A	N/A	N/A	N/A	1.5 ± 0.5^a
74	$1.89^{+1.18}_{-1.45}$	163.193130	57.296706	5.6	85 ± 6	0.037	148 ± 12	0.038	681 ± 28	0.022	47 ± 4	0.156	N/A	N/A	N/A	1.4 ± 0.5^a
...	...	163.187586	57.296442	12.0	621 ± 55	0.060	14.7	N/A	N/A	$0.08^{+0.02}_{-0.03}$
75	$1.89^{+1.17}_{-1.45}$	163.288440	57.283102	4.1	117 ± 7	0.015	290 ± 17	0.017	415 ± 8	0.026	N/A	N/A	N/A	N/A	N/A	1.2 ± 0.5^a
...	...	163.286010	57.282503	9.3	107 ± 7	0.062	N/A	N/A	N/A	N/A	N/A	1.2 ± 0.5^a
76	$1.87^{+1.00}_{-1.23}$	163.121253	57.551547	9.1	123 ± 26	0.383	24 ± 2	0.378	20.6	2.7	0.054	$1.12^{+0.05}_{-0.07}$
77	$1.89^{+1.05}_{-1.30}$	162.951740	57.688409	4.8	102 ± 13	0.022	190 ± 27	0.031	386 ± 13	0.040	N/A	N/A	N/A	N/A	N/A	1.2 ± 0.5^a
...	...	162.948700	57.691634	8.2	58 ± 13	0.091	59 ± 4	0.579	N/A	N/A	N/A	N/A	N/A	1.6 ± 0.5^a
78	$1.89^{+1.06}_{-1.33}$	163.458285	57.564010	3.1	406 ± 9	0.016	24 ± 2	0.054	22.6	1.5	N/A	2.21^{+0.14}_{-0.34}
79	$1.89^{+1.15}_{-1.47}$	163.130527	57.264555	15.9	90 ± 6	0.757	1183 ± 104	0.053	N/A	N/A	N/A	$> 2.2^a$
80	$1.89^{+1.14}_{-1.54}$	163.575400	57.579668	3.8	61 ± 12	0.028	446 ± 6	0.018	46 ± 4	0.080	21.6	3.5	0.018	$1.77^{+0.18}_{-0.20}$
...	...	163.577890	57.578058	6.7	94 ± 11	0.043	109 ± 29	0.058	286 ± 8	0.123	33 ± 3	0.299	22.0	2.0	0.330	$1.52^{+0.08}_{-0.10}$
81	$1.89^{+1.05}_{-1.41}$	163.342850	57.386243	5.1	31 ± 6	0.091	2.2 ± 0.5
...	...	163.343604	57.384038	8.5	197 ± 4	0.227	44 ± 4	0.294	21.2	3.3	0.051	$2.25^{+0.07}_{-0.05}$

Table B1: continued.

No.	$S_{1.1\mu\text{m}}$ (mJy)	RA _{ID} (deg)	DEC _{ID} (deg)	Dist ('')	$S_{1.4}$ (μJy)	$p_{1.4}$	$S_{0.6}$ (μJy)	$p_{0.6}$	S_{24} (μJy)	p_{24}	$S_{8.0}$ (μJy)	$p_{8.0}$	K (mag)	$i - K$ (mag)	p_{i-K}	z
82	$1.79^{+1.03}_{-1.29}$	162.903830	57.631042	6.4	363 ± 12	0.008	959 ± 22	0.007	862 ± 41	0.019	N/A	N/A	N/A	0.6 ± 0.5^a
...	...	162.905480	57.631763	4.9	93 ± 12	0.026	108 ± 9	0.030	N/A	N/A	N/A	1.3 ± 0.5^a
...	...	162.906190	57.632486	4.7	115 ± 22	0.041	N/A	N/A	N/A	1.5 ± 0.5^a
...	...	162.902240	57.630337	9.4	70 ± 11	0.094	72 ± 21	0.213	N/A	N/A	N/A	1.5 ± 0.5^a
...	...	162.906694	57.633462	5.0	305 ± 17	0.083	38 ± 3	0.199	N/A	N/A	N/A	$> 2.2^a$
83	$1.89^{+0.91}_{-1.87}$	162.840330	57.709211	4.2	165 ± 18	0.011	283 ± 24	0.010	401 ± 9	0.033	N/A	N/A	N/A	N/A	N/A	1.0 \pm 0.5^a
84	$1.89^{+0.71}_{-1.98}$	162.920420	57.188941	1.4	63 ± 9	0.005	82 ± 17	0.018	119 ± 5	0.033	N/A	N/A	N/A	N/A	N/A	1.6 ± 0.5^a
85	$1.79^{+1.00}_{-1.43}$	163.431700	57.429228	2.3	46 ± 7	0.017	89 ± 18	0.010	41 ± 5	0.059	27 ± 2	0.078	24.0	< 3.0	...	$2.57^{+0.13}_{-0.22}$
...	...	163.431593	57.428092	1.6	89 ± 18	0.010	112 ± 13	0.093	1.7 ± 0.5
...	...	163.430310	57.425037	14.2	199 ± 6	0.061	393 ± 15	0.056	1081 ± 21	0.081	70 ± 6	0.370	19.1	1.5	N/A	$1.03^{+0.04}_{-0.06}$
...	...	163.434000	57.425647	11.7	102 ± 7	0.090	153 ± 15	0.125	865 ± 16	0.078	64 ± 6	0.338	22.1	2.6	0.366	$1.76^{+0.16}_{-0.29}$
86	$1.79^{+0.97}_{-1.57}$	163.128230	57.369305	2.0	61 ± 6	0.010	89 ± 14	0.020	193 ± 7	0.016	52 ± 5	0.013	21.9	2.0	N/A	2.611
...	...	163.121126	57.368877	12.0	21.2	3.1	0.091	$1.12^{+0.08}_{-0.05}$
...	...	163.130216	57.370344	6.6	22.1	3.9	0.088	$1.37^{+0.10}_{-0.22}$
87	$1.79^{+0.95}_{-1.53}$	162.655010	57.541291	2.1	52 ± 12	0.013	136 ± 16	0.018	337 ± 10	0.010	N/A	N/A	N/A	N/A	N/A	1.7 ± 0.5^a
88	$1.79^{+0.81}_{-1.84}$	163.492020	57.667372	6.9	84 ± 11	0.052	260 ± 35	0.028	335 ± 8	0.121	73 ± 6	0.189	N/A	N/A	N/A	1.3 ± 0.5^a
89	$1.73^{+0.93}_{-1.51}$	162.656590	57.479112	3.2	421 ± 10	0.002	710 ± 17	0.003	968 ± 11	0.006	373 ± 33	0.008	N/A	N/A	N/A	$0.14^{+0.14}_{-0.11}$
...	...	162.655038	57.480839	6.1	304 ± 27	0.037	N/A	N/A	N/A	> 2.2
90	$1.65^{+0.90}_{-1.57}$	> 2.1
91	$1.68^{+0.63}_{-1.81}$	163.196510	57.188842	2.6	75 ± 14	0.026	1.8 ± 0.5

^aThe optical photometric redshift could not been measured because this object is outside of the optical map (or close to a bright star)

Table B2: Reliable and tentative radio, 24 μm , 8.0 μm and $i - K$ identifications in the UDS field. Columns are described in Table B1

No.	$S_{1.1\mu\text{m}}$ (mJy)	RA _{ID} (deg)	DEC _{ID} (deg)	Dist (")	$S_{1.4}$ (μJy)	$p_{1.4}$	S_{24} (μJy)	p_{24}	$S_{8.0}$ (μJy)	$p_{8.0}$	K (mag)	$i - K$ (mag)	p_{i-K}	z
1	$5.29^{+1.40}_{-1.68}$	N/A	N/A	N/A	N/A	N/A	$> 2.9^a$
2	$3.99^{+1.10}_{-1.34}$	34.442284	-4.796439	5.7	77 ± 7	0.199	21 ± 2	0.162	22.8	> 3.6	0.084	$2.53^{+0.47}_{-0.28}$
3	$3.75^{+1.22}_{-1.18}$	34.479333	-4.789667	1.5	113 ± 20	0.002	776 ± 11	0.002	78 ± 7	0.014	21.6	3.8	0.005	$1.81^{+0.04}_{-0.06}$
...	...	34.479412	-4.789859	1.4	21.6	4.6	0.003	$3.13^{+0.07}_{-0.10}$
4	$4.39^{+1.67}_{-1.58}$	N/A	N/A	N/A	$> 2.7^a$
5	$3.57^{+1.19}_{-1.21}$	34.425542	-4.941028	1.0	89 ± 17	0.002	40 ± 4	0.022	19.3	1.3	N/A	$0.45^{+0.05}_{-0.05}$
6	$3.99^{+1.27}_{-1.57}$	34.677833	-4.992167	4.3	105 ± 16	0.014	924 ± 37	0.009	77 ± 7	0.047	21.2	3.6	0.011	$2.29^{+0.09}_{-0.07}$
...	...	34.677021	-4.991021	5.2	73 ± 6	0.075	19.8	1.4	N/A	$0.45^{+0.08}_{-0.05}$
7	$3.99^{+1.57}_{-1.67}$	34.233034	-4.759176	2.1	174 ± 10	0.023	23 ± 2	0.054	21.3	2.1	0.019	$1.33^{+0.09}_{-0.11}$
...	...	34.232956	-4.758326	2.8	11 ± 1	N/A	21.8	2.1	0.054	$0.73^{+0.24}_{-0.08}$
8	$3.99^{+1.59}_{-1.82}$	34.424875	-4.525111	5.8	153 ± 24	0.016	329 ± 12	0.053	N/A	N/A	N/A	N/A	N/A	1.5 ± 0.5^a
9	$3.75^{+1.90}_{-2.37}$	> 2.5
10	$3.07^{+1.21}_{-1.31}$	34.568708	-4.919111	7.1	240 ± 15	0.013	1047 ± 33	0.021	72 ± 6	0.124	20.2	0.6	N/A	$0.39^{+0.06}_{-0.19}$
11	$3.29^{+1.52}_{-1.71}$	34.283750	-4.935194	8.7	59 ± 15	0.077	198 ± 6	0.185	33 ± 3	0.279	$5.53^{+0.17}_{-3.93}$
12	$3.29^{+1.66}_{-1.94}$	34.281514	-4.713486	10.9	12 ± 1	N/A	20.9	2.5	0.095	$1.10^{+0.07}_{-0.08}$
13	$2.83^{+1.19}_{-1.36}$	34.618958	-4.912472	9.3	55 ± 19	0.084	N/A	N/A	N/A	2.0 ± 0.5^a
14	$2.93^{+1.54}_{-1.52}$	> 2.2
15	$2.93^{+1.32}_{-1.53}$	34.478542	-4.739333	4.2	61 ± 18	0.028	464 ± 10	0.032	41 ± 4	0.087	20.8	2.0	0.030	$0.99^{+0.08}_{-0.07}$
...	...	34.477875	-4.736583	6.0	34 ± 13	0.078	3 ± 1	N/A	24.8	> 1.6	N/A	$1.37^{+0.30}_{-0.35}$
16	$2.93^{+1.48}_{-1.59}$	34.317708	-4.966000	10.8	125 ± 26	0.054	843 ± 10	0.056	425 ± 37	0.063	19.0	1.1	N/A	$0.11^{+0.04}_{-0.06}$
17	$3.07^{+1.61}_{-1.99}$	34.299750	-4.721611	5.4	59 ± 20	0.045	137 ± 16	0.218	24.3	> 2.1	0.807	$1.25^{+0.17}_{-0.20}$
...	...	34.297058	-4.719346	7.4	15 ± 1	N/A	22.0	4.1	0.086	$2.28^{+0.10}_{-0.16}$
18	$3.11^{+1.52}_{-2.65}$	N/A	N/A	N/A	N/A	N/A	$> 2.3^a$
19	$3.28^{+0.94}_{-3.27}$	N/A	N/A	N/A	$> 2.3^a$
20	$2.93^{+1.34}_{-2.61}$	> 2.2
21	$2.63^{+1.61}_{-1.77}$	34.540635	-5.077821	4.8	17 ± 2	N/A	20.6	2.6	0.020	$1.04^{+0.08}_{-0.04}$
...	...	34.543259	-5.078739	8.5	58 ± 2	0.576	20 ± 2	N/A	21.5	3.1	0.068	$1.33^{+0.07}_{-0.06}$
22	$2.47^{+1.23}_{-1.54}$	N/A	N/A	N/A	$> 2.1^a$
23	$2.47^{+1.26}_{-1.57}$	34.585958	-4.958528	9.9	126 ± 34	0.050	195 ± 5	0.249	19 ± 2	N/A	20.6	1.2	N/A	$0.64^{+0.08}_{-0.14}$
24	$2.78^{+0.87}_{-2.81}$	N/A	N/A	N/A	$> 2.2^a$
25	$2.83^{+0.70}_{-2.89}$	34.605208	-5.156611	0.3	53 ± 18	0.000	2.1 ± 0.5
26	$2.27^{+1.30}_{-1.48}$	34.634092	-4.941660	3.0	266 ± 13	0.042	13 ± 1	N/A	23.0	> 3.4	0.064	$3.30^{+0.30}_{-0.35}$
...	...	34.633677	-4.941219	5.8	17 ± 1	N/A	21.2	3.0	0.055	$0.98^{+0.07}_{-0.13}$
27	$2.66^{+0.51}_{-2.78}$	34.662821	-4.580741	3.7	249 ± 9	0.029	18 ± 2	N/A	N/A	N/A	N/A	$> 2.2^a$
...	...	34.659875	-4.581861	8.6	62 ± 23	0.084	396 ± 17	0.114	N/A	N/A	N/A	1.9 ± 0.5^a
...	...	34.659872	-4.583055	10.9	20 ± 4	0.850	496 ± 44	0.059	N/A	N/A	N/A	$> 2.2^a$
28	$2.27^{+1.21}_{-1.73}$	34.511917	-5.008611	14.1	529 ± 14	0.019	1172 ± 50	0.074	97 ± 9	0.301	21.0	2.9	0.167	$1.03^{+0.07}_{-0.08}$
...	...	34.510316	-5.004469	2.5	8 ± 1	N/A	22.0	2.5	0.065	$1.13^{+0.09}_{-0.11}$

Table B2: continued.

No.	$S_{1.1\mu\text{m}}$ (mJy)	RA _{ID} (deg)	DEC _{ID} (deg)	Dist (")	$S_{1.4}$ (μJy)	$p_{1.4}$	S_{24} (μJy)	p_{24}	$S_{8.0}$ (μJy)	$p_{8.0}$	K (mag)	$i - K$ (mag)	p_{i-K}	z
29	$2.13^{+1.27}_{-1.52}$	34.486417	-4.877444	6.4	88 ± 17	0.040	435 ± 7	0.056	48 ± 4	0.172	21.6	4.0	0.047	$3.07^{+0.08}_{-0.09}$
...	...	34.484820	-4.880592	7.6	11 ± 1	N/A	21.5	3.3	0.056	$0.97^{+0.10}_{-0.07}$
30	$2.27^{+1.14}_{-2.03}$	34.423402	-5.038808	1.8	100 ± 4	0.065	16 ± 1	N/A	21.8	1.2	N/A	$2.19^{+0.08}_{-0.14}$
...	...	34.422787	-5.040026	6.0	18 ± 2	N/A	20.2	2.2	0.035	$0.82^{+0.08}_{-0.12}$
31	$2.85^{+0.01}_{-3.01}$	> 2.2
32	$2.13^{+1.05}_{-2.01}$	34.529958	-4.737167	3.7	68 ± 19	0.023	$5.69^{+0.01}_{-5.14}$
33	$2.03^{+1.13}_{-1.92}$	34.377625	-4.993472	2.5	63 ± 15	0.013	21 ± 2	0.088	23.1	2.7	0.105	$3.19^{+0.16}_{-0.11}$
...	...	34.373214	-4.993681	16.8	81 ± 13	0.175	539 ± 14	0.219	56 ± 5	0.524	20.7	3.1	0.089	$1.02^{+0.08}_{-0.07}$
34	$2.03^{+1.11}_{-1.73}$	34.530583	-4.827694	5.8	67 ± 20	0.047	407 ± 9	0.063	33 ± 3	0.228	22.1	2.8	0.151	$2.32^{+0.11}_{-0.12}$
35	$2.19^{+0.57}_{-2.32}$	34.305542	-4.982639	4.4	54 ± 16	0.038	17 ± 2	N/A	23.5	0.9	N/A	$3.40^{+0.13}_{-0.07}$
36	$2.17^{+0.61}_{-2.29}$	34.297946	-4.965358	4.5	6 ± 1	N/A	21.8	2.9	0.073	$1.00^{+0.07}_{-0.08}$
37	$1.99^{+1.02}_{-1.88}$	> 1.9
38	$2.64^{+0.01}_{-2.81}$	34.375103	-5.164719	2.1	220 ± 13	0.020	25 ± 2	0.057	20.5	2.6	0.004	$1.11^{+0.04}_{-0.09}$
...	...	34.374508	-5.163503	4.0	16 ± 1	N/A	22.1	3.3	0.036	$2.36^{+0.17}_{-0.06}$
...	...	34.378489	-5.162173	13.3	24 ± 2	0.474	20.1	2.7	0.058	$1.05^{+0.07}_{-0.03}$
...	...	34.373557	-5.163234	7.4	29 ± 3	0.277	20.5	3.1	0.018	$1.04^{+0.08}_{-0.04}$
...	...	34.373963	-5.163446	5.8	29 ± 4	0.542	21.8	2.7	0.097	$1.04^{+0.08}_{-0.12}$
39	$2.42^{+0.01}_{-2.66}$	N/A	N/A	N/A	N/A	N/A	$> 2.1^a$
40	$1.83^{+1.01}_{-1.81}$	34.611500	-4.825250	2.3	56 ± 18	0.014	1.6 ± 0.5
...	...	34.609815	-4.828521	10.9	100 ± 8	0.560	29 ± 3	0.498	19.8	2.0	0.063	$0.79^{+0.08}_{-0.09}$
41	$1.94^{+0.74}_{-2.03}$	> 1.9
42	$1.83^{+1.00}_{-1.82}$	34.406167	-4.801278	3.4	142 ± 16	0.009	51 ± 13	0.369	16 ± 1	N/A	23.0	2.0	N/A	$3.19^{+0.06}_{-0.09}$
...	...	34.405351	-4.801697	3.7	268 ± 19	0.045	> 1.8
...	...	34.404859	-4.801858	4.7	31 ± 3	0.178	20.7	2.3	0.044	$0.82^{+0.13}_{-0.10}$
...	...	34.400962	-4.801975	16.7	126 ± 28	0.120	523 ± 9	0.236	172 ± 15	0.277	19.2	2.1	0.065	$0.39^{+0.09}_{-0.06}$
...	...	34.405269	-4.801233	2.1	22.4	2.0	0.077	$0.93^{+0.04}_{-0.03}$
43	$2.65^{+0.01}_{-2.79}$	34.640708	-5.171083	3.1	108 ± 21	0.009	903 ± 26	0.002	188 ± 17	0.017	19.1	1.1	N/A	$0.15^{+0.05}_{-0.07}$
...	...	34.640676	-5.172059	2.2	38 ± 3	0.041	22.3	3.4	0.018	$2.43^{+0.12}_{-0.16}$
44	$1.83^{+0.98}_{-1.80}$	> 1.8
45	$1.83^{+0.94}_{-1.83}$	34.578625	-4.841361	4.5	65 ± 16	0.035	156 ± 11	0.103	24 ± 2	0.199	23.0	>3.4	0.131	$2.27^{+0.38}_{-0.25}$
...	...	34.576573	-4.843538	6.3	30 ± 12	0.124	106 ± 20	0.295	24 ± 2	0.318	21.3	3.6	0.040	$1.36^{+0.06}_{-0.09}$
46	$2.28^{+0.01}_{-2.55}$	> 2.0
47	$1.99^{+0.34}_{-2.24}$	34.374708	-5.056222	2.1	57 ± 18	0.011	1477 ± 125	0.002	27 ± 2	0.066	21.8	1.8	N/A	$2.10^{+0.10}_{-0.13}$
...	...	34.374000	-5.055139	6.1	88 ± 14	0.037	42 ± 4	0.181	22.2	3.5	0.083	$2.48^{+0.10}_{-0.23}$
...	...	34.375875	-5.057028	5.1	65 ± 19	0.039	76 ± 7	0.094	19.8	2.2	0.017	$0.47^{+0.08}_{-0.04}$
...	...	34.372978	-5.056321	5.6	21 ± 2	0.278	20.5	2.2	0.044	$0.71^{+0.06}_{-0.09}$
...	...	34.375091	-5.057346	3.1	56 ± 5	0.053	19.3	2.3	0.004	$0.83^{+0.07}_{-0.11}{}^a$
48	$2.30^{+0.01}_{-2.52}$	34.539312	-4.468155	2.9	N/A	N/A	205 ± 6	0.038	N/A	N/A	N/A	N/A	N/A	$2.0 \pm 1.0{}^a$
49	$2.03^{+0.24}_{-2.30}$	34.427583	-4.650025	0.7	43 ± 4	0.033	5 ± 1	N/A	N/A	N/A	N/A	$> 1.9{}^a$
50	$2.26^{+0.01}_{-2.50}$	34.349250	-4.587278	6.7	372 ± 24	0.008	975 ± 8	0.022	N/A	N/A	N/A	N/A	N/A	$0.7 \pm 0.5{}^a$

Table B2: continued.

No.	$S_{1.1\mu\text{m}}$ (mJy)	RA _{ID} (deg)	DEC _{ID} (deg)	Dist ('')	$S_{1.4}$ (μJy)	$p_{1.4}$	S_{24} (μJy)	p_{24}	$S_{8.0}$ (μJy)	$p_{8.0}$	K (mag)	$i - K$ (mag)	p_{i-K}	z
...	...	34.350000	-4.591806	9.8	88 ± 30	0.068	N/A	N/A	N/A	N/A	N/A	1.5 ± 0.5^a
51	$1.92^{+0.33}_{-2.17}$	> 1.9
52	$1.75^{+0.77}_{-1.80}$	34.417528	-4.916742	4.0	12 ± 1	N/A	21.4	2.5	0.076	$1.43^{+0.07}_{-0.08}$
...	...	34.419344	-4.916439	3.0	32 ± 3	0.089	18.5	1.3	N/A	$0.56^{+0.06}_{-0.03}$
...	...	34.419426	-4.914115	10.4	47 ± 4	0.357	21.1	4.0	0.067	1.36^{+0.06}_{-0.11}
...	...	34.420239	-4.912388	17.4	97 ± 31	0.155	927 ± 39	0.112	671 ± 59	0.098	18.9	0.7	N/A	$0.15^{+0.05}_{-0.12}$
53	$2.19^{+0.01}_{-2.44}$	34.703512	-5.000932	12.0	14 ± 1	N/A	21.4	3.5	0.099	1.46^{+0.06}_{-0.09}
54	$1.75^{+0.67}_{-1.83}$	34.638576	-4.968898	2.2	103 ± 5	0.029	15 ± 1	N/A	24.8	>1.6	N/A	4.07^{+1.63}_{-3.17}
55	$2.38^{+0.01}_{-2.53}$	34.762124	-4.915183	0.8	297 ± 5	0.002	51 ± 4	0.006	20.9	4.0	0.001	1.47^{+0.05}_{-0.05}
56	$1.67^{+0.61}_{-1.81}$	> 1.8
57	$2.24^{+0.01}_{-2.43}$	34.363693	-5.111945	2.7	23 ± 2	0.088	> 2.0

^aThe optical photometric redshift could not been measured because this object is outside of the optical map (or close to a bright star)

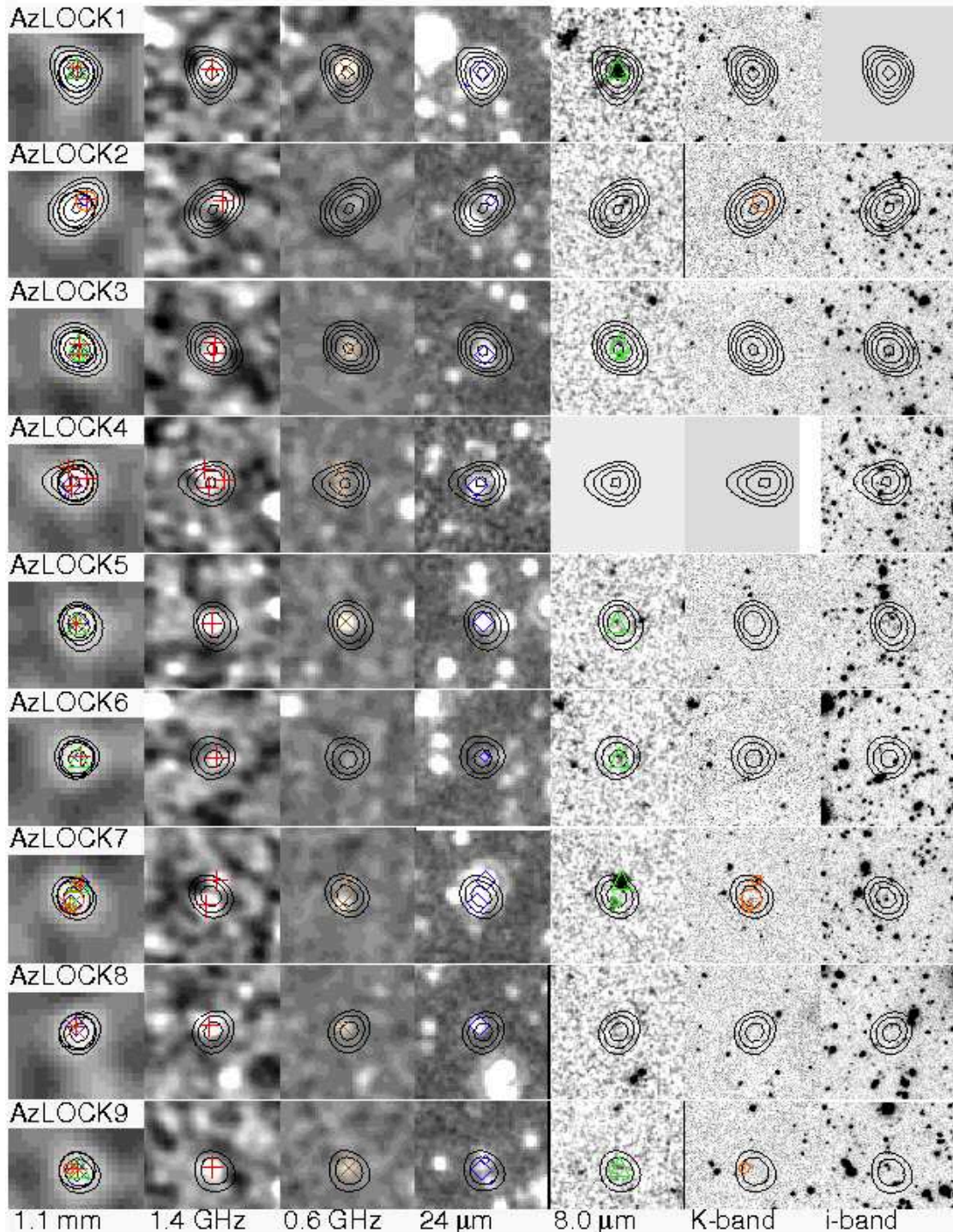
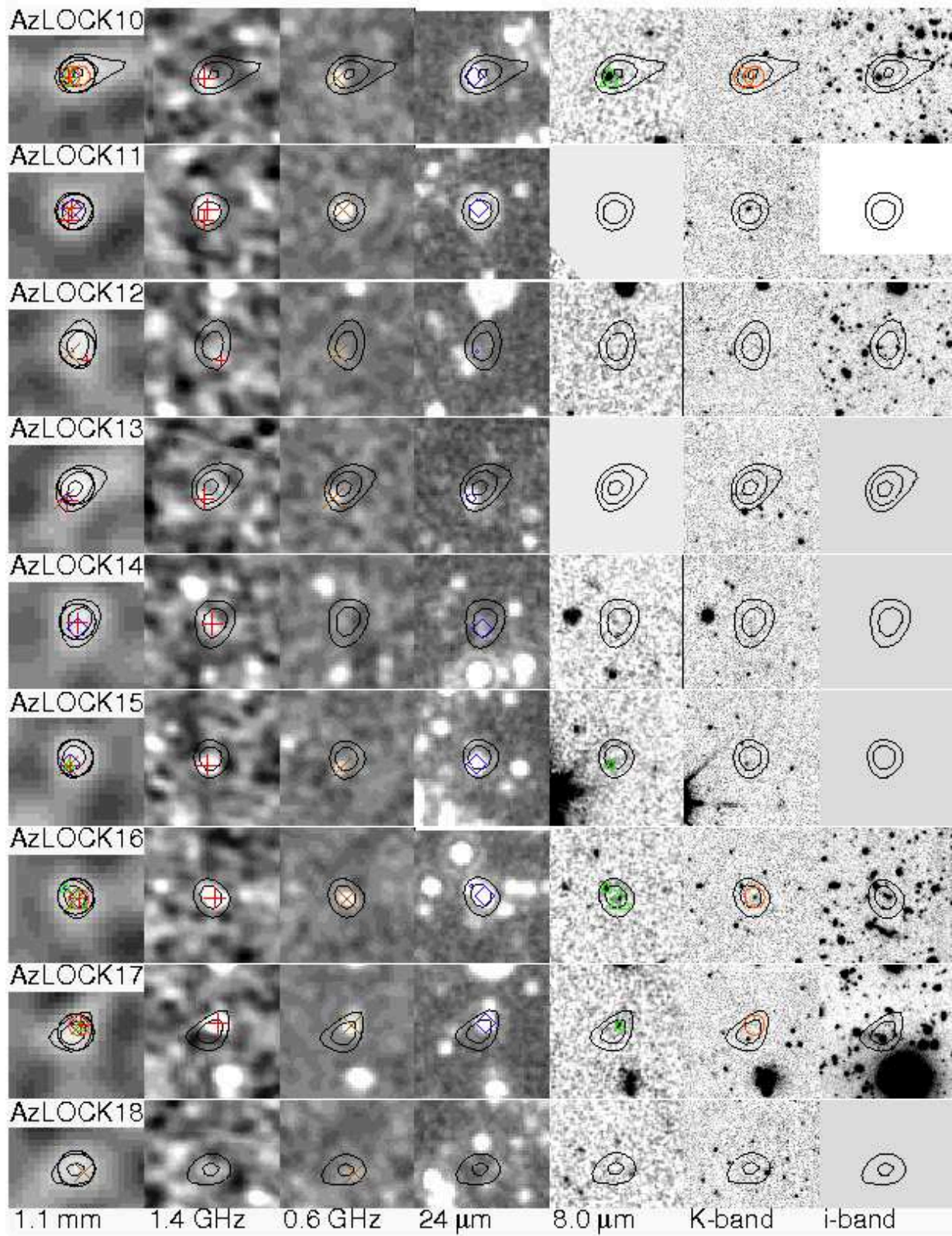
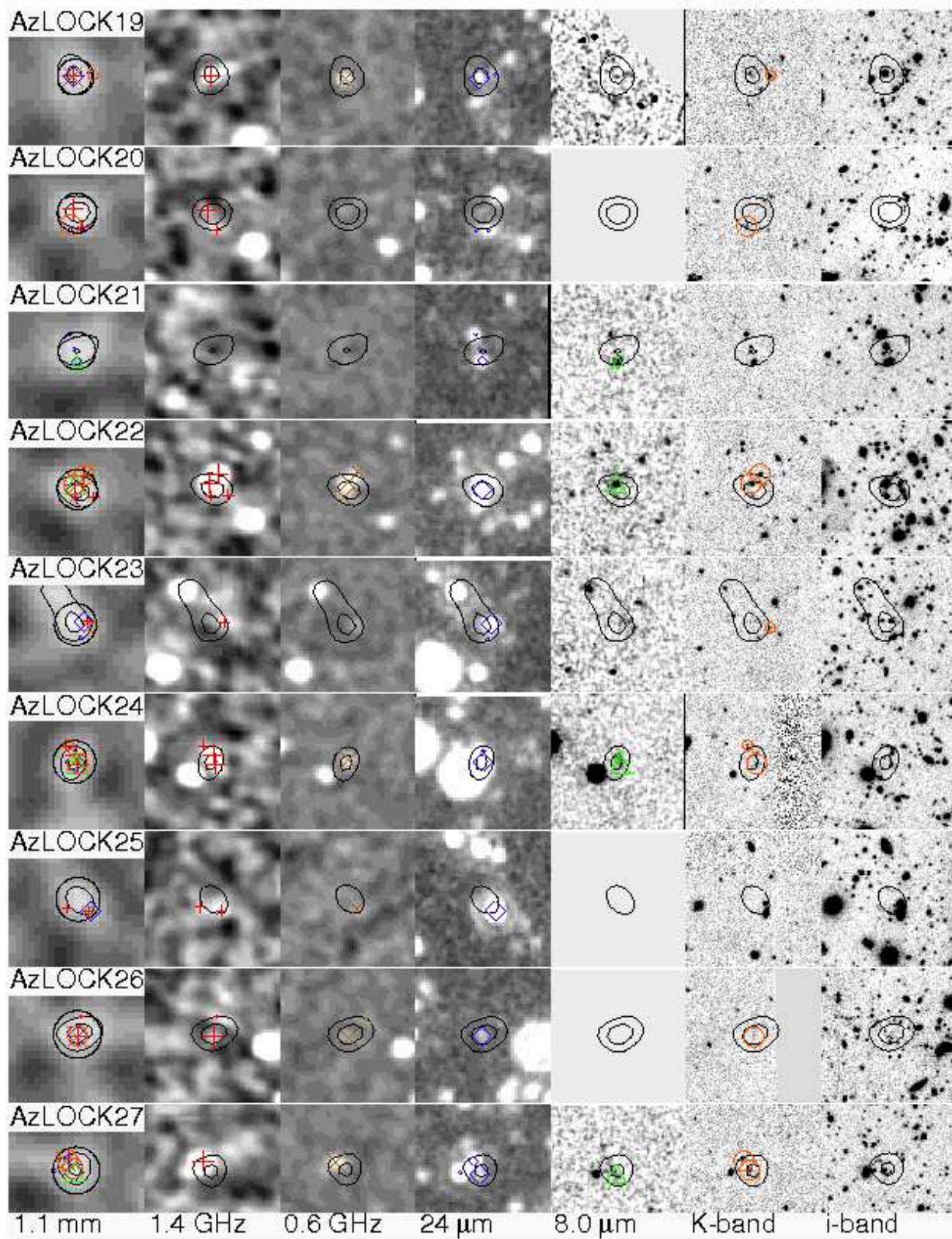
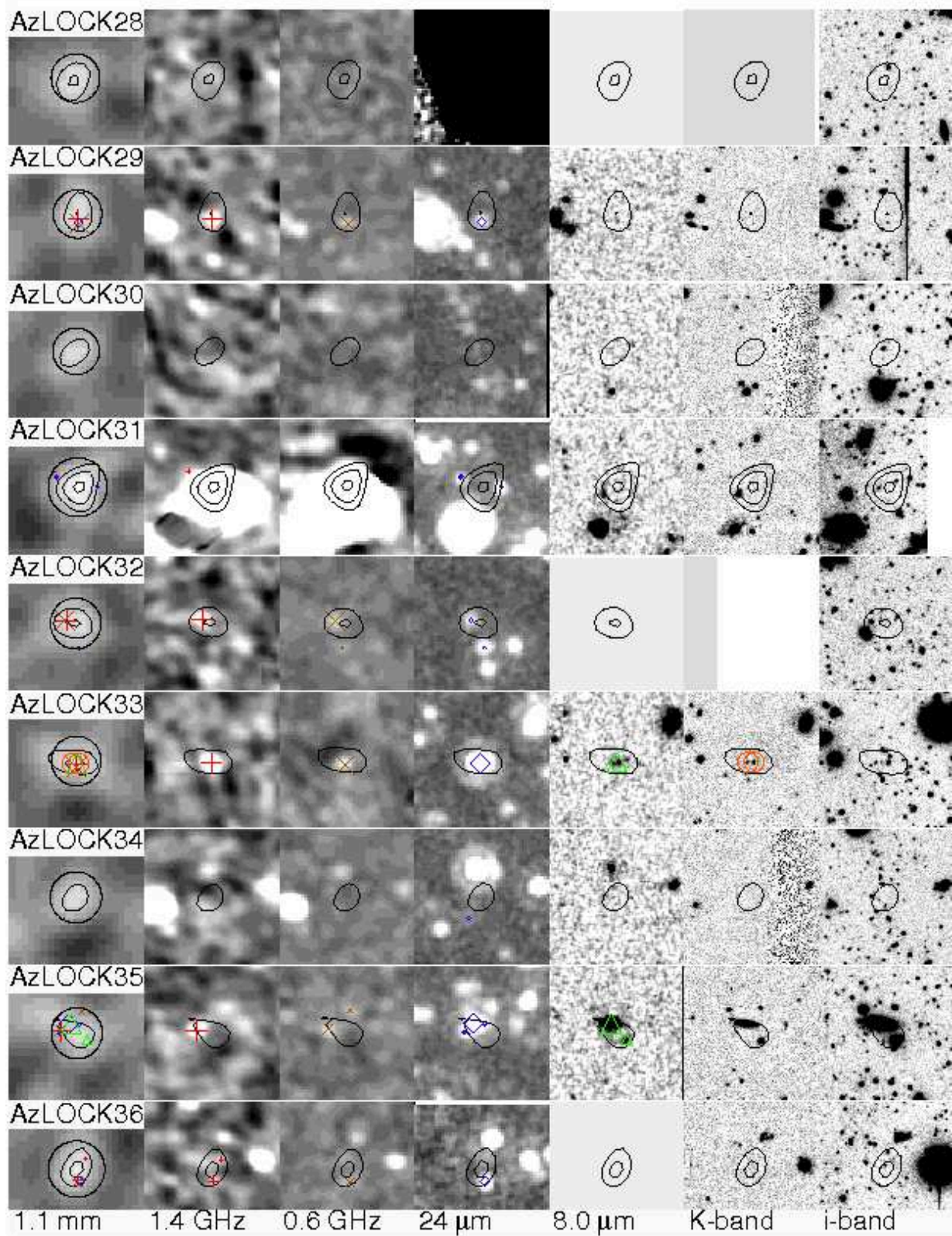
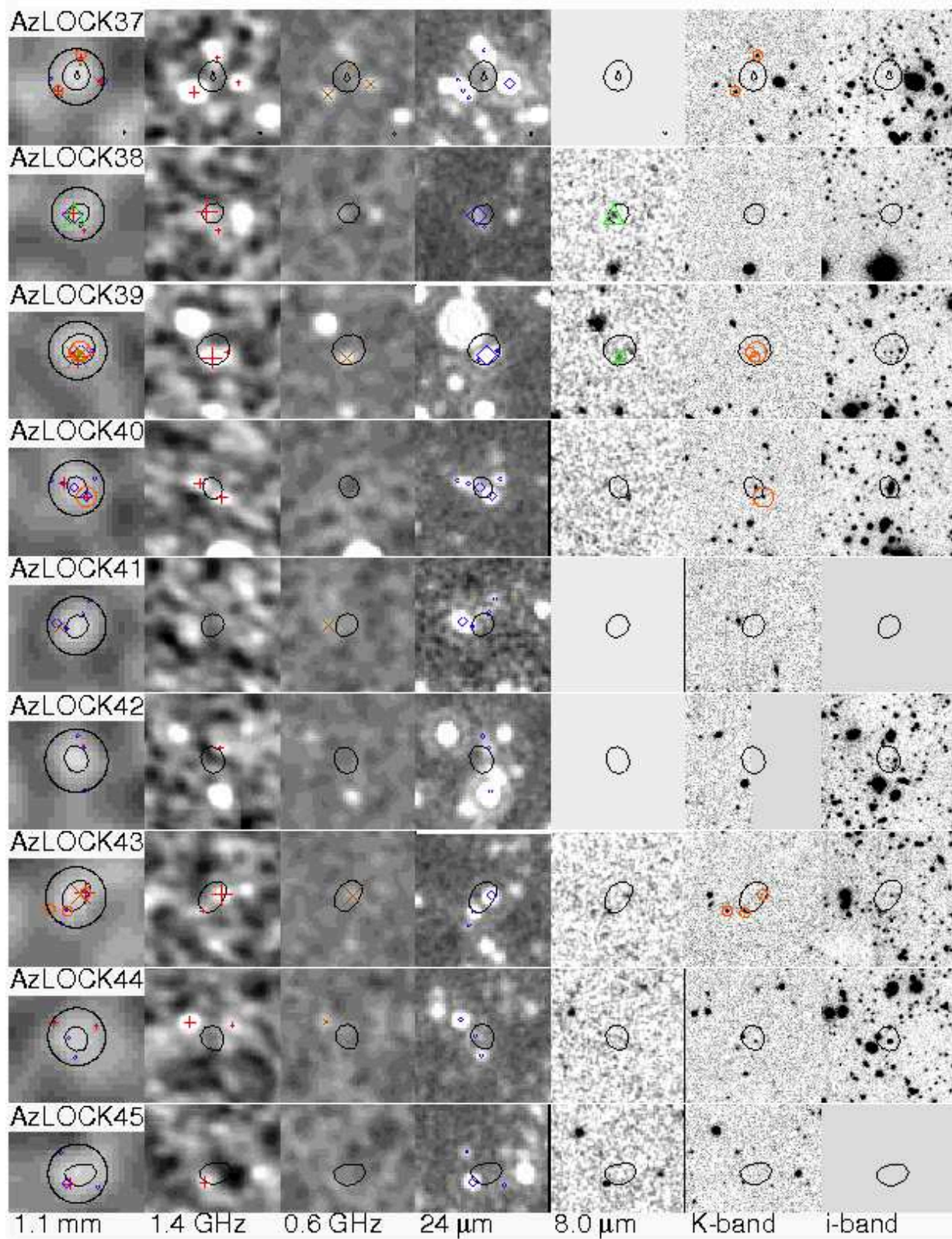


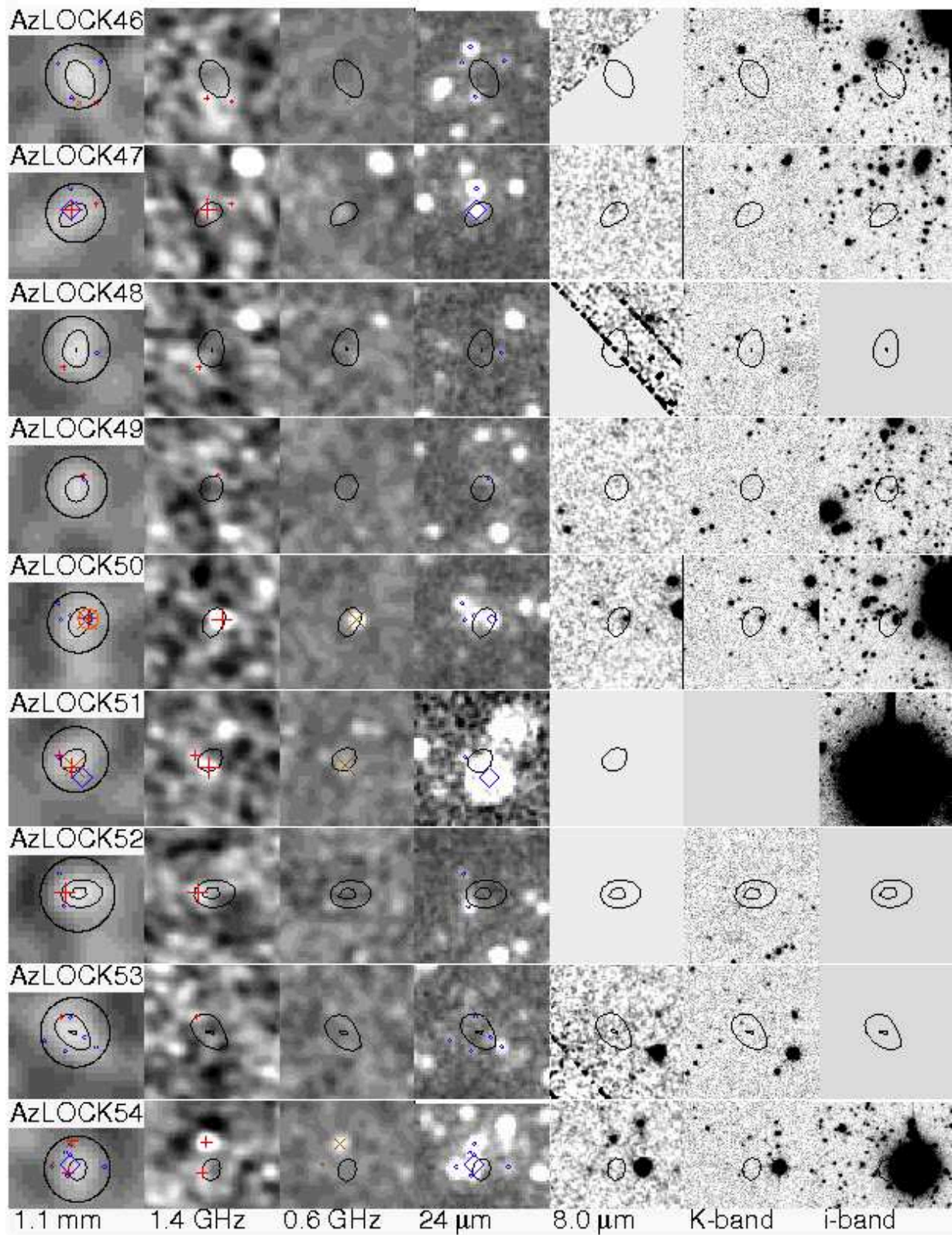
Figure B1. Thumbnail images of AzTEC sources in the Lockman Hole. Each panel is 60 arcsec on a side and centred on the AzTEC position. From left to right: 1.1 mm, 1.4 GHz, 0.61 GHz, 24 μ m, 8.0 μ m, *K*-band and *i*-band. The IDs are marked on the relevant images: red pluses: 1.4 GHz IDs, blue diamonds: 24 μ m IDs, brown crosses: 0.61 GHz IDs, green triangles: the 8.0 μ m IDs, orange circles: the $i - K > 2$. Big symbols: reliable IDs ($p < 0.05$), medium symbols: tentative IDs ($0.05 < P < 0.1$), small symbols: bad IDs ($p > 0.1$). On the 1.1 mm images all the ID symbols as well as a thick circle corresponding to the search radius (Sec. 3) are shown. The contours represent 1.1 mm flux and start at 3 mJy with a 1 mJy increment. The rest of the images is available in the electronic edition of the Journal.

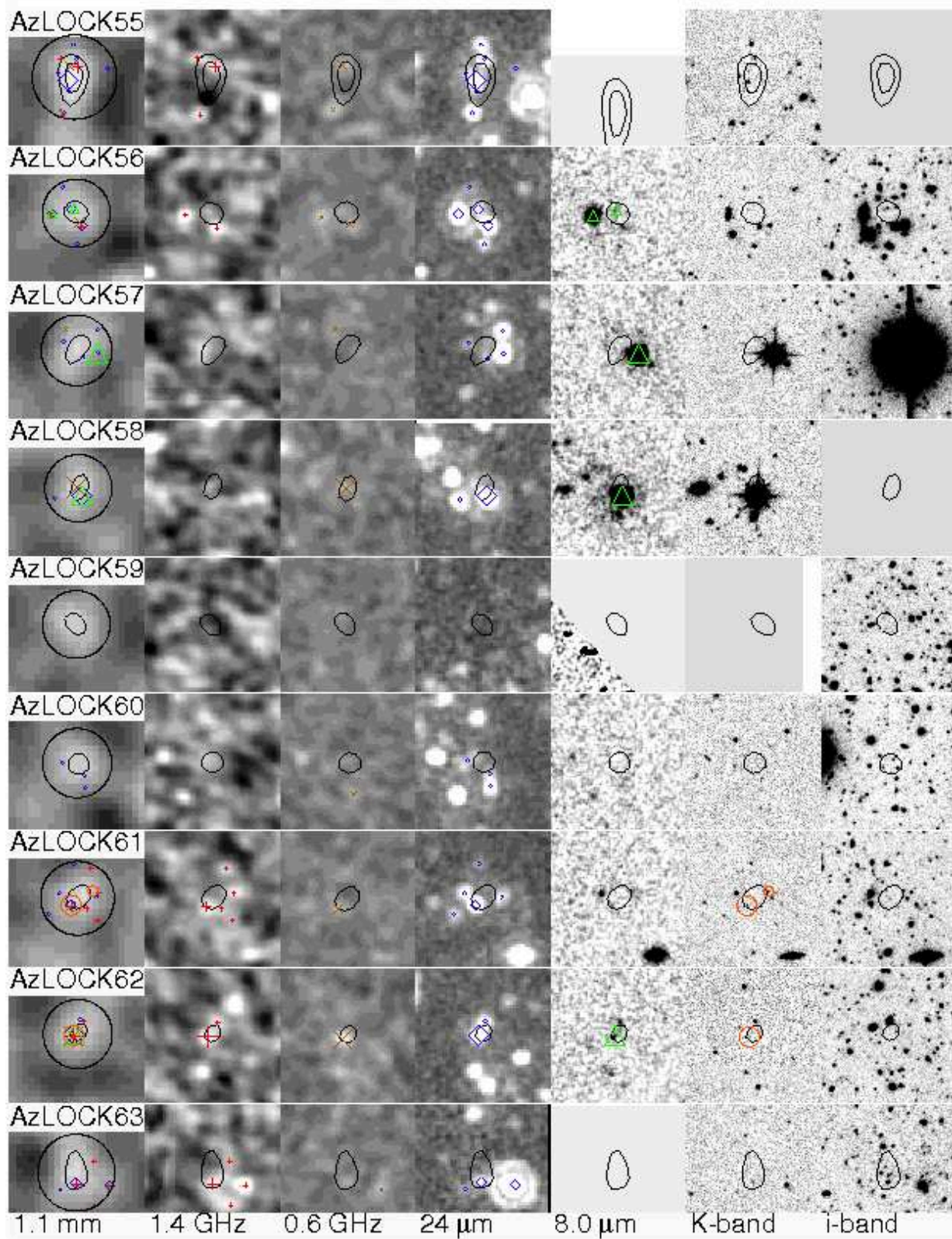


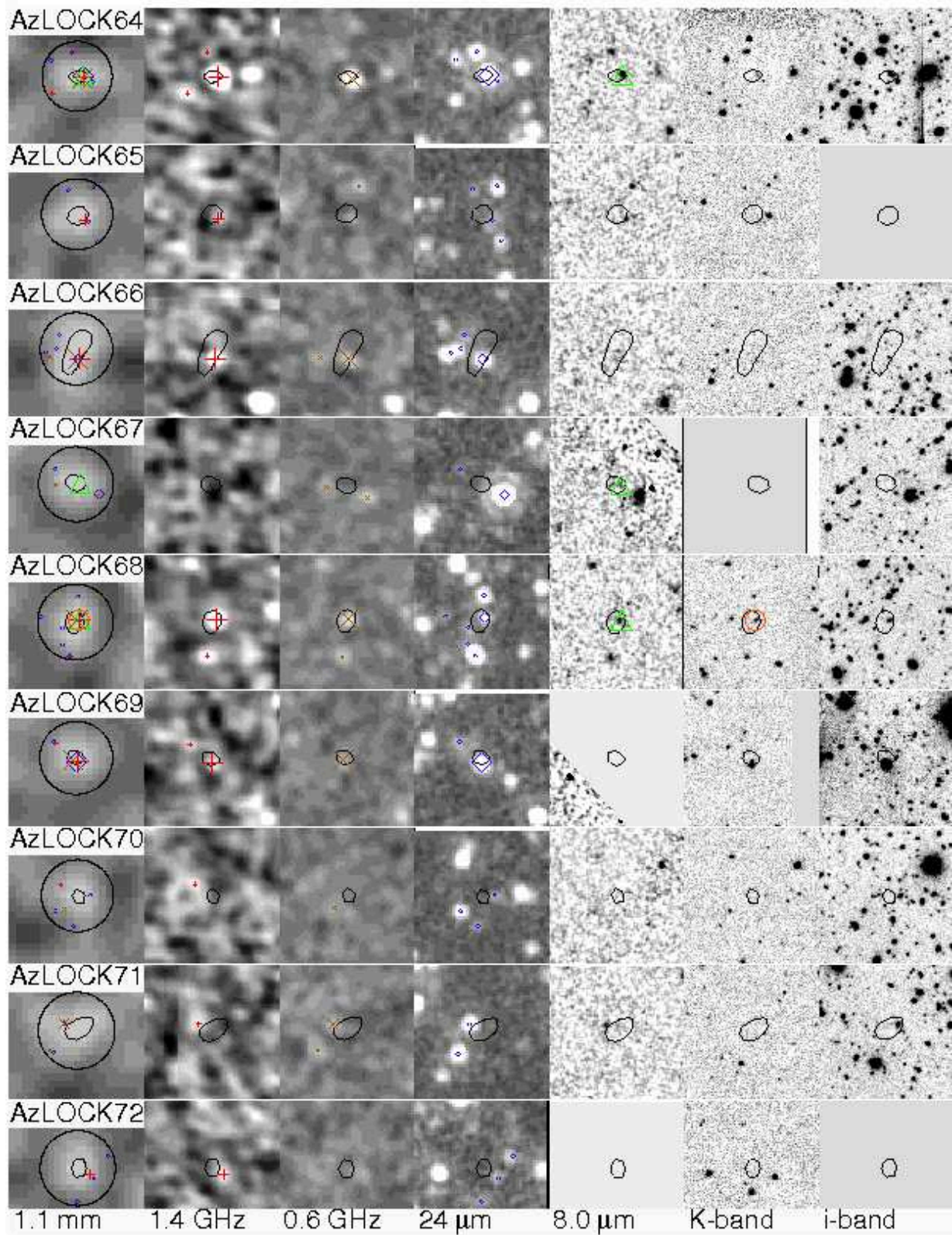


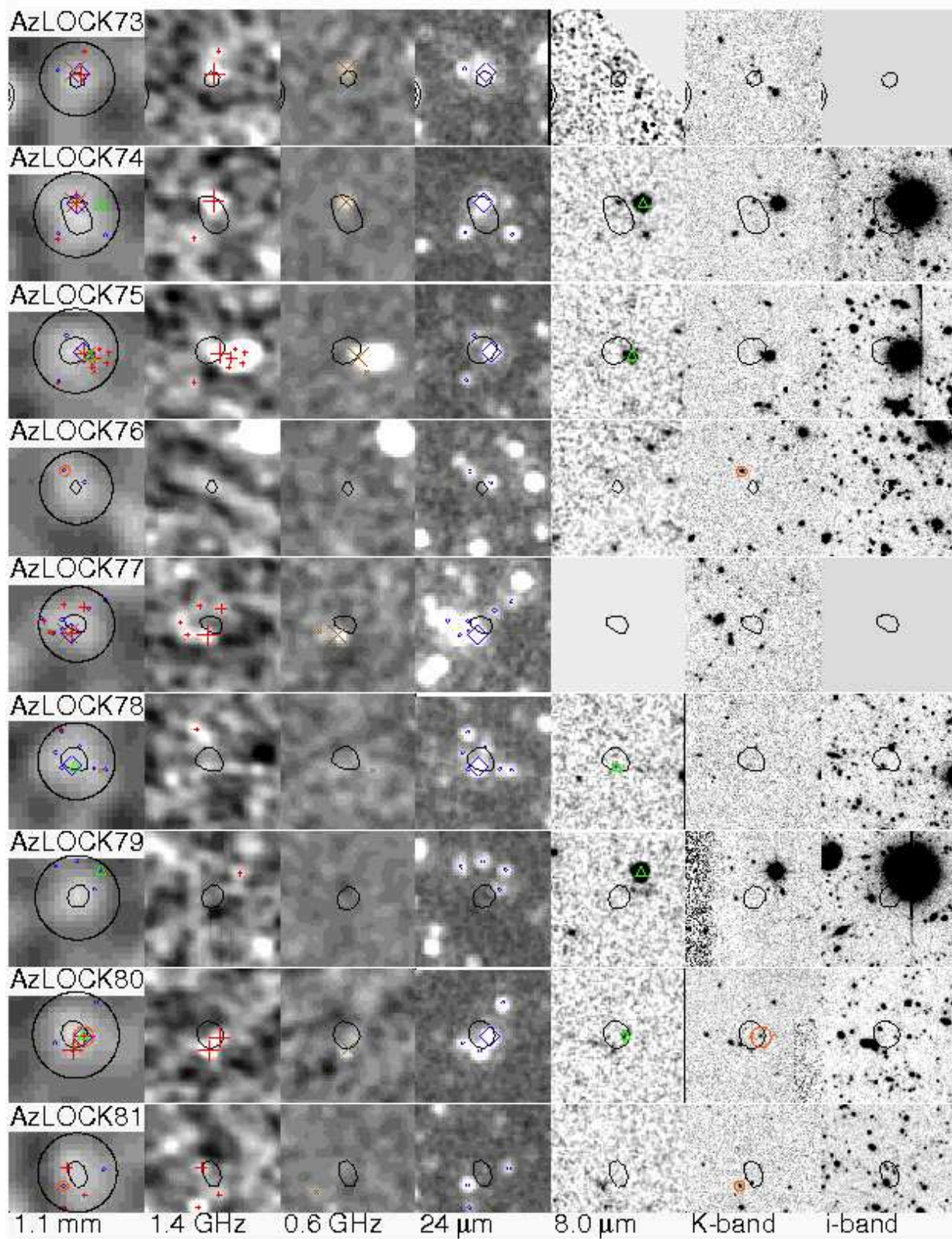


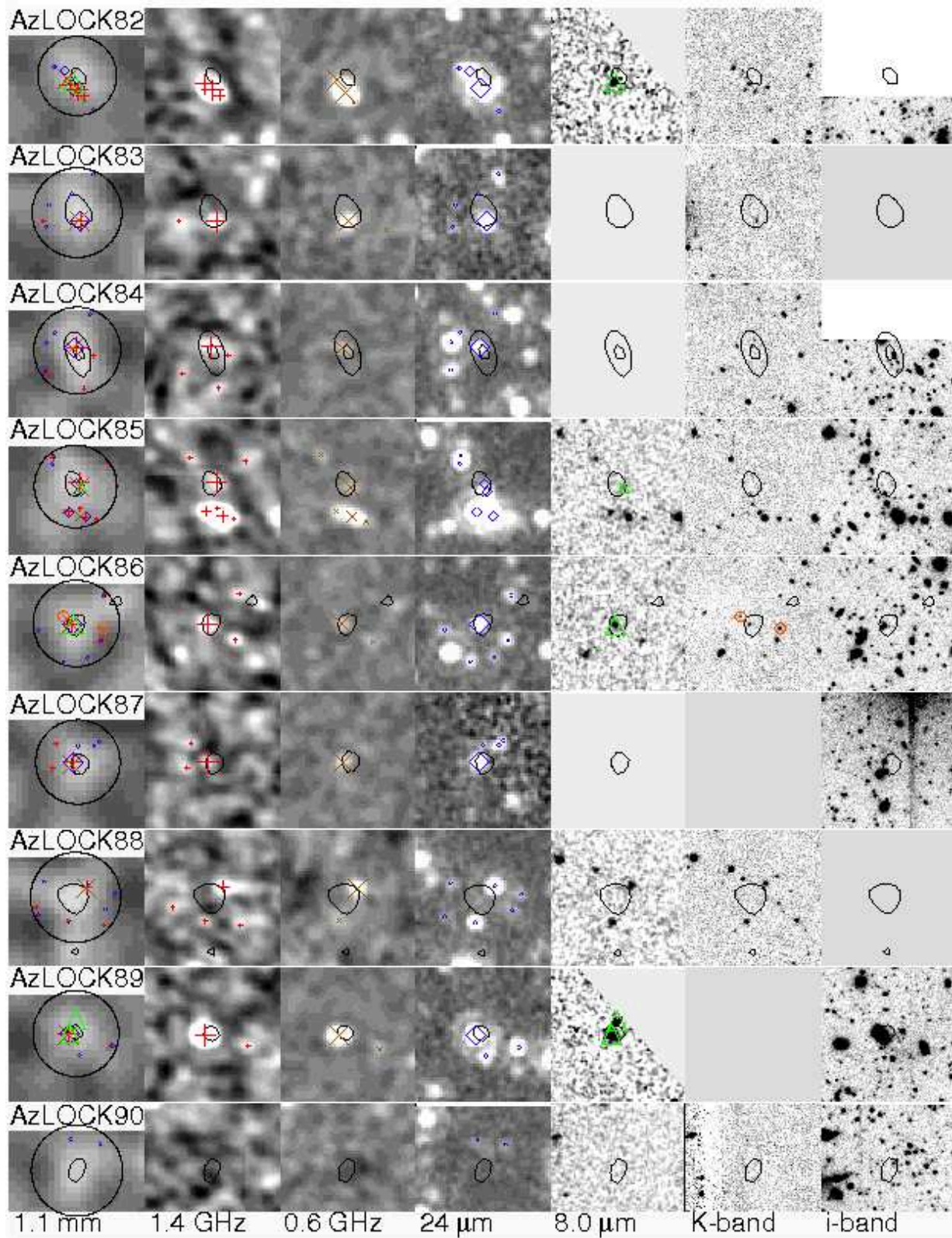


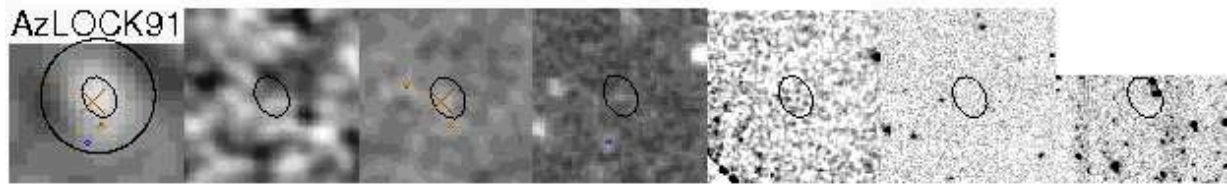












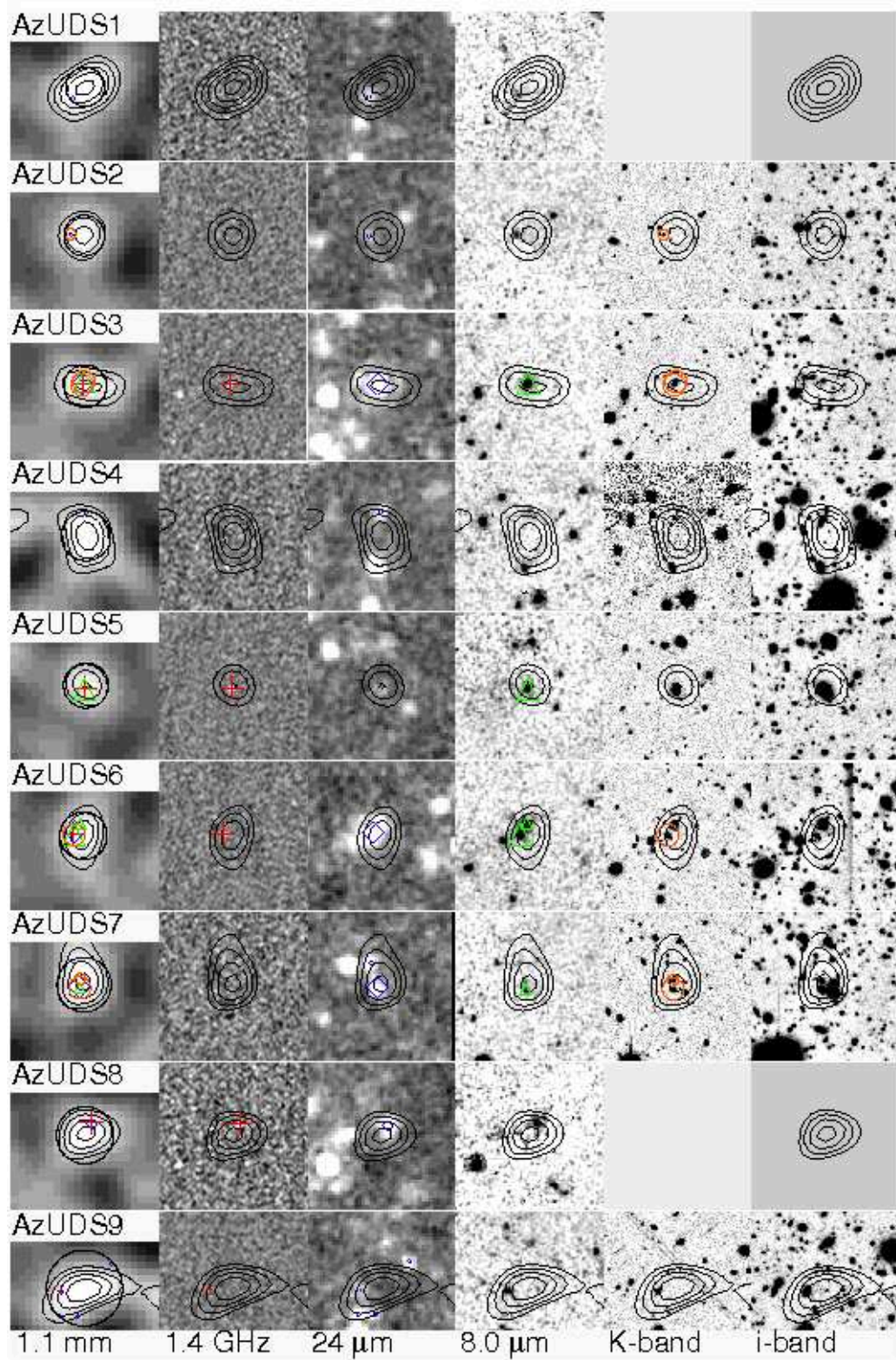
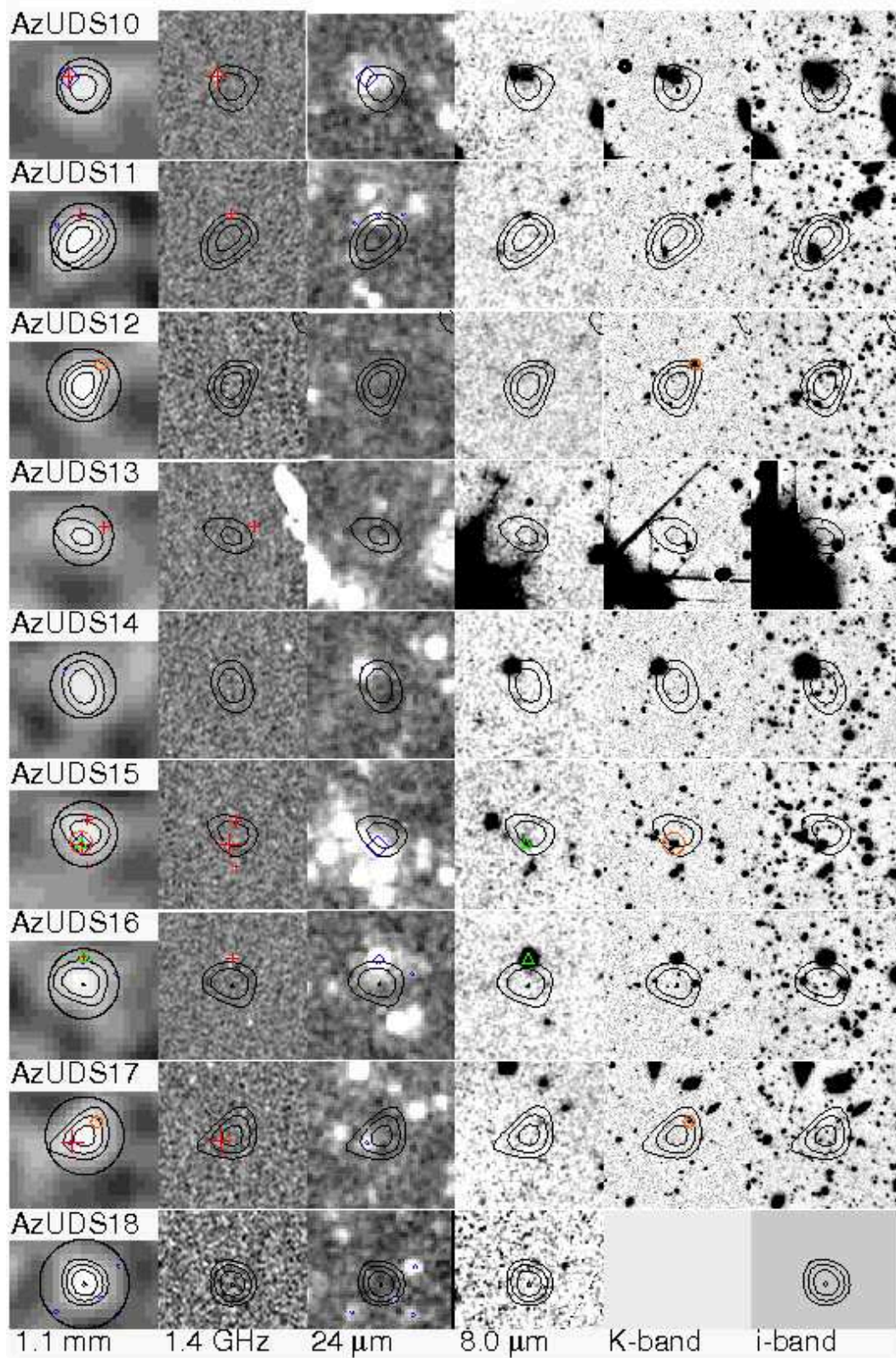
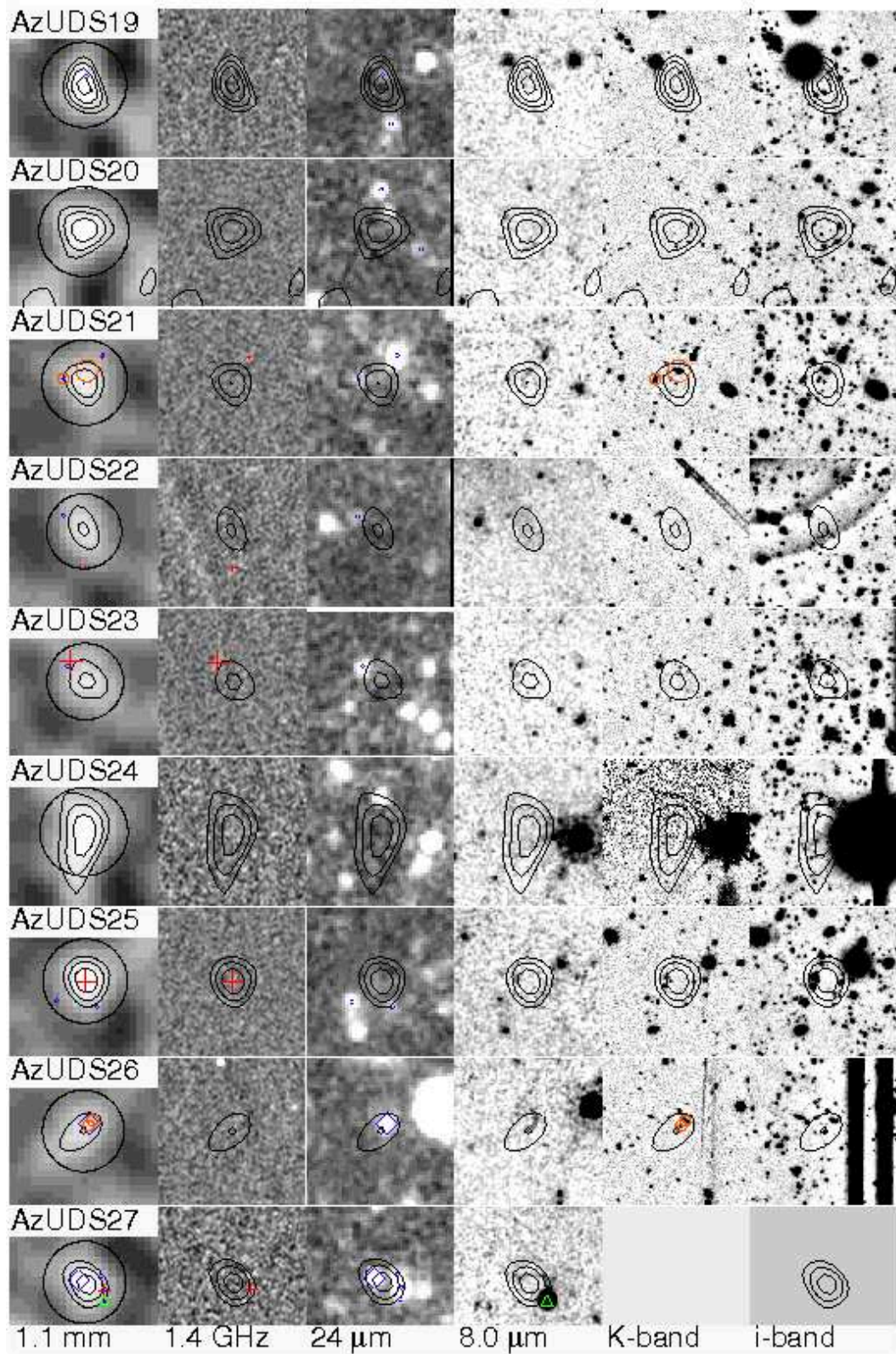
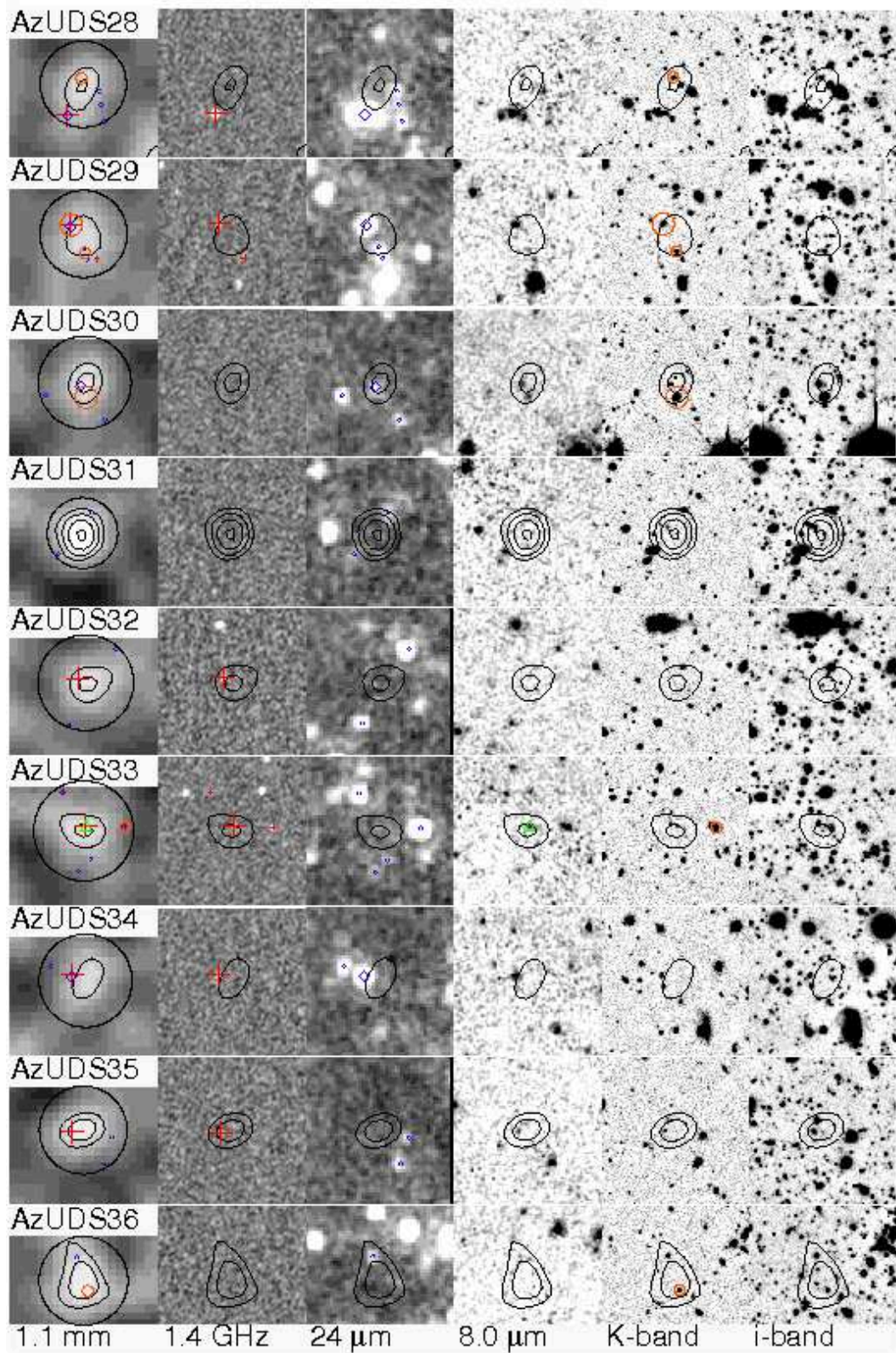
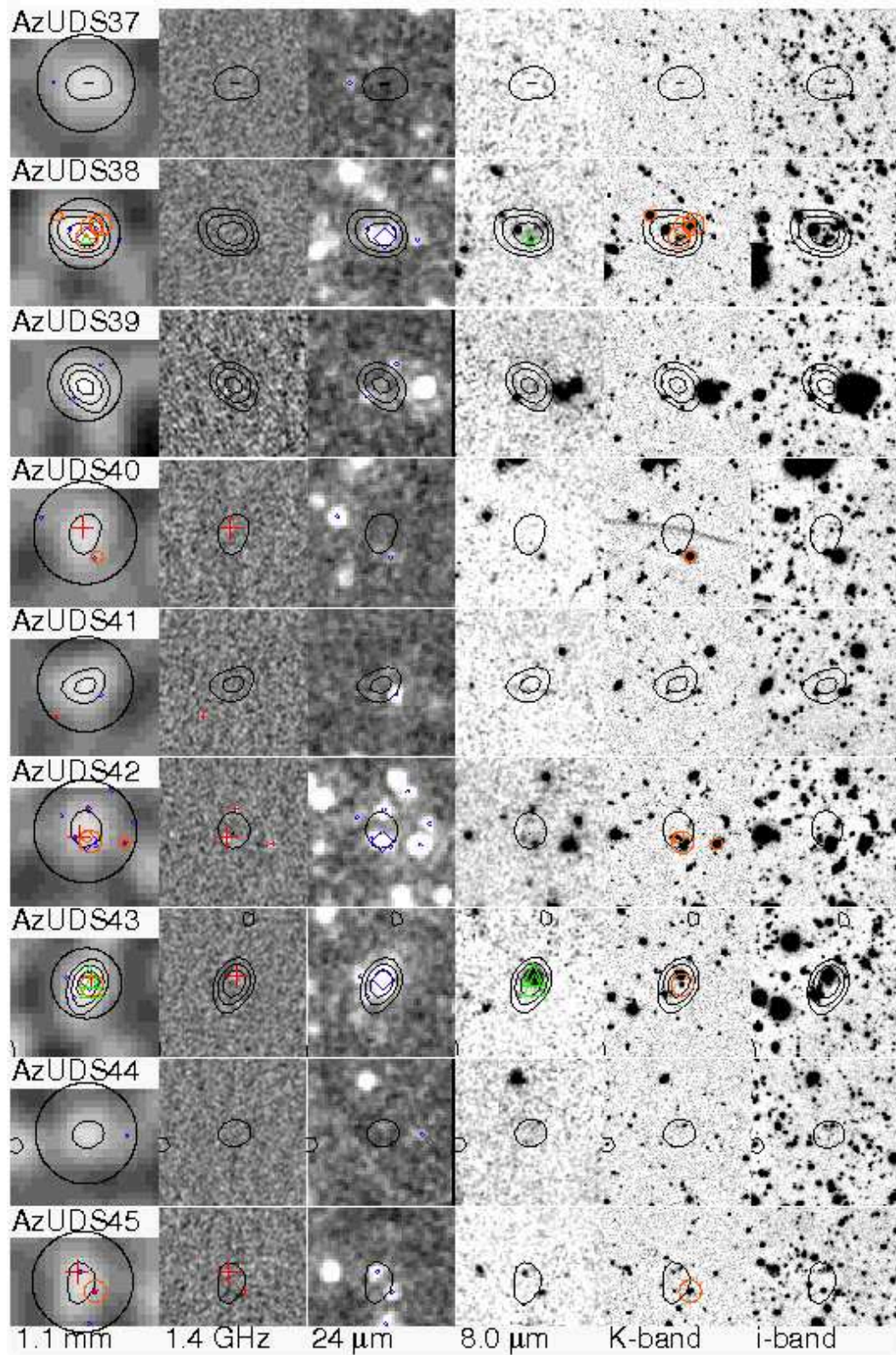


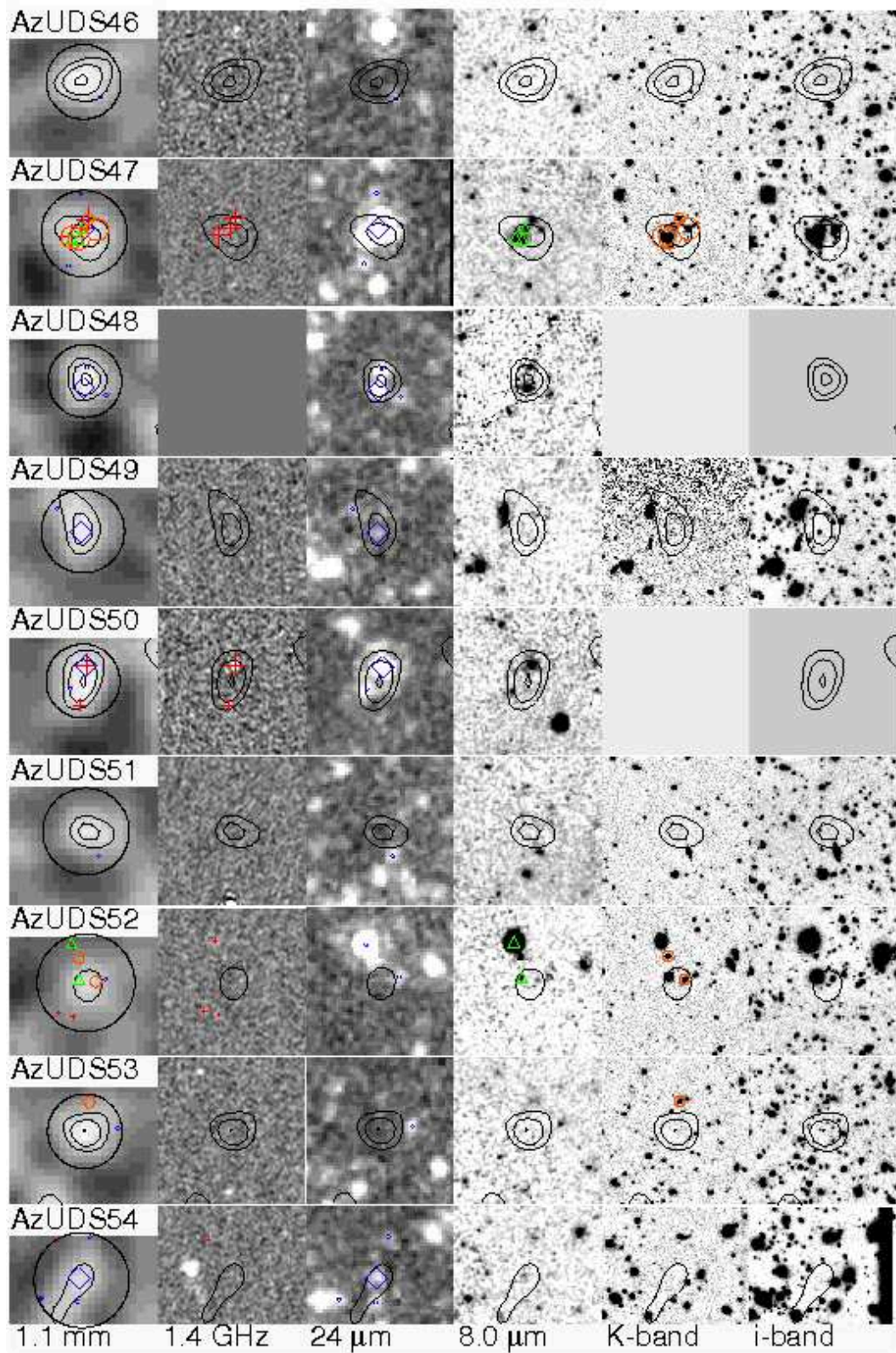
Figure B2. Thumbnail images of AzTEC sources in the UDS field. Symbols are the same as in Fig. B1. The rest of the images is available in the electronic edition of the Journal.











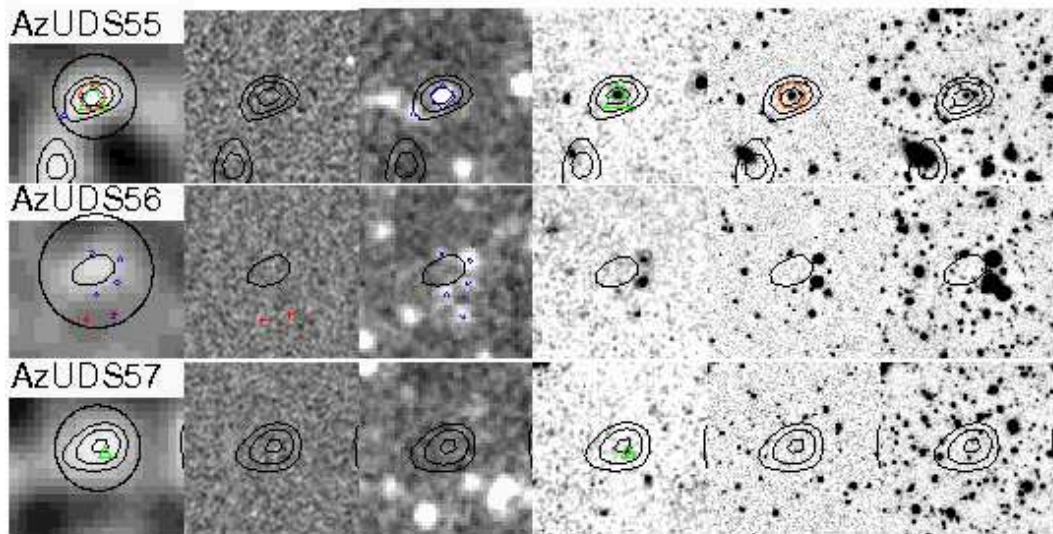


Table B3: Radio and 24 μm identifications in the Lockman Hole field.

No.	$S_{1.1\mu\text{m}}$ (mJy)	RA _{1.4} (deg)	DEC _{1.4} (deg)	$S_{1.4}$ (μJy)	Dist. ($''$)	p	RA ₂₄ (deg)	DEC ₂₄ (deg)	S_{24} (μJy)	Dist. ($''$)	p	RA _{0.61} (deg)	DEC _{0.61} (deg)	$S_{0.61}$ (μJy)	Dist. ($''$)	p
1	$6.63^{+0.85}_{-0.97}$	163.008040	57.681007	258 ± 11	2.3	0.002	163.008072	57.681003	1642 ± 11	2.3	0.002	163.008390	57.680893	596 ± 24	1.9	0.001
...	163.011618	57.679160	123 ± 14	7.8	0.206
2	$6.43^{+0.90}_{-0.89}$	163.022900	57.607548	66 ± 8	6.5	0.038	163.023461	57.607408	235 ± 6	5.4	0.070
3	$6.21^{+1.05}_{-0.92}$	163.237710	57.350926	67 ± 7	2.8	0.011	163.237751	57.350931	636 ± 13	2.8	0.008	163.237780	57.351320	149 ± 16	1.5	0.004
...	...	163.237530	57.352273	36 ± 7	2.6	0.019
4	$5.27^{+0.91}_{-0.97}$	162.686880	57.556959	150 ± 12	7.4	0.021	162.687180	57.556781	121 ± 17	7.1	0.045
...	...	162.686160	57.554737	56 ± 11	2.1	0.009	162.686322	57.554857	284 ± 13	2.2	0.013	162.686720	57.554341	99 ± 17	3.9	0.025
...	...	162.682660	57.555667	43 ± 11	5.5	0.044
...	162.687226	57.553517	30 ± 4	6.8	0.359
5	$4.91^{+1.02}_{-0.90}$	163.515860	57.431498	138 ± 9	0.5	0.000	163.515574	57.431619	232 ± 6	0.3	0.000	163.516050	57.431526	277 ± 19	0.7	0.000
6	$4.75^{+0.84}_{-1.00}$	163.173650	57.597852	45 ± 8	1.9	0.009	163.174019	57.597864	37 ± 6	1.2	0.052
...	163.174035	57.597818	30 ± 3	1.1	0.057
7	$4.75^{+0.89}_{-1.06}$	163.017480	57.448871	102 ± 6	5.2	0.018	163.017287	57.449199	422 ± 16	4.0	0.023	163.017530	57.448910	189 ± 14	5.1	0.019
...	...	163.015030	57.451904	49 ± 6	6.7	0.050	163.015357	57.451936	1179 ± 13	6.6	0.016	163.016060	57.451601	58 ± 15	5.2	0.056
8	$4.65^{+0.97}_{-0.98}$	163.005230	57.412690	110 ± 6	2.8	0.006	163.005188	57.412736	233 ± 5	2.9	0.027	163.005520	57.412444	114 ± 16	2.3	0.010
9	$4.09^{+0.90}_{-0.92}$	163.059220	57.557859	68 ± 8	0.8	0.001	163.059445	57.557446	21 ± 5	0.8	0.045	163.058850	57.557735	144 ± 19	0.9	0.002
...	163.058446	57.558749	202 ± 18	4.3	0.059
...	163.057054	57.555872	86 ± 5	7.7	0.261
10	$4.15^{+0.93}_{-0.92}$	163.528620	57.552436	77 ± 9	3.5	0.014	163.528550	57.552555	819 ± 12	3.3	0.008	163.529300	57.552327	230 ± 27	4.9	0.015
11	$3.79^{+0.97}_{-0.89}$	162.877010	57.635730	245 ± 11	2.0	0.002	162.876902	57.635812	1120 ± 10	2.1	0.002	162.877350	57.635653	428 ± 22	2.4	0.002
...	...	162.877810	57.634337	35 ± 11	4.7	0.044
12	$3.79^{+0.88}_{-0.95}$	163.069630	57.582199	27 ± 9	7.0	0.074
...	163.072956	57.583444	39 ± 3	2.5	0.137	163.073580	57.583051	80 ± 19	4.3	0.034
13	$4.15^{+1.02}_{-1.11}$	162.921340	57.721734	77 ± 18	7.5	0.039	162.921717	57.721935	285 ± 4	7.3	0.089	162.922070	57.721982	171 ± 22	7.6	0.037
14	$3.61^{+0.92}_{-0.94}$	163.084400	57.665143	35 ± 9	0.6	0.002	163.084430	57.664533	173 ± 8	2.8	0.036
15	$3.73^{+0.94}_{-1.00}$	163.235830	57.706780	88 ± 12	3.8	0.013	163.235873	57.706928	441 ± 8	3.4	0.017	163.236410	57.706625	132 ± 20	4.9	0.026
16	$3.65^{+0.96}_{-0.95}$	163.422140	57.537473	121 ± 8	1.9	0.003	163.422245	57.537543	533 ± 10	1.6	0.004	163.422620	57.537360	216 ± 24	1.6	0.003
...	163.425379	57.538780	183 ± 7	5.9	0.104
17	$3.61^{+1.02}_{-0.98}$	163.329930	57.352418	105 ± 6	4.1	0.012	163.330322	57.352432	406 ± 6	3.8	0.022	163.330090	57.352413	263 ± 14	3.9	0.009
18	$3.19^{+0.97}_{-0.90}$	163.103080	57.643072	97 ± 30	3.8	0.025
19	$3.19^{+0.97}_{-0.92}$	162.873630	57.613839	106 ± 11	1.1	0.001	162.873701	57.613663	194 ± 6	1.1	0.007	162.873830	57.613666	162 ± 20	1.4	0.003
...	162.870019	57.614230	143 ± 6	6.3	0.141
20	$3.37^{+1.11}_{-1.08}$	163.438430	57.277931	31 ± 8	6.9	0.077	163.438389	57.277666	174 ± 12	7.8	0.164
...	...	163.440710	57.280218	26 ± 8	2.6	0.029
...	163.441198	57.277670	60 ± 7	7.9	0.356
21	$3.07^{+0.91}_{-0.97}$	162.882483	57.528237	163 ± 6	8.1	0.176
...	162.880905	57.524897	210 ± 6	4.5	0.061
...	162.881545	57.526417	25 ± 2	1.6	0.117
22	$3.19^{+1.10}_{-0.99}$	163.233880	57.400757	93 ± 5	6.7	0.030	163.233200	57.401123	63 ± 17	8.4	0.089
...	...	163.235770	57.399629	76 ± 5	2.0	0.006	163.235570	57.398985	976 ± 72	0.5	0.000	163.235270	57.399845	267 ± 16	2.7	0.005
...	...	163.235610	57.398088	19 ± 6	3.7	0.058	163.236310	57.397990	84 ± 16	4.4	0.037
...	...	163.231580	57.398130	17 ± 6	8.2	0.086
23	$3.13^{+1.04}_{-1.12}$	163.338730	57.288664	40 ± 8	5.6	0.054	163.339525	57.288594	376 ± 37	4.1	0.029
...	163.340381	57.286669	35 ± 6	6.2	0.413
24	$3.01^{+1.04}_{-1.06}$	163.159970	57.411082	42 ± 5	3.2	0.024	163.160031	57.411485	88 ± 20	4.6	0.157	163.159940	57.410476	132 ± 15	1.1	0.003
...	...	163.159440	57.409936	32 ± 5	1.9	0.015	163.160159	57.410157	370 ± 28	0.3	0.000	163.159940	57.410476	132 ± 15	1.1	0.003
...	...	163.162320	57.412221	14 ± 5	8.2	0.086
25	$2.73^{+1.04}_{-0.93}$	162.777040	57.576881	56 ± 11	7.2	0.056	162.776500	57.576868	1126 ± 26	7.9	0.025	162.777330	57.577005	83 ± 27	6.5	0.064
...	...	162.781960	57.577321	42 ± 11	6.3	0.061
26	$3.07^{+1.14}_{-1.26}$	162.748710	57.276582	28 ± 8	1.1	0.008	162.748983	57.276752	70 ± 6	0.4	0.004	162.748960	57.276601	67 ± 15	1.0	0.005
...	...	162.748020	57.279106	26 ± 7	8.3	0.121
...	162.744920	57.278801	52 ± 15	10.5	0.132

27	$2.89^{+1.10}_{-1.13}$	163.079530	57.316107	122 ± 6	6.2	0.022	163.079603	57.316099	239 ± 27	6.3	0.096	163.080110	57.315767	188 ± 12	6.1	0.028
...	163.082598	57.314697	357 ± 8	9.5	0.118
...	163.078117	57.314455	48 ± 3	1.2	0.043
28	$2.73^{+1.11}_{-1.08}$
29	$2.73^{+1.05}_{-1.08}$	162.847080	57.366224	51 ± 5	2.4	0.014	162.846960	57.365802	132 ± 6	4.0	0.092	162.846750	57.365700	84 ± 14	4.4	0.041
30	$2.65^{+0.94}_{-1.09}$
31	$3.13^{+1.44}_{-1.60}$	163.610970	57.620802	67 ± 18	12.7	0.119
...	163.600920	57.618918	155 ± 5	8.8	0.260
...	163.610438	57.619999	54 ± 3	10.4	0.609
...	163.610370	57.620138	49 ± 9	10.5	0.633
32	$2.73^{+1.12}_{-1.16}$	162.673560	57.358630	45 ± 7	4.2	0.037	162.673860	57.358644	145 ± 7	4.8	0.111	162.674020	57.358556	128 ± 18	5.0	0.033
...	162.670881	57.355197	183 ± 4	11.0	0.274
...	162.672330	57.355239	50 ± 16	10.9	0.149
33	$2.51^{+1.03}_{-1.02}$	163.191330	57.522224	83 ± 7	1.2	0.002	163.191746	57.522194	1009 ± 36	1.5	0.002	163.191400	57.521754	145 ± 40	2.9	0.012
34	$2.65^{+1.03}_{-1.21}$	163.162951	57.387493	68 ± 5	11.2	0.524
35	$2.51^{+1.01}_{-1.10}$	163.486250	57.498767	79 ± 8	6.9	0.043	163.486757	57.498488	57 ± 13	7.8	0.443	163.486520	57.498862	141 ± 25	7.5	0.053
...	163.484690	57.499650	475 ± 29	5.6	0.039
...	163.482260	57.499574	40 ± 6	3.9	0.279
...	163.482261	57.499612	33 ± 4	4.0	0.333
...	163.486917	57.498591	26 ± 8	8.1	0.593	163.486520	57.498862	141 ± 25	7.5	0.053
...	163.481650	57.501131	86 ± 25	9.6	0.108	
36	$2.73^{+1.22}_{-1.32}$	163.456170	57.266529	29 ± 9	4.9	0.073	163.455746	57.266403	223 ± 7	5.5	0.093	163.456220	57.266335	93 ± 17	5.6	0.056
...	...	163.454640	57.269161	27 ± 9	6.0	0.103
37	$2.65^{+1.12}_{-1.32}$	162.973890	57.224526	110 ± 7	10.3	0.057	162.974277	57.224773	389 ± 14	10.4	0.133	162.973990	57.224300	146 ± 13	11.0	0.090
...	...	162.963760	57.225744	70 ± 7	11.7	0.101	162.963737	57.225631	859 ± 15	11.8	0.069	162.964290	57.225575	132 ± 15	10.8	0.096
...	...	162.968490	57.228701	31 ± 8	9.1	0.139
...	162.969598	57.229672	584 ± 38	12.3	0.111
...	162.975480	57.226052	26 ± 6	11.3	0.611
...	162.973006	57.223882	29 ± 4	10.7	0.654	162.973990	57.224300	146 ± 13	11.0	0.090
...	162.968830	57.227743	48 ± 15	5.6	0.102	
38	$2.35^{+0.98}_{-1.07}$	162.819690	57.536226	40 ± 9	2.3	0.017	162.819698	57.536024	109 ± 5	2.3	0.050
...	...	162.817100	57.534008	24 ± 8	8.0	0.137
...	162.817929	57.534583	35 ± 3	5.6	0.454
39	$2.51^{+1.13}_{-1.27}$	163.051110	57.263759	91 ± 6	3.0	0.011	163.050327	57.263995	276 ± 20	2.6	0.022	163.051060	57.263704	162 ± 12	3.2	0.013
...	...	163.047620	57.264366	29 ± 6	6.8	0.112	163.047705	57.264598	41 ± 6	6.6	0.505
...	163.051879	57.263439	20 ± 6	4.4	0.541	163.051060	57.263704	162 ± 12	3.2	0.013
...	163.047740	57.264637	27 ± 4	6.5	0.604
...	163.051933	57.263438	34 ± 8	4.4	0.391	163.051060	57.263704	162 ± 12	3.2	0.013
40	$2.27^{+1.02}_{-1.03}$	163.113650	57.565914	53 ± 8	6.0	0.054	163.114050	57.565839	194 ± 13	6.6	0.138
...	...	163.108470	57.564205	50 ± 9	5.9	0.057	163.108537	57.564300	256 ± 8	5.6	0.081
...	163.106617	57.566446	137 ± 19	9.0	0.285
...	163.111345	57.565350	27 ± 2	1.1	0.078
...	163.116447	57.566183	31 ± 4	11.4	0.637
41	$2.35^{+1.07}_{-1.19}$	162.822738	57.674594	467 ± 25	9.0	0.090	162.822080	57.674117	85 ± 24	7.7	0.096
...	162.815233	57.677330	136 ± 2	12.3	0.416
...	162.820507	57.673946	31 ± 5	4.8	0.455
...	162.816648	57.675723	31 ± 6	5.9	0.538
...	162.820648	57.674002	27 ± 4	5.0	0.508
42	$2.35^{+1.19}_{-1.24}$	162.741040	57.313558	25 ± 6	6.9	0.137	162.741298	57.313471	125 ± 8	6.4	0.214
...	162.740899	57.308206	1035 ± 76	13.8	0.175
...	162.742499	57.314974	34 ± 3	11.1	0.737
43	$2.35^{+1.12}_{-1.22}$	162.969100	57.356797	41 ± 6	4.5	0.049	162.969181	57.356773	261 ± 5	4.3	0.055	162.970050	57.356670	74 ± 13	2.7	0.025
...	...	162.973420	57.354826	21 ± 7	6.8	0.147	162.973279	57.354767	196 ± 7	6.8	0.150
...	162.974519	57.353088	34 ± 2	13.3	0.707
44	$2.25^{+1.01}_{-1.12}$	163.179740	57.570097	80 ± 8	11.9	0.093	163.179551	57.570206	332 ± 6	11.8	0.187	163.179450	57.569914	96 ± 20	11.1	0.129
...	...	163.169940	57.569688	28 ± 8	9.9	0.164
...	163.174804	57.565838	219 ± 6	9.2	0.198
...	163.176280	57.568225	86 ± 4	3.5	0.130
45	$2.21^{+1.04}_{-1.11}$	162.980280	57.638882	52 ± 9	5.9	0.055	162.980860	57.638985	335 ± 7	6.3	0.075

59	$2.05^{+1.08}_{-1.20}$	163.182610	57.678603	74 ± 22	0.5	0.001
60	$2.05^{+1.11}_{-1.22}$	163.438331	57.443009	246 ± 23	11.6	0.260	
...	163.443506	57.446084	185 ± 18	6.5	0.154	
...	163.438482	57.444546	30 ± 3	6.4	0.634	
...	163.438950	57.442131	60 ± 17	14.4	0.246	
61	$2.05^{+1.21}_{-1.27}$	163.239680	57.379146	29 ± 4	4.5	0.075	163.239877	57.379325	272 ± 8	4.3	0.054	163.240120	57.379084	74 ± 19	5.2	0.074	
...	...	163.233530	57.380782	24 ± 5	9.6	0.219	163.233900	57.380335	198 ± 5	8.6	0.220	
...	...	163.235300	57.383806	18 ± 5	14.4	0.281	
...	...	163.233800	57.377434	15 ± 4	13.1	0.276	
...	...	163.236230	57.378896	14 ± 4	6.1	0.205	
...	163.244851	57.378211	200 ± 10	14.5	0.416	
...	163.242418	57.380773	138 ± 5	8.3	0.291	
...	163.239095	57.384391	48 ± 3	15.3	0.828	
62	$1.95^{+1.05}_{-1.16}$	163.049240	57.586139	65 ± 7	1.8	0.007	163.049282	57.586310	272 ± 7	1.7	0.011	163.049370	57.586009	167 ± 20	2.2	0.008	
...	...	163.047070	57.587930	30 ± 6	6.3	0.113	163.047842	57.588108	136 ± 40	6.5	0.208	
63	$2.05^{+1.19}_{-1.40}$	163.518080	57.343389	73 ± 9	15.8	0.171	163.518027	57.343446	1722 ± 10	15.8	0.056	163.517710	57.342985	89 ± 18	17.0	0.258	
...	...	163.525460	57.343559	37 ± 9	5.3	0.077	163.525736	57.343755	190 ± 31	4.5	0.090	
...	...	163.521410	57.340985	31 ± 9	16.7	0.299	
...	...	163.521660	57.346403	26 ± 9	9.2	0.206	
...	163.529224	57.342892	23 ± 2	10.4	0.863	
64	$1.95^{+1.07}_{-1.18}$	163.294160	57.576504	188 ± 7	2.8	0.004	163.294141	57.576623	457 ± 9	2.9	0.015	163.294440	57.576334	347 ± 22	2.4	0.004	
...	...	163.301240	57.574446	26 ± 7	13.3	0.255	
...	...	163.296730	57.579536	19 ± 6	10.8	0.255	163.296858	57.579518	187 ± 5	10.8	0.307	
...	163.301718	57.578523	108 ± 6	13.7	0.577	
...	163.292141	57.575910	22 ± 4	7.1	0.761	
65	$1.97^{+1.08}_{-1.22}$	163.241560	57.659149	32 ± 11	4.2	0.062	163.240715	57.658914	142 ± 6	6.1	0.184	
...	163.239593	57.663206	192 ± 9	14.0	0.407	163.240270	57.663064	94 ± 22	13.0	0.182	
...	163.238716	57.656411	115 ± 5	15.3	0.610	
...	163.245393	57.662807	44 ± 2	11.3	0.757	
66	$1.95^{+1.08}_{-1.24}$	163.463590	57.514934	67 ± 8	4.7	0.034	163.464103	57.514901	230 ± 15	4.6	0.074	163.464090	57.514930	107 ± 20	4.5	0.040	
...	163.471436	57.515665	274 ± 19	13.7	0.298	
...	163.469049	57.516174	33 ± 8	8.9	0.748	
...	163.468278	57.517870	44 ± 3	9.6	0.704	
...	163.470520	57.515076	76 ± 20	12.4	0.206	
67	$1.89^{+1.14}_{-1.19}$	162.683620	57.488883	888 ± 13	11.2	0.067	162.684230	57.488735	108 ± 17	10.3	0.131	
...	162.693663	57.492084	27 ± 2	11.6	0.852	
...	162.693550	57.490056	64 ± 14	9.0	0.172	
68	$1.95^{+1.12}_{-1.31}$	163.356740	57.380114	75 ± 6	2.3	0.009	163.356830	57.380301	100 ± 6	2.5	0.072	163.357420	57.380083	138 ± 15	1.2	0.003	
...	...	163.358980	57.375635	45 ± 7	15.3	0.231	163.359033	57.375581	370 ± 10	15.5	0.272	163.358680	57.375407	101 ± 16	16.0	0.225	
...	163.357126	57.382995	153 ± 7	11.5	0.399	
...	163.365797	57.380437	33 ± 3	15.7	0.858	
...	163.360672	57.379088	40 ± 3	6.2	0.551	
...	163.360626	57.376985	29 ± 2	11.6	0.850	
69	$1.89^{+1.07}_{-1.20}$	162.748590	57.545517	42 ± 11	1.9	0.014	162.748828	57.545503	315 ± 7	1.9	0.011	162.749570	57.545760	60 ± 20	1.5	0.014	
...	...	162.753740	57.547842	34 ± 10	11.4	0.206	162.754023	57.548086	160 ± 17	12.3	0.413	
70	$1.89^{+1.04}_{-1.20}$	162.844050	57.5560717	36 ± 11	8.9	0.151	
...	162.845196	57.557483	251 ± 12	11.7	0.264	
...	162.837212	57.559436	38 ± 3	5.8	0.527	
...	162.841146	57.555595	30 ± 2	13.6	0.831	
...	162.843260	57.557734	67 ± 17	8.3	0.146	
71	$1.89^{+1.14}_{-1.25}$	163.532170	57.500368	28 ± 8	6.6	0.135	163.532010	57.500343	216 ± 8	6.3	0.131	163.532060	57.500234	81 ± 24	6.2	0.088	
...	163.534524	57.496645	278 ± 6	14.1	0.314	163.535550	57.496911	87 ± 23	15.0	0.236	
72	$1.89^{+1.10}_{-1.24}$	162.883580	57.672004	44 ± 12	6.2	0.080	162.882751	57.671566	33 ± 6	8.4	0.740	
...	162.879447	57.674317	88 ± 5	14.4	0.684	
...	162.886674	57.668642	73 ± 12	15.1	0.753	
73	$1.89^{+1.07}_{-1.24}$	162.987140	57.683242	74 ± 11	2.4	0.011	162.987369	57.683353	688 ± 25	2.6	0.008	162.988250	57.683585	117 ± 22	3.4	0.023	
...	...	162.986200	57.686034	37 ± 11	12.5	0.216	
...	162.992324	57.683763	164 ± 8	9.5	0.299	

74	$1.89^{+1.18}_{-1.45}$	163.193130	57.296706	85 ± 6	5.6	0.037	163.193245	57.296453	681 ± 28	4.7	0.022	163.193470	57.296584	148 ± 12	5.2	0.038
...	...	163.197600	57.292134	21 ± 7	13.7	0.347	
...	163.197388	57.292829	191 ± 6	11.6	0.353	
...	163.186690	57.292578	205 ± 5	15.7	0.472	
75	$1.89^{+1.17}_{-1.45}$	163.288440	57.283102	117 ± 7	4.1	0.015	163.288669	57.283156	415 ± 8	3.7	0.026	163.288250	57.282611	290 ± 17	5.2	0.017
...	...	163.286010	57.282503	107 ± 7	9.3	0.062	
...	...	163.282940	57.283178	102 ± 7	14.7	0.125	
...	...	163.283480	57.281806	50 ± 7	14.8	0.227	
...	...	163.285150	57.283616	34 ± 7	10.5	0.210	
...	...	163.286680	57.281393	27 ± 7	10.3	0.243	163.286260	57.280806	95 ± 17	12.4	0.196
...	...	163.294510	57.279466	22 ± 6	16.1	0.359	163.294352	57.279720	80 ± 5	15.1	0.765	
...	163.292614	57.285222	137 ± 2	7.8	0.288	
76	$1.87^{+1.00}_{-1.23}$	163.121471	57.551626	123 ± 26	9.6	0.383	
...	163.116573	57.550207	149 ± 5	4.7	0.122	
77	$1.89^{+1.05}_{-1.30}$	162.951740	57.688409	102 ± 13	4.8	0.022	162.951851	57.688521	386 ± 13	4.6	0.040	162.952580	57.688430	190 ± 27	5.7	0.031
...	...	162.948700	57.691634	58 ± 13	8.2	0.091	162.947825	57.691469	59 ± 4	8.6	0.579	
...	...	162.956370	57.688486	58 ± 13	11.8	0.147	162.955849	57.688485	345 ± 10	10.9	0.180	162.956790	57.688701	85 ± 25	12.4	0.197
...	...	162.958060	57.689926	50 ± 13	14.5	0.204	162.958624	57.690295	410 ± 17	15.7	0.252	
...	...	162.953610	57.691981	40 ± 13	10.4	0.171	
...	162.953880	57.690167	139 ± 19	6.7	0.221	
...	162.943962	57.692553	172 ± 13	16.6	0.535	
...	162.953776	57.688976	17 ± 4	6.5	0.810	
78	$1.89^{+1.06}_{-1.33}$	163.460800	57.568554	34 ± 9	15.8	0.280	163.460704	57.568225	133 ± 5	14.7	0.567	
...	163.456670	57.566393	106 ± 17	6.7	0.285	
...	163.450576	57.563589	154 ± 2	13.5	0.474	163.451580	57.563417	112 ± 27	11.8	0.152
...	163.458285	57.564010	406 ± 9	2.8	0.016	
...	163.453267	57.563724	43 ± 3	8.4	0.674	
...	163.462020	57.565660	46 ± 5	9.9	0.721	
...	163.460613	57.563713	28 ± 3	7.1	0.727	
79	$1.89^{+1.15}_{-1.47}$	163.129490	57.264232	21 ± 6	16.5	0.360	
...	163.132051	57.262251	122 ± 7	8.3	0.346	
...	163.130708	57.264683	90 ± 6	16.0	0.757	
...	163.140810	57.265090	172 ± 13	16.9	0.569	
...	163.135864	57.265720	132 ± 6	16.2	0.640	
80	$1.89^{+1.14}_{-1.54}$	163.577890	57.578058	94 ± 11	6.7	0.043	163.578053	57.577928	286 ± 8	7.2	0.123	163.577230	57.578342	109 ± 29	5.5	0.058
...	...	163.575400	57.579668	61 ± 12	3.8	0.028	163.575766	57.579719	446 ± 6	3.0	0.018	
...	163.572638	57.583961	220 ± 6	17.2	0.497	
...	163.582089	57.578907	155 ± 5	9.9	0.350	
81	$1.89^{+1.05}_{-1.41}$	163.343460	57.381329	59 ± 6	16.7	0.218	163.343336	57.381257	43 ± 3	16.8	0.880	
...	...	163.342850	57.386243	31 ± 6	5.1	0.091	
...	...	163.338730	57.382906	25 ± 6	10.5	0.247	
...	163.343653	57.384025	197 ± 4	8.6	0.227	
...	163.334439	57.386083	90 ± 4	11.7	0.598	
...	163.347430	57.383169	61 ± 15	16.3	0.306
82	$1.79^{+1.03}_{-1.29}$	162.903830	57.631042	363 ± 12	6.4	0.008	162.904335	57.631430	862 ± 41	5.1	0.019	162.904180	57.630924	959 ± 22	6.8	0.007
...	...	162.905480	57.631763	93 ± 12	4.9	0.026	
...	...	162.902240	57.630337	70 ± 11	9.4	0.094	162.902240	57.629708	72 ± 21	11.6	0.213
...	162.906694	57.633462	305 ± 17	6.0	0.083	
...	162.909160	57.633895	21 ± 5	11.0	0.882	
...	162.900110	57.628619	49 ± 3	16.7	0.868	
...	162.909098	57.633911	25 ± 7	10.9	0.873	
...	162.906190	57.632486	115 ± 22	4.7	0.041
83	$1.89^{+0.91}_{-1.87}$	162.840330	57.709211	165 ± 18	4.2	0.011	162.840469	57.709222	401 ± 9	4.1	0.033	162.840940	57.709271	283 ± 24	3.6	0.010
...	...	162.849000	57.709257	59 ± 17	15.3	0.218	
...	162.837544	57.714951	152 ± 8	18.3	0.666	
...	162.842358	57.712567	20 ± 4	8.5	0.899	
...	162.848382	57.708510	24 ± 5	15.1	0.932	
...	162.847692	57.711210	17 ± 5	12.8	0.922	
...	162.832080	57.708247	77 ± 25	19.1	0.349
84	$1.89^{+0.71}_{-1.98}$	162.920420	57.188941	63 ± 9	1.4	0.005	162.921043	57.188856	119 ± 5	1.7	0.033	162.921320	57.188833	82 ± 17	2.1	0.018

...	...	162.918760	57.183850	37 ± 8	17.3	0.323
...	...	162.916560	57.187867	29 ± 9	7.8	0.172
...	...	162.926940	57.185605	28 ± 9	16.7	0.354	162.927541	57.186058	145 ± 7	16.7	0.628
...	162.927389	57.189506	374 ± 8	14.2	0.252
...	162.925405	57.190720	34 ± 4	12.6	0.895
...	162.917411	57.192994	56 ± 5	16.9	0.885
85	$1.79^{+1.00}_{-1.43}$	163.430310	57.425037	199 ± 6	14.2	0.061	163.430173	57.425106	1081 ± 21	14.1	0.081	163.431420	57.425120	393 ± 15	13.4	0.056
...	...	163.434000	57.425647	102 ± 7	11.7	0.090	163.433984	57.425613	865 ± 16	11.8	0.078	163.435020	57.425695	153 ± 15	12.1	0.125
...	...	163.431700	57.429228	46 ± 7	2.3	0.017	163.432225	57.429068	41 ± 5	1.2	0.059	163.431740	57.428725	89 ± 18	1.6	0.010
...	...	163.437830	57.432205	34 ± 7	16.0	0.304	163.437699	57.432524	410 ± 18	16.7	0.283	163.438490	57.432649	65 ± 20	18.0	0.331
...	...	163.431520	57.426063	30 ± 7	10.0	0.218	163.428200	57.424464	95 ± 14	17.7	0.275
...	...	163.427800	57.424773	22 ± 6	17.2	0.348
...	...	163.425140	57.431842	22 ± 6	18.1	0.344
...	163.431593	57.428092	112 ± 13	3.2	0.093	163.431740	57.428725	89 ± 18	1.6	0.010
...	163.437965	57.431518	32 ± 9	14.3	0.900
86	$1.79^{+0.97}_{-1.57}$	163.128230	57.369305	61 ± 6	2.0	0.010	163.128037	57.369335	193 ± 7	1.6	0.016	163.128500	57.369428	89 ± 14	2.5	0.020
...	...	163.121800	57.367376	46 ± 5	13.0	0.215	163.121551	57.367324	108 ± 6	13.5	0.624	163.121350	57.367128	85 ± 15	14.2	0.249
...	...	163.120910	57.373063	29 ± 5	17.9	0.361	163.120880	57.372842	113 ± 8	17.3	0.727
...	163.130124	57.364734	81 ± 11	17.9	0.831
...	163.124659	57.365240	49 ± 4	16.0	0.889
...	163.135937	57.368598	110 ± 8	17.2	0.733
87	$1.79^{+0.95}_{-1.53}$	162.655010	57.541291	52 ± 12	2.1	0.013	162.654827	57.541280	337 ± 10	1.8	0.010	162.655330	57.540959	136 ± 16	3.1	0.018
...	...	162.658900	57.543568	39 ± 11	12.5	0.229
...	...	162.659770	57.540565	36 ± 11	11.7	0.227
...	162.650163	57.543357	121 ± 17	10.2	0.441
...	162.649113	57.543860	24 ± 5	12.9	0.913
...	162.653829	57.543339	27 ± 5	7.1	0.765
88	$1.79^{+0.81}_{-1.84}$	163.492020	57.667372	84 ± 11	6.9	0.052	163.491745	57.667601	335 ± 8	7.9	0.121	163.492140	57.667187	260 ± 35	6.3	0.028
...	...	163.503660	57.664778	40 ± 12	18.0	0.331
...	...	163.488050	57.662641	39 ± 11	17.6	0.327
...	...	163.496160	57.663100	36 ± 12	11.0	0.220	163.496206	57.663085	195 ± 6	11.1	0.336	163.496180	57.663230	124 ± 30	10.5	0.132
...	163.487676	57.664595	141 ± 6	14.3	0.568
...	163.501916	57.667912	55 ± 9	15.6	0.880
...	163.485560	57.666597	39 ± 4	17.5	0.934
...	163.503151	57.663772	27 ± 3	18.4	0.921
89	$1.73^{+0.93}_{-1.51}$	162.656590	57.479112	421 ± 10	3.2	0.002	162.656425	57.479090	968 ± 11	2.9	0.006	162.656760	57.478953	710 ± 17	3.6	0.003
...	...	162.646780	57.477733	48 ± 10	16.6	0.267	162.646676	57.477563	307 ± 7	17.0	0.378	162.647460	57.477183	63 ± 17	16.1	0.327
...	162.654172	57.476494	117 ± 7	9.7	0.429
90	$1.65^{+0.90}_{-1.57}$	163.543413	57.554149	48 ± 3	15.5	0.901
91	$1.68^{+0.63}_{-1.81}$	163.550009	57.554730	36 ± 5	14.1	0.919
...	163.197334	57.184814	40 ± 3	16.6	0.923
...	163.196510	57.188842	75 ± 14	2.6	0.026
...	163.202670	57.190326	55 ± 14	14.4	0.332
...	163.194840	57.186583	50 ± 15	10.0	0.258

Table B4: All radio and 24 μ m identifications in the UDS field.

No.	$S_{1.1\mu\text{m}}$ (mJy)	RA _{1.4} (deg)	DEC _{1.4} (deg)	$S_{1.4}$ (μ Jy)	Dist. (")	p	RA ₂₄ (deg)	DEC ₂₄ (deg)	S_{24} (μ Jy)	Dist. (")	p
1	$5.29^{+1.40}_{-1.68}$	34.411903	-4.559684	95 ± 2	6.7	0.211
2	$3.99^{+1.10}_{-1.34}$	34.442192	-4.796477	77 ± 7	5.3	0.199
3	$3.75^{+1.22}_{-1.18}$	34.479333	-4.789667	113 ± 20	1.5	0.002	34.479359	-4.789783	776 ± 11	1.3	0.002
4	$4.39^{+1.67}_{-1.58}$	34.630307	-4.650681	107 ± 5	9.5	0.325
5	$3.57^{+1.19}_{-1.21}$	34.425542	-4.941028	89 ± 17	1.0	0.002
6	$3.99^{+1.27}_{-1.57}$	34.677833	-4.992167	105 ± 16	4.3	0.014	34.677600	-4.991972	924 ± 37	3.7	0.009

7	$3.99^{+1.57}_{-1.67}$	34.233034	-4.759176	174 ± 10	2.0	0.023
...	34.233708	-4.756331	143 ± 9	10.4	0.306
8	$3.99^{+1.59}_{-1.82}$	34.424875	-4.525111	153 ± 24	5.8	0.016	34.424837	-4.525333	329 ± 12	5.2	0.053
9	$3.75^{+1.90}_{-2.37}$	34.598958	-5.193944	36 ± 12	9.7	0.147	34.598853	-5.194038	95 ± 16	9.4	0.447
...	34.598925	-5.196769	147 ± 9	15.0	0.518
...	34.593195	-5.190765	64 ± 3	14.9	0.747
...	34.597081	-5.196744	34 ± 4	11.9	0.797
10	$3.07^{+1.21}_{-1.31}$	34.568708	-4.919111	240 ± 15	7.1	0.013	34.568580	-4.919129	1047 ± 33	6.7	0.021
11	$3.29^{+1.52}_{-1.71}$	34.283750	-4.935194	59 ± 15	8.7	0.077	34.283849	-4.935368	198 ± 6	8.1	0.185
...	34.281025	-4.935302	33 ± 5	12.1	0.705
...	34.286451	-4.936322	17 ± 2	11.5	0.306
12	$3.29^{+1.66}_{-1.94}$
13	$2.83^{+1.19}_{-1.36}$	34.618958	-4.912472	55 ± 19	9.3	0.084
14	$2.93^{+1.34}_{-1.52}$	34.420986	-4.767350	426 ± 9	9.9	0.114
15	$2.93^{+1.32}_{-1.53}$	34.477833	-4.741806	67 ± 14	13.0	0.110
...	...	34.477875	-4.736583	34 ± 13	6.0	0.078
...	...	34.478542	-4.739333	61 ± 18	4.2	0.028	34.478647	-4.739425	464 ± 10	4.7	0.032
16	$2.93^{+1.48}_{-1.59}$	34.317708	-4.966000	125 ± 26	10.8	0.054	34.317740	-4.966248	843 ± 10	10.0	0.056
...	34.313998	-4.967851	90 ± 7	13.9	0.609
17	$3.07^{+1.61}_{-1.99}$	34.299750	-4.721611	59 ± 20	5.4	0.045	34.300088	-4.721689	137 ± 16	6.6	0.218
18	$3.11^{+1.52}_{-2.65}$	34.355212	-4.532161	109 ± 6	16.0	0.689
...	34.348184	-4.527019	202 ± 7	15.6	0.467
...	34.348378	-4.532473	70 ± 7	18.0	0.844
...	34.350123	-4.530609	51 ± 4	8.8	0.662
19	$3.28^{+0.94}_{-3.27}$	34.774804	-4.897214	118 ± 12	17.1	0.681
...	34.775762	-4.891686	34 ± 6	3.5	0.345
20	$2.93^{+1.34}_{-2.61}$	34.425295	-5.118199	232 ± 21	18.0	0.489
...	34.420856	-5.125052	88 ± 8	18.1	0.800
21	$2.63^{+1.61}_{-1.77}$	34.538958	-5.076250	65 ± 20	12.5	0.135	34.538877	-5.076049	637 ± 17	13.3	0.129
...	34.543201	-5.078746	58 ± 2	8.3	0.576
22	$2.47^{+1.23}_{-1.54}$	34.616125	-4.893111	42 ± 16	14.7	0.185
...	34.618624	-4.887246	40 ± 4	10.7	0.741
23	$2.47^{+1.26}_{-1.57}$	34.585958	-4.958528	126 ± 34	9.9	0.050	34.586312	-4.959017	195 ± 5	9.5	0.249
24	$2.78^{+0.87}_{-2.81}$
25	$2.83^{+0.70}_{-2.89}$	34.605208	-5.156611	53 ± 18	0.3	0.000
...	34.608533	-5.158794	141 ± 5	14.1	0.527
...	34.603987	-5.159477	117 ± 20	11.4	0.487
26	$2.27^{+1.30}_{-1.48}$	34.634092	-4.941660	266 ± 13	3.6	0.042
27	$2.66^{+0.51}_{-2.78}$	34.659875	-4.581861	62 ± 23	8.6	0.084	34.659761	-4.581780	396 ± 17	8.8	0.114
...	34.662821	-4.580741	249 ± 9	2.8	0.029
...	34.659849	-4.583152	20 ± 4	11.2	0.850
...	34.660219	-4.580278	33 ± 5	7.1	0.675
28	$2.27^{+1.21}_{-1.73}$	34.511917	-5.008611	529 ± 14	14.1	0.019	34.511864	-5.008660	1172 ± 50	14.2	0.074
...	34.507718	-5.009330	151 ± 10	17.3	0.608
...	34.508261	-5.005937	134 ± 11	7.2	0.257

...	34.508090	-5.007461	32 ± 1	11.0	0.846
29	$2.13^{+1.27}_{-1.52}$	34.486417	-4.877444	88 ± 17	6.4	0.040	34.486430	-4.877678	435 ± 7	6.0	0.056	
...	...	34.483500	-4.881250	54 ± 20	11.3	0.140
...	34.484522	-4.881337	157 ± 12	10.4	0.359	
...	34.484959	-4.880100	33 ± 6	5.8	0.601	
30	$2.27^{+1.14}_{-2.03}$	34.420620	-5.042508	121 ± 7	17.1	0.694	
...	34.427263	-5.039770	155 ± 15	16.3	0.589	
...	34.423402	-5.038808	100 ± 4	2.3	0.065	
31	$2.85^{+0.01}_{-3.01}$	34.565159	-5.212831	114 ± 9	9.1	0.361	
...	34.568994	-5.217467	104 ± 7	13.0	0.541	
32	$2.13^{+1.05}_{-2.01}$	34.529958	-4.737167	68 ± 19	3.7	0.023
...	34.525632	-4.733848	325 ± 11	18.3	0.395	
...	34.530918	-4.742369	167 ± 9	18.4	0.629	
33	$2.03^{+1.13}_{-1.92}$	34.373208	-4.993639	81 ± 13	16.8	0.175	34.373355	-4.993668	539 ± 14	16.3	0.219	
...	...	34.377625	-4.993472	63 ± 15	2.5	0.013
...	...	34.380250	-4.989750	32 ± 12	17.8	0.321	34.380261	-4.989742	236 ± 9	17.9	0.501	
...	34.378463	-4.998602	60 ± 4	16.3	0.880	
...	34.377084	-4.997223	49 ± 6	11.6	0.818	
34	$2.03^{+1.11}_{-1.73}$	34.530583	-4.827694	67 ± 20	5.8	0.047	34.530710	-4.827852	407 ± 9	6.1	0.063	
...	34.532985	-4.826688	173 ± 46	15.2	0.514	
35	$2.19^{+0.57}_{-2.32}$	34.305542	-4.982639	54 ± 16	4.4	0.038
...	34.301078	-4.983261	38 ± 5	12.1	0.846	
...	34.301982	-4.986214	191 ± 28	16.0	0.496	
36	$2.17^{+0.61}_{-2.29}$	34.299203	-4.961543	63 ± 6	10.0	0.645	
37	$1.99^{+1.02}_{-1.88}$	34.471748	-4.981573	42 ± 4	13.0	0.876	
38	$2.64^{+0.01}_{-2.81}$	34.375103	-5.164719	220 ± 13	2.1	0.020	
...	34.376996	-5.163692	109 ± 9	6.1	0.232	
...	34.371440	-5.164847	85 ± 10	14.3	0.642	
...	34.374011	-5.163650	29 ± 4	5.3	0.542	
39	$2.42^{+0.01}_{-2.66}$	34.237126	-4.675920	156 ± 5	7.6	0.225	
...	34.234002	-4.672071	70 ± 7	10.2	0.572	
40	$1.83^{+1.01}_{-1.81}$	34.611500	-4.825250	56 ± 18	2.3	0.014
...	34.616148	-4.824096	265 ± 7	18.8	0.488	
...	34.610162	-4.828669	100 ± 8	10.9	0.560	
41	$1.94^{+0.74}_{-2.03}$	34.612875	-4.746444	36 ± 13	18.2	0.295
...	34.607719	-4.743902	198 ± 10	7.8	0.202	
42	$1.83^{+1.00}_{-1.82}$	34.400958	-4.801972	126 ± 28	16.7	0.120	34.400986	-4.802091	523 ± 9	16.8	0.236	
...	...	34.405167	-4.798000	64 ± 14	9.7	0.110	34.405089	-4.798160	202 ± 7	9.2	0.258	
...	...	34.406167	-4.801278	142 ± 16	3.4	0.009	34.406547	-4.801338	51 ± 13	4.6	0.369	
...	34.405351	-4.801697	268 ± 19	3.7	0.045	
...	34.399962	-4.799696	107 ± 8	20.0	0.823	
...	34.402387	-4.796087	170 ± 8	19.9	0.678	
...	34.408115	-4.798993	60 ± 11	11.4	0.756	
...	34.404316	-4.802323	20 ± 5	7.1	0.874	
43	$2.65^{+0.01}_{-2.79}$	34.640708	-5.171083	108 ± 21	3.1	0.009	34.640900	-5.171446	903 ± 26	1.6	0.002	

This paper has been typeset from a T_EX/ L^AT_EX file prepared
by the author.